materials

MDPI

Article

Rendering Mortars Reinforced with Natural Sheep's Wool Fibers

Cinthia Maia Pederneiras [1,2], Rosário Veiga [2] and Jorge de Brito [1,*]

[1] CERIS, Instituto Superior Técnico, University of Lisbon, 1049-001 Lisbon, Portugal; cinthiamaia@tecnico.ulisboa.pt

[2] National Laboratory for Civil Engineering, 1700-066 Lisbon, Portugal; rveiga@lnec.pt

* Correspondence: jb@civil.ist.utl.pt; Tel.: +351-218-418-118

Received: 12 October 2019; Accepted: 4 November 2019; Published: 6 November 2019

Abstract: The susceptibility of rendering mortars to cracking is a complex phenomenon. Fibers have been incorporated in mortars to ensure the durability of the render and can improve the flexural strength, fracture toughness, and impact resistance of the mortars. Aside from the better cracking performance of fiber reinforced mortars, natural fibers have been a path to reducing the environmental impacts of construction materials. Recycling has high sustainability-related potential as it can both mitigate the amount of waste being inadequately disposed and reduce the consumption of natural raw materials. Studies on the incorporation of waste in civil engineering materials have been growing, and recycled fibers may be feasible to incorporate in mortars. Natural fibers are considered as a viable replacement for synthetic ones. Several studies have investigated vegetal fibers in cementitious composites. However, only a few have focused on the incorporation of waste animal-based fiber. The aim of this work is to analyze the feasibility of the use of natural sheep's wool fibers on the reinforcement of mortars and in particular to improve their cracking behavior. For this purpose, two different binders were used: cement and cement-lime mortars were produced. The incorporation of 10% and 20% (in volume) of 1.5 cm and 3.0 cm wool fibers was analyzed. The results show that the incorporation of wool fibers increased the ductility of the mortars and improved their mechanical properties.

Keywords: render; cement and cement-lime reinforced mortars; natural fiber; sheep's wool; sustainability

1. Introduction

The construction sector has been trying to reduce its environmental impacts. Eco-friendly constituents have been an alternative to develop new cementitious materials. In order to enhance the cracking performance of mortars, the incorporation of natural fibers can contribute to better performance while ensuring a sustainable approach. According to previous studies, natural fibers such as sheep wool may improve the ductility of cementitious composites and also provide an adequate disposal of the waste [1].

The incorporation of fibers enhances a better post-cracking behavior due to the higher fracture toughness, flexural strength, and impact resistance of the mortars [2]. The benefits of fiber reinforcement in cementitious materials depend on the fiber type, their geometry, and their volume ratio and distribution [3]. The use of natural fibers compared to man-made fibers has been achieving environmental, energy, and resource conservation benefits [4]. There are three types of natural fibers: plant-based, mineral-derived, and animal-based. In this paper, the study focused on animal-based fibers, namely sheep's wool fibers.

Natural sheep wool is considered as waste on a large-scale, taking into account that 270.000 tons of wool are produced by 90 million sheep in Europe [3]. Indeed, 75% of the wool produced (around

150 million tons per year) is rejected by the textile industry [4,5]. Most of this material does not have a proper disposal method. Furthermore, the wool fibers have an elastic modulus of about 1–4 GPa, which can be comparable to the modulus of plastic fibers [5].

Several studies have been carried out to investigate the incorporation of wool fibers in cementitious materials to improve the thermal insulation properties [6–9]. However, only a few studies, described next, have incorporated wool fibers with the purpose of improving the mechanical performance of cementitious composites.

Alyousef et al. [10] analyzed the mechanical properties of reinforced concrete with wool fibers and found that the incorporation of fibers decreased the workability of concrete. Concerning the mechanical behavior, the fibers enhanced the ductility and flexural capacity of the composite. In terms of compressive strength, the incorporation of fibers implied a reduction of strength. This reduction was explained by the authors by the incorporation of wool up to 6% by weight of cement in the concrete, which led to a reduction of the total binder in the mix.

Fantilli et al. [5] investigated the incorporation of 1% (in volume) of wool fibers in cementitious reinforced-mortars. The authors observed that the fibers reduced the brittle nature of the mortars due to the development of bridge mechanisms between the crack borders. In this research, an improvement in the fracture toughness in the reinforced mortars of 300% relative to the control mortar is reported. It could also be seen that the wool fibers promoted a reduction in the plastic shrinkage. The cementitious mortars reinforced with wool fibers presented the same mechanical performance (i.e., strengths and modulus of elasticity) as those in mortars with the most common vegetal fibers.

Giosué et al. [11] investigated the replacement of 25% (in volume) of aggregates with wool fibers in lime-based lightweight mortars. The modified mortars were tested in the fresh and hardened state concerning workability, mechanical strength, and hygro-thermal properties. The results showed an increase of about 30% in the flexural strength of the modified mortars.

Kesikidou and Stefanidou [12] investigated the incorporation of natural fibers in mortars. The authors analyzed mortars with two different binders, incorporating vegetal fibers such as jute, coconut, and kelp and showed that the natural fibers performed differently in relation to cement or lime-based binder. Lime-reinforced mortars presented a higher increase in flexural and compressive strength when compared to the cement-based reinforced mortars. Therefore, the compatibility of the fibers with the mortar's composition should be evaluated.

As a conclusion of this review, it was found that, aside from all of the studies carried out on mortars with natural fibers, the incorporation of wool fibers in rendering cementitious mortars could not be found in the technical literature. This is relevant because rendering mortars mainly have the function of protecting the substrate. This means that a high compressive strength is not often necessary, but is important to minimize cracking. As a consequence, usually low strength mortars with a low binder/aggregate ratio are used, and from this aspect, leads to a different microstructure and a poorer adhesion between the binder, aggregates, and fibers.

Additionally, the compositions used result in a low modulus of elasticity, possibly nearer the modulus of elasticity of natural fibers than in the case of structural mortars. Finally, for rendering mortars, as a favorable cracking behavior is more important than a high mechanical strength, characteristics such as a low modulus of elasticity and ductility are mainly required. Therefore, the novelty of this work was in analyzing the feasibility of the incorporation of wool fibers in rendering mortars and their efficacy in improving those specific properties. Cement and cement-lime mortars with low binder/aggregate volumetric ratios of 1:4 and 1:3 were produced, respectively, with different fibers lengths of 1.5 and 3.0 cm, respectively. The ratios of incorporation were 10% and 20% of the total mortar volume.

The mortars' properties considered relevant for rendering mortars, namely workability, bulk density, dynamic modulus of elasticity, ultra-sound pulse velocity, flexural and compressive strengths, and protection to water action, were evaluated in the fresh and hardened states.

From the results, it could be seen that the incorporation of wool fibers in rendering mortars with a volumetric ratio of 1:4 (cement: aggregates) and 1:1:6 (cement:air-lime:aggregates) improved the

cracking behavior of the materials as the modified mortars, in general, presented a higher flexural strength and a lower modulus of elasticity when compared to the plain mortars.

2. Experimental Program

The aim of this research was to evaluate the influence of natural fiber waste, namely sheep wool, incorporated in rendering mortars.

Cement mortars and cement-air lime-based mortars were produced. The volumetric proportions were 1:4 (cement: aggregates) and 1:1:6 (cement:air-lime:aggregates). Aside from the binder, the length and volume ratio were parameters used to formulate the analyzed mortars.

Mortars were identified as follows:

- REF 1:4 (0% of incorporation—reference cement mortar)
- W 1.5_10%c (10% of incorporation of 1.5 cm long wool fibers—cement mortar)
- W 3.0_10%c (10% of incorporation of 3.0 cm long wool fibers—cement mortar)
- W 1.5_20%c (20% of incorporation of 1.5 cm long wool fibers—cement mortar)
- W 3.0_20%c (20% of incorporation of 3.0 cm long wool fibers—cement mortar)
- REF 1:1:6 (0% of incorporation—reference cement-lime mortar)
- W 1.5_10%cl (10% of incorporation of 1.5 cm long wool fibers—cement-lime mortar)
- W 3.0_10%cl (10% of incorporation of 3.0 cm long wool fibers—cement-lime mortar)
- W 1.5_20%cl (20% of incorporation of 1.5 cm long wool fibers—cement-lime mortar)
- W 3.0_20%cl (20% of incorporation of 3.0 cm long wool fibers—cement-lime mortar)

2.1. Materials

The materials used were cement, air-lime, sand, and wool fibers. The binder used on the cement mortars was CEM II/B-L 32.5 N, according to EN 197-1 [13]. The calcium hydrated lime powder—air lime—used was class CL80-S, according to EN 459-1 [14]. The natural silica sand was previously washed, calibrated, and sieved for a required size distribution. The wool fibers were washed with neutral detergent, and dried at 40 °C. This procedure was applied to remove the impurities. The fiber length was obtained by manually cutting the waste material. The fibers were added in order to ensure a homogeneous dispersion in each mix composition. The homogeneity of the fibers in the mix was implemented by distributing them in a properly closed receptacle and blowing compressed air over them in order to achieve an adequate dispersion before adding to the mix. Figure 1 presents the wool fibers used in the experimental campaign. The apparent bulk density of the constituents of the mortars produced is presented in Table 1.

2.2. Methods

All tests carried out in the experimental program are described in Table 3.

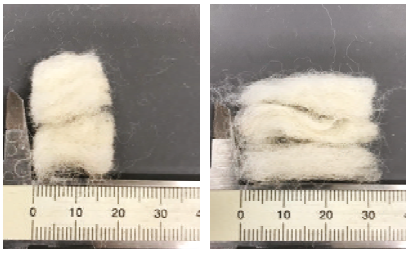

(**a**) (**b**)

Figure 1. Sheep wool fiber used: (**a**) 1.5 cm long (**b**) 3.0 cm long.

Table 1. Apparent bulk density of the constituents.

Component	Apparent Bulk Density (kg/m^3)
Cement	975.5
Air-lime	565.7
Sand	1230.8
Wool 1.5 cm	4.25
Wool 3.0 cm	2.53

Table 2 presents the composition of the mortars produced in this work.

Table 2. Composition of the mortar mixes by mass.

Mortar	Cement (g)	Air-lime (g)	Sand (g)	Water (g)	Fibers (g)
REF 1:4	487.8	-	2461.6	445	-
W 1.5_10%c	439.1	-	2215.4	405	1.1
W 3.0_10%c	439.1	-	2215.4	435	0.6
W 1.5_20%c	390.2	-	1969.3	350	2.1
W 3.0_20%c	390.2	-	1969.3	350	1.3
REF 1:1:6	304.8	176.8	2307.8	465	-
W 1.5_10%cl	274.4	159.1	2077.0	435	1.1
W 3.0_10%cl	274.4	159.1	2077.0	420	0.6
W 1.5_20%cl	243.9	141.4	1846.2	370	2.1
W 3.0_20%cl	243.9	141.4	1846.2	370	1.3

Table 3. Experimental campaign tests.

Test	European Standard	Samples	Specimens	Age (days)
Apparent bulk density	Cahier 2669-4 [15]	6	Cement, lime, sand and fibers	-
Consistence by flow table	EN 1015-3 [16]	3	Fresh mortar	-
Bulk density	EN 1015-6 [17]	3	Fresh mortar	-
Dry bulk density	EN 1015-10 [18]	3	Hardened mortar	28, 90, and 180
Dynamic modulus of elasticity by resonance frequency method	EN 14146 [19]	3	Hardened mortar	28, 90. and 180
Ultra-sound pulse velocity	EN 12504-4 [20]	1	Hardened mortar	28, 90, and 180
Flexural and compressive strengths	EN 1015-11 [21]	3	Hardened mortar	28
Open porosity	EN 1936 [22]	3	Hardened mortar	28

For the hardened mortar tests, prismatic samples (40 mm × 40 mm × 160 mm) were used, in accordance with European Standards.

For ultra-sound pulse velocity, the direct and indirect methods were used for the measurements. In the direct transmission method, the electrodes are placed on the opposite surfaces of the specimen. In the indirect method, the electrodes are positioned on the same surface of the prism: the transmitter electrode is fixed at a specific point and the receptor moves over the specimen, and at different distances, the transmission time is measured allowing for the velocity to be calculated.

In order to analyze the susceptibility to cracking of the mortars produced in this work, some parameters were calculated. The Center Scientifique et Technique du Bâtiment (CSTB) [15] refers to the dynamic modulus of elasticity and flexural strength ratio (E/σ_f) as indicators of the mortar's ability to resist cracking. This criterion is based on the fact that a lower dynamic modulus of elasticity provides a higher deformation capacity of the material, and a greater flexural strength induces the material to

withstand tensions without cracking. Therefore, the tendency to crack due to restrained shrinkage is greater when the ratio between the modulus of elasticity and tensile strength is high.

Another parameter to evaluate the susceptibility to crack is based on the flexural and compressive strengths. The ductility of the material can be associated to this ratio (σ_f/σ_c) (i.e., the mortar is considered more ductile when this value is closer to 1). Ductility is a measure of the deformability of the material before fracture. Cracking resistance is correlated with the deformation capacity of the mortar and its ability to absorb stress without cracking [23].

The ability to absorb energy before fracture is correlated with the toughness of the mortar. The fracture toughness was calculated by the total area under the strain–stress curve of the results of flexural strength at 28 days.

Regardless of the binder used, all hardened mortars were cured as specified by EN 1015-11 [21]. The specimens were kept in molds for two days at a temperature of 20 ± 2 °C and a relative humidity of 95 ± 5%. After demolding, all specimens were maintained in the same conditions for a total of seven days. After that, the specimens were kept at 20 ± 2 °C and the relative humidity was reduced to 65 ± 5%, until testing.

3. Results and Analysis

3.1. Fresh State

The mortar's workability was measured by the consistency test. To improve the comparability of the results, the values were limited to 140 ± 5 mm. The mortars presented a stiff consistence, but an application on a brick was carried out to ensure that an adequate workability was achieved, as shown in Figure 2.

Figure 2. Mortar application on a brick.

It was noticed that the fibers kept the mortar agglutinated. Although the workability was acceptable, the flor value did not increase due to the fibers' agglutinating action. In order to illustrate this behavior, Figure 3 presents the flow table test of the W 1.5_10%c sample.

Figure 3. Flow table test for the modified mortar.

Table 4 presents the results of the fresh mortars' properties.

Table 4. Fresh mortar properties.

Mortar	w/b Ratio	Consistency (mm)	Bulk Density (kg/m^3)
REF 1:4	0.91	140	2005.3
W 1.5_10%c	0.92	141	1978.1
W 3.0_10%c	0.98	139	1969.5
W 1.5_20%c	0.89	135	1936.5
W 3.0_20%c	0.89	141	2002.9
REF 1:1:6	0.98	140	1998.8
W 1.5_10%cl	1.02	141	1980.3
W 3.0_10%cl	0.98	141	1977.8
W 1.5_20%cl	0.97	139	1970.3
W 3.0_20%cl	0.97	139	1985.9

In all cement-lime mortars, the water/binder ratio was higher than that of the cement mortars. The incorporation of 10% of wool fibers increased the amount of water needed to maintain the workability. This could be due to the morphology of the fiber, which is composed of keratin filaments [5]. However, the incorporation of 20% of fibers again decreased the water/binder ratio to values similar to the control mortar. This trend reversion may be due to the fact that the longer fibers have a lower bulk density and thus a lower weight of incorporated fibers is actually used (Table 2). The modified mortars presented a lower bulk density than that of the reference mortars.

3.2. Hardened State

3.2.1. Dry Bulk Density of the Hardened Mortars

The dry bulk density of the hardened mortars was determined at 28, 90, and 180 days and the results are presented in Figure 4. The same trend as for the fresh state was noticed: the incorporation of wool fibers reduced the dry bulk density of the mortars due to the low bulk density of the fibers. Giosué et al. [11] found similar results (i.e., the bulk density of the reinforced mortars had a decrease of about 13% compared to the control mortar at 28 days).

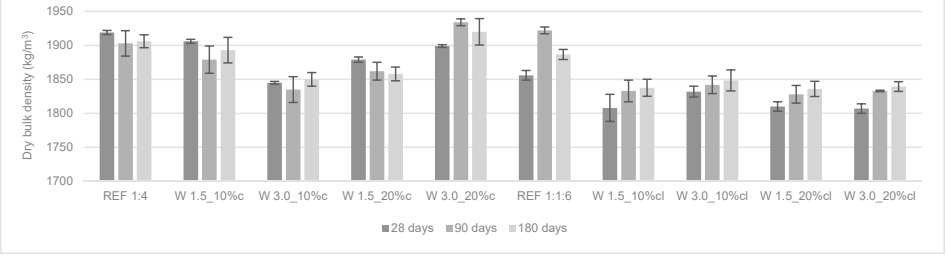

Figure 4. Dry bulk density of the hardened mortars.

In general, the dry bulk density of the cement mortars decreased from 28 to 90 days. Dry bulk density is defined as the ratio between mass and volume. Thus, the variations in weight and volume during time explain the variations in dry bulk density. In a previous study, a similar trend of decrease from 28 to 90 days was found [24], possibly because the mass reduction overlapped the volume reduction.

The opposite effect occurred in the cement-lime mortars, which presented an increase in this property over time. In fact, cement-lime mortars also have shrinkage with the consequent reduction of

volume, and possibly have an increase in weight due to a higher carbonation reaction (by comparison with cement-only mortars). Previous works have shown this same trend for air lime mortars [25].

3.2.2. Dynamic Modulus of Elasticity of the Hardened Mortars

The modulus of elasticity measures the ability of the rendering mortars to absorb deformations. The renders should be able to withstand higher internal stresses without cracking. The dynamic modulus of elasticity was determined at 28, 90, and 180 days. The results are presented in Figures 5 and 6.

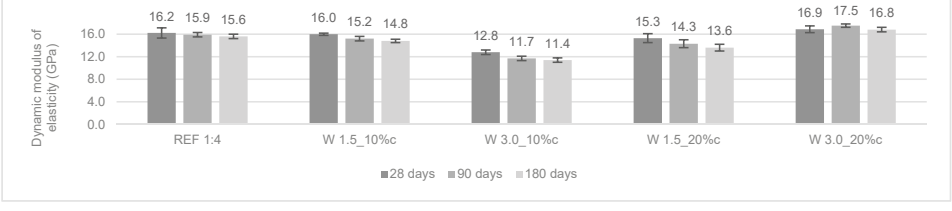

Figure 5. Dynamic modulus of elasticity of the cement mortars.

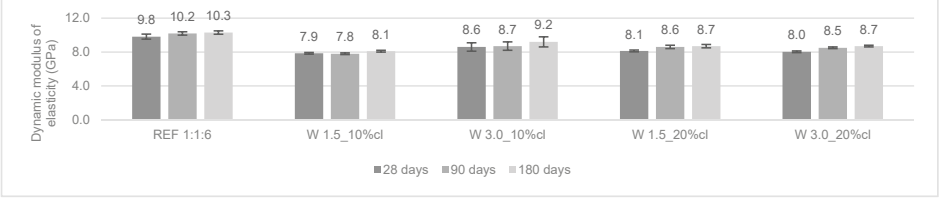

Figure 6. Dynamic modulus of elasticity of the cement-lime mortars.

In general, the modified mortars presented a lower modulus of elasticity when compared to the reference mortars. For cement mortars, the modulus of elasticity decreased from 28 to 180 days. This could be attributed to the internal micro-cracking of the mortars over time. The opposite trend occurred in cement-lime mortars (i.e., the modulus of elasticity presented a slight increase from 28 to 90 days).

According to Araya-Letelier et al. [26], the incorporation of pig hair in mortars did not lead to a significant reduction in the dynamic modulus of elasticity. The authors explained this effect by the small amount of total fiber volume incorporated (up to 1.5%).

3.2.3. Ultra-Sound Pulse Velocity of the Hardened Mortars

The ultra-sound pulse velocity test was performed at 28, 90, and 180 days. The results are presented in Table 5. The ultra-sound pulse velocity results showed that the incorporation of fibers reduced the pulse velocity through the mortar, indicating a decrease in the modulus of elasticity (Table 5).

These results followed the same trend as those of the modulus of elasticity test, as expected. The direct method showed a decrease of the pulse velocity in cement mortars, which could be related to some internal cracks due to shrinkage. According to the indirect method, this reduction is not that significant as it measures the velocity in small distances in the prism, which may detect a more distributed crack pattern and consequent decrease of the pulse velocity, as seen by the high R^2 of the velocity trend lines (Figures 7 and 8).

Table 5. Ultra-sound pulse velocity of the mortars tested.

Mortar	Ultra-Sound Pulse Velocity (m/s)					
	Direct Method			Indirect Method		
	28 days	90 days	180 days	28 days	90 days	180 days
REF 1:4	2855	2751	2661	2551	2581	2676
W 1.5_10%c	2727	2695	2650	2516	2530	2361
W 3.0_10%c	2641	2493	1842	2830	2293	2399
W 1.5_20%c	2556	2602	1855	2677	2739	2545
W 3.0_20%c	2788	2925	1892	2652	2779	2731
REF 1:1:6	2205	2218	2321	2190	2059	2321
W 1.5_10%cl	2050	1990	2051	1921	1968	2003
W 3.0_10%cl	2118	2169	2219	2039	2108	2050
W 1.5_20%cl	2040	2076	2143	2136	2071	2276
W 3.0_20%cl	1985	2065	2120	1957	1936	2017

Figures 5 and 6 present the results of the ultra-sound pulse velocity test by the indirect method for the reference mortars and W 1.5_10% mortars.

3.2.4. Flexural and Compressive Strength of the Hardened Mortars

Figures 9 and 10 present the results of the flexural and compressive strengths at 28 days. In general, the incorporation of wool fibers in cement mortars improved their flexural strength. Longer fibers (3.0 cm) presented a higher increase in flexural strength. The cement mortar with 20% of 3.0 cm long wool fibers had an increase of 40% and 26% in flexural and compressive strength, respectively, compared to REF 1:4.

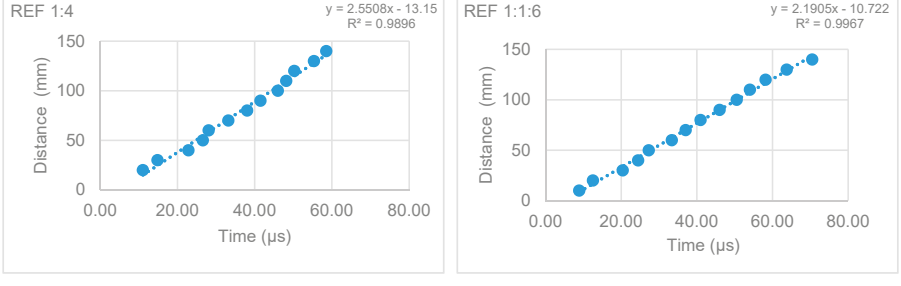

Figure 7. Ultra-sound pulse velocity of the reference mortars.

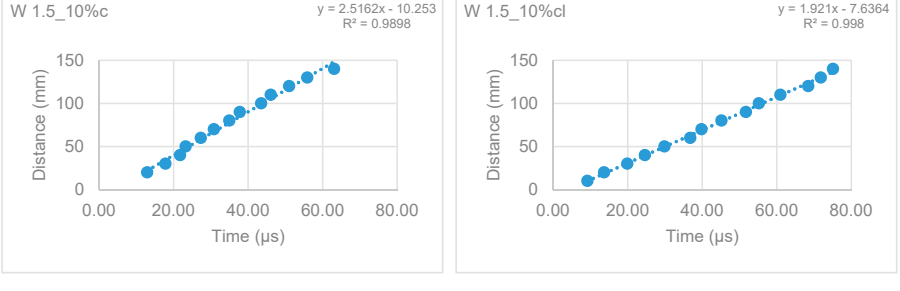

Figure 8. Ultra-sound pulse velocity of the W 1.5_10% mortar.

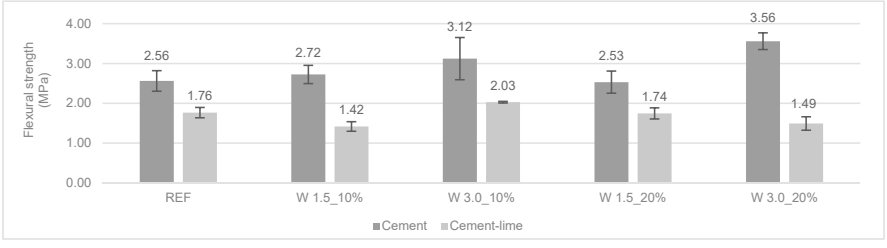

Figure 9. Flexural strength of the mortars at 28 days.

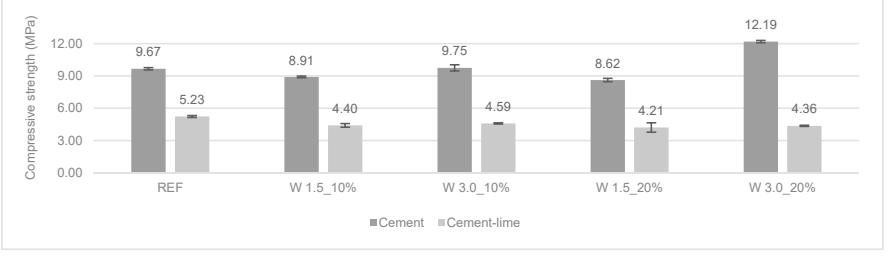

Figure 10. Compressive strength of the mortars at 28 days.

For cement-lime mortars, only W 3.0 cm 10% had an increase of 15% in this property when compared to REF 1:1:6. In general, the modified cement-lime mortars presented a slight decrease in flexural strength. W 1.5 cm 10% obtained the lowest flexural strength, 20% less than the reference mortar. Figure 11 presents the mechanical tests carried out on the mortars.

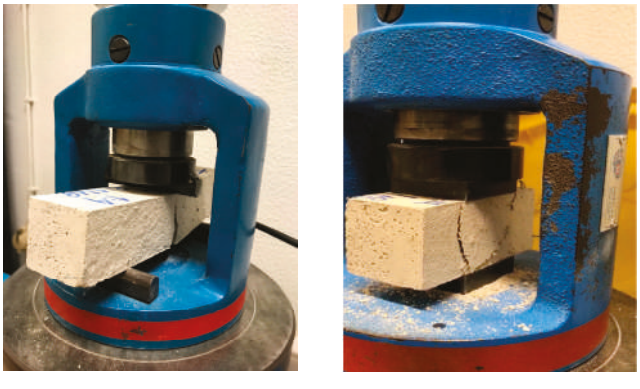

(**a**) (**b**)

Figure 11. Flexural strength test (**a**); compressive strength test (**b**).

Fantilli et al. [5] reached similar conclusions to those of the cement mortars. The modified mortars with wool fibers had an 18% higher flexural strength than that of the control mortar. Araya-Letelier et al. [23] studied the incorporation of natural animal fibers such as pig hair in mortars and also reported an increase in flexural strength of the modified mortars. Giosué et al. [11] reported that a hydraulic-lime mortar with wool fibers achieved about a 30% higher flexural strength than that of the conventional mortar. These previous works explained this increase in flexural strength due to a bridging mechanism.

In the compressive strength test, a different trend was found regarding the type of the binder used and the length of the fibers. Indeed, it can be seen that the longer fibers led to an increase in the compressive strength when compared to the cement mortar reference. Modified cement mortars with 1.5 cm of wool fiber presented a slight decrease in compressive strength.

The modified cement-lime mortars obtained a slight reduction of compressive strength compared to the control mortar (REF 1:1:6). W 1.5_20% cl obtained the most significant decrease compared to the reference mortar, about 20%.

Giosué et al. [11] found a decrease in the modified lime-based mortars with wool fibers. The authors reported that the use of fibers reduced the compressive strength of mortars. In agreement with this study, Araya-Letelier et al. [26] found a reduction of compressive strength with the incorporation of animal-based fibers in cement mortars.

Figure 12 presents a sample of the modified mortar, where the wool fibers do not produce a significant change in the mortar's appearance.

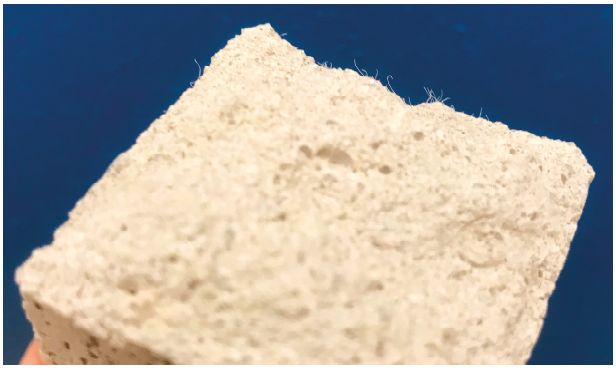

Figure 12. Sample of the modified mortar with wool fiber incorporation.

3.2.5. Cracking Behavior

Restrained shrinkage can be induced by the restrictions imposed on deformations of a rendering mortar. Tensile stresses should be dissipated without cracking of the coating. There are several causes that lead the mortar to crack. In order to evaluate the mortar's susceptibility to cracking, some parameters were considered to enhance the analysis of this phenomena as described above, and the results are presented in Table 6.

The values of fracture toughness are presented in Table 6.

An increase in the fracture toughness of the modified cement mortars was noticed. The increment was higher when longer fibers were incorporated, regardless of the incorporation ratio. W 3.0_10%c and W 3.0_20%c attained up to 100% higher toughness values when compared with the reference cement mortar (REF 1:4).

The fracture toughness results of the cement-lime mortars did not present significant changes.

These results are in accordance with previous studies [5,27]. Fantilli et al. [5] also obtained a higher fracture toughness with the incorporation of wool fibers in cementitious composites. This can be explained by the fibers' bridging mechanism, since the fibers cross the micro-cracks, preventing their propagation and delaying the occurrence of the first crack. Reinforced mortars may withstand tensile load after cracking and exhibit ductile behavior [1,28].

Table 6. The mechanical test results of the hardened mortars and parameters related to cracking.

Mortar	Dry Bulk Density (kg/m^3)	Dynamic Modulus of Elasticity (MPa)	Flexural Strength (MPa)	Compressive Strength (MPa)	E/σ_f	σ_f/σ_c	Fracture Toughness (N.mm)
REF 1:4	1919	16210 ± 0.91	2.56 ± 0.21	9.66 ± 0.11	6332	0.27	0.195 ± 0.07
W 1.5_10%c	1906	15980 ± 0.19	2.72 ± 0.19	8.75 ± 0.08	5875	0.31	0.278 ± 0.04
W 3.0_10%c	1845	12790 ± 0.29	3.12 ± 0.43	9.47 ± 0.25	4099	0.33	0.415 ± 0.05
W 1.5_20%c	1879	15290 ± 0.61	2.53 ± 0.22	8.53 ± 0.16	6043	0.30	0.235 ± 0.06
W 3.0_20%c	1899	16860 ± 0.47	3.56 ± 0.17	11.50 ± 0.11	4736	0.31	0.392 ± 0.06
REF 1:1:6	1856	9820 ± 0.21	1.76 ± 0.10	5.22 ± 0.09	5580	0.34	0.135 ± 0.02
W 1.5_10%cl	1808	7850 ± 0.09	1.42 ± 0.09	3.28 ± 0.15	5528	0.43	0.090 ± 0.01
W 3.0_10%cl	1832	8600 ± 0.41	2.03 ± 0.01	4.48 ± 0.06	4236	0.45	0.147 ± 0.03
W 1.5_20%cl	1810	8130 ± 0.05	1.74 ± 0.11	3.17 ± 0.40	4672	0.55	0.127 ± 0.02
W 3.0_20%cl	1807	8030 ± 0.04	1.49 ± 0.13	2.99 ± 0.05	5389	0.50	0.104 ± 0.02

Araya-Letelier et al. [26] found that the incorporation of animal-based fibers, namely pig hair, increased the fracture toughness of the fiber-reinforced mortars. The authors related this increment to the increase in the impact energy absorption capacity of the mortars due to the addition of fibers. In this work, it was reported that the post-cracking behavior of the modified mortars was improved by up to 55% higher energy absorbed at failure.

Considering these factors, all the modified mortars evaluated in this work were less susceptible to cracking. However, the cement-lime mortars presented more ductility than the cement mortars. The incorporation of 20% of 1.5 cm long wool fibers in cement-lime mortars presented the best results regarding ductility. Table 6 presents the results of tests on the hardened mortars.

3.2.6. Open Porosity

The open porosity test determines the volume of interconnected voids in the mortars, in percentage. This property is correlated with the ultra-sound pulse velocity and modulus of elasticity as well as the mechanical strength and water tightness behavior. Table 7 presents the results of the open porosity test.

Table 7. Open porosity test results of the hardened mortars.

Mortar	Open Porosity (%)
REF 1:4	20.18 ± 0.003
W 1.5_10%c	20.91 ± 0.001
W 3.0_10%c	20.91 ± 0.007
W 1.5_20%c	20.82 ± 0.003
W 3.0_20%c	19.88 ± 0.003
REF 1:1:6	23.93 ± 0.003
W 1.5_10%cl	24.93 ± 0.008
W 3.0_10%cl	24.65 ± 0.003
W 1.5_20%cl	24.73 ± 0.008
W 3.0_20%cl	25.49 ± 0.012

The results of the open porosity test confirmed the expectations. In general, the incorporation of fibers increased the volume of pores of the modified mortars. W 3.0_20%c was an exception, as it presented a reduction of 1.5% of total open porosity compared to the control cement mortar. The incorporation of 10% of wool fibers in cement mortars presented the same values, regardless of the length of the fibers.

The cement-lime modified mortars exhibited a greater increase in the volume of pores than that of the cement mortars. W 3.0_20% cl obtained an increase of about 6.5% of total open porosity compared to REF 1:1:6.

Giosué et al. [11] also noticed an increase (32%) of total open porosity in hydraulic lime-mortars with the incorporation of 25% of wool fibers when compared to the control mortar. The increase in open porosity of the modified mortars could be explained by the fiber–matrix interfacial bond that is thought to be less efficient than that of the sand–matrix.

4. Conclusions

From the results of the experimental campaign, it was concluded that the incorporation of wool fibers in rendering mortars presented a satisfactory performance concerning the mechanical and cracking behavior. All of the modified mortars presented less susceptibility to cracking when compared with the mortars without fibers, based on the parameters evaluated.

In general, the reinforced mortars presented a decrease in the dynamic modulus of elasticity, which can be considered an advantage of the incorporation of wool fibers. W 3.0_10%c and W 1.5_10%cl obtained a similar decrease of 20% of modulus of elasticity when compared to the control mortar.

Regarding flexural strength, the modified cement mortars presented an increase when compared to the reference mortar. The addition of longer fibers enhanced the mechanical strength of the mortars. W 3.0_20%c obtained an increase of 40% in flexural strength when compared to REF 1:4. The cement-lime modified mortars obtained a slight reduction in flexural strength, with the exception of W 3.0_10%cl.

The dynamic modulus of elasticity and flexural strength ratio (E/σ_f) was analyzed as an indicator of the mortars' ability to resist cracking. It could be seen that all of the modified mortars, regardless of the binder used, presented a lower (E/σ_f) ratio, which could lead to a lesser tendency to crack due to restrained shrinkage when compared to the reference mortars.

The ratio (σ_f/σ_c) is related to the mortar's ductility. According to the results, all the modified mortars presented a higher ratio (σ_f/σ_c) compared to the reference mortars, which allows concluding that the incorporation of fibers increased the ductility of those mortars, based on this parameter.

Regarding fracture toughness, the modified cement mortars presented improvements. In fact, the toughness increment was higher when longer fibers were incorporated. However, for the cement-lime mortars, the toughness results did not present any significant contribution of the incorporation of the fibers.

Besides the analyzed parameters related with the cracking behavior, it was also found that, concerning compressive strength, the incorporation of longer fibers in cement mortars (W 3.0_10%c and W 3.0_20%c) resulted in an increase.

The results obtained in this work identify the advantages of the addition of the natural wool fibers in rendering mortars, namely concerning the improvement in the mechanical, and in particular of the cracking behavior.

Author Contributions: C.M.P. performed the experiments in the Building Finishes and Thermal Insulation Unit (NRI) of the National Laboratory for Civil Engineering of Portugal (LNEC). The analyses of the tests and the interpretation of the results were developed by C.M.P., R.V. and J.d.B. The original draft of this paper was written by C.M.P. and the review and editing were performed by R.V. and J.d.B.

Funding: This research was funded by Portuguese Foundation for Science and Technology (FCT) (PD/BD/135193/2017).

Acknowledgments: The authors would like to acknowledge the REuSE project from National Laboratory for Civil Engineering of Portugal (LNEC) and the research unit CERIS from Instituto Superior Técnico (IST).

Conflicts of Interest: The authors declare no conflicts of interest.

References

1. Pederneiras, C.M.; Veiga, R.; De Brito, J. Effects of the incorporation of waste fibres on the cracking resistance of mortars: A review. *Int. J. Green Technol.* **2018**, *4*, 38–46.
2. Erdogmus, E. Use of Fiber-Reinforced cements in masonry construction and structural rehabilitation. *Fibers* **2015**, *3*, 41–63. [CrossRef]
3. Grădinaru, C.M.; Bărbuță, M.; Șerbănoiu, A.A.; Babor, D. Investigations of the mechanical properties of concrete with sheep wool fibers and fly ash. *Eng. Sci.* **2016**, *9*, 73–80.
4. Onuaguluchi, O.; Banthia, N. Plant-based natural fibre reinforced cement composites: A review. *Cem. Concr. Compos.* **2016**, *68*, 96–108. [CrossRef]

5. Fantilli, A.P.; Sicardi, S.; Dotti, F. The use of wool as fiber-reinforcement in cement-based mortar. *Constr. Build. Mater.* **2017**, *139*, 562–569. [CrossRef]
6. De Fazio, P.; Cardinale, T.; Arleo, G.; Bernardo, F.; Feo, A. Thermal and mechanical characterization of panels made by cement mortar and sheep's wool fibres. *Energy Procedia* **2017**, *140*, 159–169.
7. Florea, I.; Manea, L. Analysis of thermal insulation building materials based on natural fibers. *Procedia Manuf.* **2019**, *32*, 230–235. [CrossRef]
8. Zach, J.; Korjenic, A.; Petranek, V.; Hroudová, J.; Bednar, T. Performance evaluation and research of alternative thermal insulations based on sheep wool. *Energy Build.* **2012**, *49*, 246–253. [CrossRef]
9. Bosia, D. Sheep wool for sustainable architecture. *Energy Procedia* **2015**, *78*, 315–320. [CrossRef]
10. Alyousef, R.; Aldossari, K.; Ibrahim, O.A.; Mustafa, H.; Jabr, A. Effect of sheep wool fiber on fresh and hardened properties of fiber reinforced concrete. *Int. J. Civ. Eng. Technol.* **2019**, *10*, 190–199.
11. Giosuè, C. Properties of multifunctional lightweight mortars containing zeolite and natural fibers. *J. Sustain. Cem. Mater.* **2019**, *8*, 214–227. [CrossRef]
12. Kesikidou, F.; Stefanidou, M. Natural fiber-reinforced mortars. *J. Build. Eng.* **2019**. [CrossRef]
13. EN 197-1. *Cement Part 1: Composition, Specifications and Conformity Criteria for Common Cements*; European Committee for Standardization (CEN): Brussels, Belgium, 2011.
14. EN 459-1. *Building Lime*; Part 1: Definitions, Specifications and Conformity Criteria; European Committee for Standardization (CEN): Brussels, Belgium, 2015.
15. Cahier 2669-4. *Certification CSTB Des Enduits Monocouches D'imperméabilisation, Modalités D'essais*; Centre Scientifique et Technique du Bâtiment: Marne-la-Vallée, French, 1993.
16. EN 1015-3. *Methods of Test for Mortar for Masonry—Part 3: Determination of Consistence of Fresh Mortar (by Flow Table)*; European Committee for Standardization (CEN): Brussels, Belgium, 1999.
17. EN 1015-6. *Methods of Test for Mortar for Masonry—Part 6: Determination of Bulk Density of Fresh Mortar*; European Committee for Standardization (CEN): Brussels, Belgium, 1998.
18. EN 1015-10. *Methods of Test for Mortar for Masonry—Part 10: Determination of Dry Bulk Density of Hardened Mortar*; European Committee for Standardization (CEN): Brussels, Belgium, 1999.
19. EN 14146. *Natural Stone Test Methods. Determination of the Dynamic Elastic Modulus of Elasticity (by Measuring the Fundamental Resonance Frequency)*; European Committee for Standardization (CEN): Brussels, Belgium, 2004.
20. EN 12504-4. *Testing Concrete in Structures. Part 4: Determination of Ultrasonic Pulse Velocity*; European Committee for Standardization (CEN): Brussels, Belgium, 2007.
21. EN 1015-11. *Methods of Test for Mortar for Masonry—Part 11: Determination of Flexural and Compressive Strength of Hardened Mortar*; European Committee for Standardization (CEN): Brussels, Belgium, 1999.
22. EN 1936. *Natural Stone Test Methods. Determination of Real Density and Apparent Density and Total and Partial Open Porosity*; European Committee for Standardization (CEN): Brussels, Belgium, 2007.
23. Veiga, R. Performance of Rendering Mortars. Contribution to The Study of Their Cracking Resistance. Ph.D. Thesis, University of Porto, Porto, Portugal, 1998. (In Portuguese)
24. Farinha, C.; De Brito, J.; Veiga, R. Incorporation of fine sanitary ware aggregates in coating mortars. *Constr. Build. Mater.* **2015**, *83*, 194–206. [CrossRef]
25. Santos, A.R. The Influence of Natural Aggregates on the Performance of Replacement Mortars for Ancient Buildings: The Effects of Mineralogy, Grading and Shape. Ph.D. Thesis, University of Lisbon, Lisbon, Portugal, 2019.
26. Araya-Letelier, G.; Antico, F.C.; Carrasco, M.; Rojas, P.; García-herrera, C.M. Effectiveness of new natural fibers on damage-mechanical performance of mortar. *Constr. Build. Mater.* **2017**, *152*, 672–682. [CrossRef]
27. Fantilli, A.P.; Jozwiak-niedzwiedzka, D.; Gibas, K.; Dulnik, J. The compatibility between wool fibers and cementitious mortars. In Proceedings of the International Conference on Bio-based Building Materials, Clermont-Ferrand, France, 21–23 June 2017; pp. 42–47.
28. Pereira, M.V.; Fujiyama, R.; Darwish, F.; Alves, G.T. On the strengthening of cement mortar by natural fibers. *Mater. Res.* **2015**, *18*, 177–183. [CrossRef]

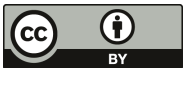

materials

MDPI

Article

Environmentally Sustainable Cement Composites Based on End-of-Life Tyre Rubber and Recycled Waste Porous Glass

Andrea Petrella *, Rosa Di Mundo, Sabino De Gisi, Francesco Todaro, Claudia Labianca and Michele Notarnicola

Dipartimento di Ingegneria Civile, Ambientale, Edile, del Territorio e di Chimica, Politecnico di Bari, Via E. Orabona 4, 70125 Bari, Italy; rosa.dimundo@poliba.it (R.D.M.); sabino.degisi@poliba.it (S.D.G.); francesco.todaro@poliba.it (F.T.); claudia.labianca@poliba.it (C.L.); michele.notarnicola@poliba.it (M.N.)
* Correspondence: andrea.petrella@poliba.it; Tel.: +39(0)805963275; Fax: +39(0)805963635

Received: 11 September 2019; Accepted: 8 October 2019; Published: 10 October 2019

Abstract: In this paper, environmentally sustainable cement mortars were prepared with end-of-life tyre rubber (TR) and recycled waste porous glass (PG) as aggregates in order to obtain lightweight products characterized by renewable and not-pretreated materials specifically for indoor applications. The secondary raw materials were added as partial and/or total replacement of the conventional sand aggregate. The resulting lightweight specimens were characterized by rheological, mechanical, thermal, microstructural and wettability tests. Fine tyre rubber aggregates affected the cohesiveness of the composites, as opposite to coarse tyre rubber and porous glass. The flexural and the compressive strengths of the porous glass samples were higher than the tyre rubber samples because of the higher stiffness and good adhesion of the glass to the cement paste as observed by microstructural observations. On the contrary, an unfavorable adhesion of the tyre aggregates to the cement paste was observed, together with discrete cracks after failure without separation of the two parts of the specimens. The latter result can explain the best results obtained by tyre rubber mortars in the case of impact compression tests where the super-elastic properties of the elastomeric material were evidenced by a deep groove before complete failure. Moreover, the thermal conductivity decrease of the lightweight porous TR and PG composites was in the range of ~80–90% with respect to the sand-based samples, which suggests that they can be used as plasters and masonries, and, in the case of tyre rubber specimens, outside applications are not excluded as observed from the wettability tests.

Keywords: cement composites; recycled waste porous glass; end-of-life tyre rubber; safe production; thermal insulation; mechanical resistance

1. Introduction

The recycling of industrial by-products is an ever rising issue in the sustainable waste management field. Indeed, many studies have focused on the conversion, after appropriate procedures, of these secondary raw materials into a new resource that would otherwise be landfilled. In this respect, over the last years, industrial waste recycling and reuse have become important environmental challenges that many countries are facing in order to reduce overall costs and negative environmental impacts [1–10].

Waste glass and tyre rubber are among the most recycled secondary raw materials from industrial and municipal activities, accordingly, various investigations, mainly in sustainable construction technology, have been carried out with the aim to face the problems relative to the disposal space limitations of these by-products associated with the increasing costs [8,11–17].

In recent years, the amount of waste glass has gradually increased due to the widespread development of urban areas and industries. After the forming process, different types of glass products

can be obtained, specifically container glass, flat glass, light bulbs, fluorescent and cathode ray tubes. The biopersistence and chemical inertia of these products lead to long-term accumulation. Accordingly, in the ambit of environmentally sustainable management policies, glass needs to be reused and/or recycled. This material can be indefinitely recycled by preserving the original properties [18,19], and accordingly, the products collected during the sorting operations can be used for the production of abrasives, reflective paints for highways, cullets in glass production, lubricants, additives, fractionators, in road beds and fiberglass production [19–23].

In the last 20 years, recycled glass has been widely used in construction materials, specifically in bricks, normal concrete, pavement materials and asphalt concrete [19,24–28], which is a practice that reduces landfill operations and consumption of natural resources, and also minimizes greenhouse emissions [18,29]. In this respect, it is worth saying that in the case of building materials, recycled glass as aggregate in structural concrete is still not widely used.

The growing amount and disposal of waste tyre rubber has become an environmental issue in many countries. Every year, millions of end-of-life tyres are discarded all over the world and stockpiled tyres represent a threat to human health and the environment through air, water and soil pollution, with its associated economic and social risks [15,30]. The volume of waste, which is globally produced, makes management of the accumulated rubber very hard, with potential fire risks. Tyre burning, although easy and cheap, represents an extremely dangerous method of disposal because fires are difficult to be extinguished and uncontrolled emission of hazardous compounds and potentially toxic gases are released in air. This is very dangerous to humans, animals and plants, and causes ground and surface water contamination generated by the oils and residue ashes left after burning [31,32]. Tyre rubber may be also used as fuel after carbon black production but this solution is not economically advantageous because this material has lower quality and higher costs as compared to conventional fuels [15].

Due to the biopersistence and chemical inertia of waste rubber, recycling operations are rising issues in the sustainable waste management field, as an alternative to landfilling, along with the awareness that new products can be produced with different properties with respect to the original materials.

Tyre rubber can be used for applications in civil and non-civil engineering, for example in erosion control, earthquake shock-wave absorption, road construction as a modifier in asphalt paving mixtures, in breakwaters, in crash and sound barriers, in reefs, playground equipment, as a fuel in cement kilns or for electricity production after incineration [14,16,33–35].

Over the last few years, waste tyre rubber incorporation into cement concrete has been considered one of the most effective, cheap and eco-friendly recycling solutions because it contributes to reducing the cost of some natural aggregates, the great volume of tyre waste, and the emission of toxic compounds and carbon dioxide by preventing tyre fires [36–39].

The main purpose of the present research was to prepare and characterize, by physico-mechanical procedures, eco-friendly non-structural cement composites based on inorganic and organic by-products of recycled waste porous glass (PG) and end-of-life tyre rubber (TR). The secondary raw materials were added as partial and/or total replacement of the conventional sand aggregate, which was made on a volume basis rather than on a weight basis due to the low specific weight of both waste materials. The specimens were characterized by rheological, mechanical, thermal, porosimetric, microstructural and wettability tests. The aim was to obtain lightweight thermo-insulating composites specifically for indoor applications in perfect agreement with the current policies of environmental sustainability. They are also cost-effective because they are prepared through a cheap process where the renewable aggregates are not pre-treated (no addition of chemicals to improve adhesion to the cement paste) and the mixture preparation does not require complex manufacturing processes or expensive procedures.

2. Experimental Part

2.1. Materials and Mortar Specimens Preparation

CEM II A-LL 42.5 R (limestone Portland cement, $R_{c\ (2\ days)} > 25.0$ MPa, $R_{c\ (28\ days)} > 47.0$ MPa, 3100–4400 cm^2/g Blaine specific surface area) was provided by Buzzi Unicem (Barletta, Italy) and used for the preparation of the cement mortars [40]. Conventional sand (normalized) was characterized as clean, isometric and rounded in shape grains in the 0.08–2 mm size range (1660 kg/m^3) and provided by Societè Nouvelle du Littoral, Leucate, France [41,42]. End-of-life tyre rubber (TR) (0–0.5 mm and 0.5–2 mm size range, 460 kg/m^3 and 500 kg/m^3, respectively) and recycled porous waste glass (PG) (0.5–2 mm size range, 300 kg/m^3) were provided by Maltek Industrie S.r.l., Terlizzi, Bari, Italy. PG is a sodium calcium silicate glass (71% SiO_2, 9% CaO, 14% Na_2O, 3% Al_2O_3, 2% MgO, 1% K_2O) obtained from separate collection and separation of municipal and industrial solid wastes. Preliminary cleaning and crushing of the raw materials is followed by the addition of a porosizing agent at temperatures of 900–1300 °C, which induces a controlled porosity of the resulting beads, thus showing a specific weight in the 200–900 kg/m^3 range. TR and PG were added as partial and/or total replacement of the conventional aggregate, which was made on a volume basis rather than on a weight basis due to the low specific weight of both waste materials. In the present case, the total volume of aggregate was set at 500 cm^3 in order to preserve an acceptable workability of the mixture. For this purpose, another sand reference (sand, sample 2) with the same aggregate volume (500 cm^3) and with a 0.5–2 mm sand size range (1880 kg/m^3) was prepared. Tables 1 and 2 report the aggregate types used for the mortar preparation and the composition of the conglomerates. In the present case, the composites were prepared with a water/cement ratio equal to 0.5, specifically with 225 g of water and 450 g of cement; dosages that were chosen according to the standard protocol [41] for the normalized mortar preparation, showing a plastic behavior. After the mixture, the rheology of the fresh mixtures was evaluated by the flow-test [43]. The mortars were placed inside a truncated cone shape ring. After demolding, fifteen hits in fifteen seconds were applied. Flow data were calculated through the following empirical equation after evaluation of the diameters of the mixture before (D_i) and after (D_m) the test:

$$\%flow = \frac{[(D_m - D_i)]}{D_i} * 100 \quad (1)$$

The percentage increase of the diameter of the non-consolidated sample over the base diameter represents the flow of a specimen.

Successively, all the specimens were molded in the form of prisms (40 mm × 40 mm × 160 mm) for the flexural and compressive tests and cured in water for 7, 28, 60 and 90 days after demolding [41]. Moreover, the specimens were molded in the form of cylinders for thermal (φ = 100 mm; H = 50 mm) and impact resistance (φ = 150 mm; H = 60 mm) tests and cured in water for 28 days after demolding.

Table 1. Mortars composition.

Sample	Cement (g)	Water (g)	Sand Volume (cm^3)	TR_f Volume (cm^3)	TR_c Volume (cm^3)	PG Volume (cm^3)
Norm	450	225	810	0	0	0
Sand	450	225	500	0	0	0
TR_f	450	225	0	500	0	0
TR_c	450	225	0	0	500	0
PG	450	225	0	0	0	500
TR_f/Sand	450	225	250	250	0	0
TR_f/TR_c	450	225	0	250	250	0
TR_f/PG	450	225	0	250	0	250

Porosimetric measurements of the resulting mortars were carried-out by Ultrapyc 1200e Automatic Gas Pycnometer, Quantachrome Instruments, Boynton Beach, FL, USA. In this respect, helium gas penetrates the finest pores of the material and the results were the average of three measurements performed on three specimens of the same type (see Table 2).

Table 2. Type, aggregate composition, specific weight ρ and porosity of the cement mortar specimens. Samples prepared with 225 g of water and 450 g of cement. TR_f = fine tyre rubber, TR_c = coarse tyre rubber, PG = porous glass.

Sample	Type	Aggregate Composition	ρ Kg/m^3	Porosity %
1	Norm	Normalized sand	1980	22
2	Sand	100% Sand (0.5–2 mm)	1900	25
3	TR_f	100% TR (0–0.5 mm)	1060	46
4	TR_c	100% TR (0.5–2 mm)	1080	47
5	PG	100% PG (0.5–2 mm)	840	57
6	TR_f/Sand	50% TR (0–0.5 mm)/50% Sand (0.5–2 mm)	1380	40
7	TR_f/TR_c	50% TR (0–0.5 mm)/50% TR (0.5–2 mm)	1080	45
8	TR_f/PG	50% TR (0–0.5 mm)/50% PG (0.5–2 mm)	980	52

2.2. Microscopical Characterization

A scanning electron microscope (SEM) was used to show magnified images of the aggregates and of the cement composites. For this purpose, a FESEM-EDX Carl Zeiss Sigma 300 VP (Carl Zeiss Microscopy GmbH, Jena, Germany) electron microscope was used and the samples were sputtered with gold after immobilization onto aluminum stubs (Sputter Quorum Q150 Quorum Technologies Ltd, East Sussex, UK). The elemental composition of the different organic and inorganic areas of the samples was obtained by energy dispersive X-ray (EDX) analysis (Oxford Instruments, X-Max 20, Abingdon-on-Thames, UK). Specifically, sand composition was: C (4%), O (52%), Si (35%), Ca (2%), end-of-life tyre rubber composition was: C (25%), O (70%), S (1.5%), recycled porous waste glass was: Na (14.8%), Mg (2.1%), Al (3.5%), Si (66%), K (1%), Ca (12%), cement paste composition was: C (4.2%), O (40%), Si (7.6%), Ca (44%), Fe (1.5%), Al (2.5%). A homemade system (premier series dyno-lyte portable microscope and background cold lighting) allowed us to evaluate the wettability of the specimens, which was carried out after deposition of a drop of water onto the side and fracture surface of each sample.

2.3. Mechanical and Thermal Tests

The flexural and compression tests were carried-out by the use of a MATEST device, Milan, Italy. Compression strengths were obtained on twelve semi-prisms (loading rate in the range of 2400 ± 200 N/s), deriving from the flexural tests carried-out on six prisms (40 mm × 40 mm × 160 mm) (loading rate in the range of 50 ± 10 N/s) [41].

An impact resistance device was made according to the ACI Committee 544 [44]. Specifically, the test was carried-out by dropping a weight of 4.50 kg from a height of 45 cm above a steel ball (63 mm diameter) placed centrally on the upper surface of the specimen. The energy absorbed by the sample before the fracture was obtained after evaluation of the number of blows on the sphere.

Thermal conductivity (λ) and thermal diffusivity (α) measurements were carried-out through an ISOMET 2104 device, from Applied Precision Ltd. (Bratislava, Slovakia). Before the tests, the mortars were dried to a constant weight, followed by final stabilization at room temperature. Specifically, a constant thermal flow was produced by a heating probe that was applied on the sample surface and the temperature was recorded over time. The thermal diffusivity and thermal conductivity parameters

were obtained by comparison between the experimental temperature values and the analytical solution of the heat conduction equation [45].

3. Results and Discussion

3.1. Characterization of the Aggregates and Rheological Tests of the Mortars

Figure 1 shows the scanning electron micrographs (SEM) of tyre rubber grains and of PG beads. An intrinsic micro-scale texture of the elastomeric aggregates can be observed (Figure 1A), while the glass aggregates (Figure 1B) show a large open porosity together with a large closed porosity (inset Figure 1B). The properties of these secondary raw materials can explain the properties of the resulting mortars. In this respect, Table 2 shows that the TR and PG samples are lighter and with a much higher porosity than the references, while, among the lightweight composites, PG mortars were the most porous.

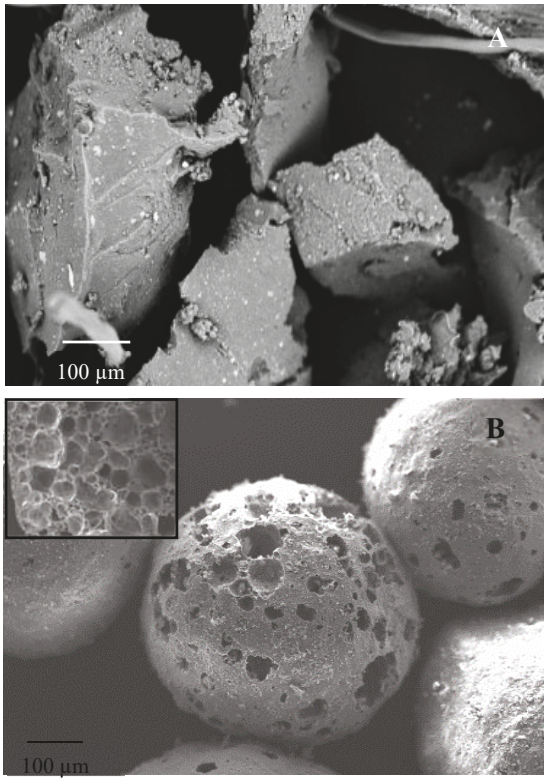

Figure 1. (**A**) Tyre rubber (TR) grain and (**B**) porous glass (PG) bead with evidenced porosity (in the inset: inner porosity).

Flow-test measurements were carried-out on the mixtures in order to determine the consistency of the fresh specimens (Figure 2).

Sample 2 (sand sample) showed a higher flow (+56%) than the control (normalized mortar (norm), with a plastic behavior) due to the lack of fines in the sand aggregate. The sample with bare fine tyre rubber aggregates (sample 3) showed a flow decrease in the range of 44.5% with respect to the reference [46], as opposite to sample 4 with bare coarse tyre rubber aggregates, which showed approximately the same flow as the control (+9%). The former result is ascribed to the absence of

the fine aggregates, with a higher specific surface, which contributes to the decrease of plasticity and increase of cohesiveness of the specimen. Sample 6, with fine TR and coarse sand, showed a plastic behavior as the flow was similar to the control (+8%), while the PG composite (sample 5) showed a flow increase in the range of 30% because of the absence of fine aggregates. Finally, the presence of the finer TR fraction is associated with the decrease of workability of the samples 7 and 8 (−25%).

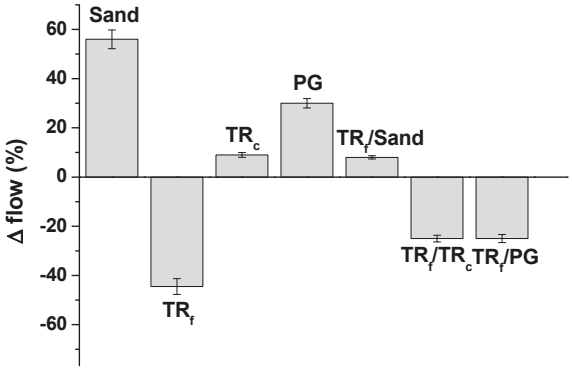

Figure 2. Flow-test results with respect to the normalized mortar (norm sample).

3.2. Mechanical Tests and Microscopical Characterization of the Mortars

Figures 3 and 4 report the flexural and compressive strengths of the samples. Reference sand-based mortars (samples 1 and 2) showed the best mechanical performances. In fact, the flexural and compressive strengths of all the unconventional and lightweight mortars were lower than the references, based on the more resistant sand aggregate.

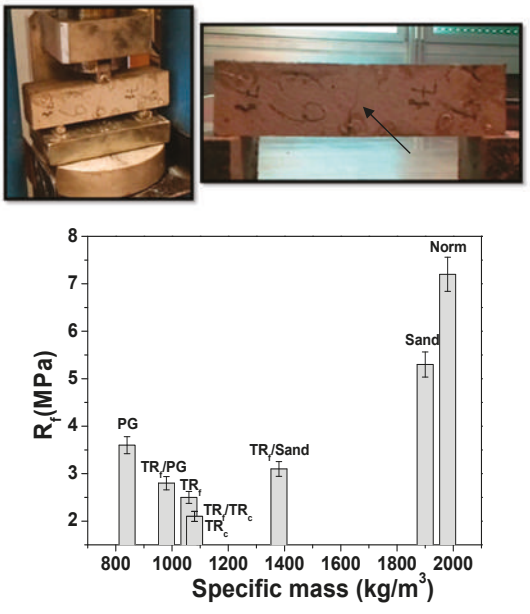

Figure 3. Flexural strengths of the cement mortars. On the top: discrete cracks after rupture in the TR specimens (evidenced by the arrow), with the two parts of the sample still connected by the tyre rubber.

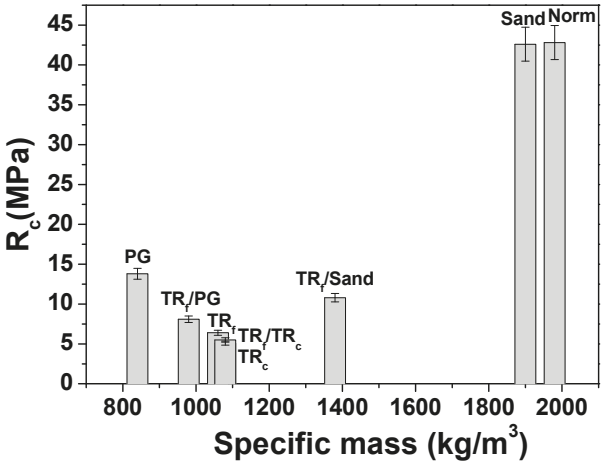

Figure 4. Compressive strengths of the cement mortars.

As for specimens 3, 4 and 7, characterized by bare tyre rubber, the addition of the elastomeric waste disrupted the mineral skeleton of the mortars after the formation of voids in the composite, which sensibly reduced the specific weight of the samples.

This effect depends on the organic/inorganic interface properties. In fact, an unfavorable adhesion of the aggregate to the cement paste [46–52] was observed and ascribed to the hydrophobic nature of the tyres rubber and to the completely different chemistry of the compounds present in the polymeric structure and in the inorganic matrix (Figure 5A). This evidence was not observed in the sand-based references where a good aggregate/cement paste adhesion was present (Figure 5B).

Accordingly, after total replacement of the sand volume, a decrease in the mechanical performances of these composites was ascribed to the low density of the TR grains and to the voids (entrapped air) created by the aggregate at the cement/TR interface during mixing, which can explain the decrease of the specific weight and an almost double porosity of these samples with respect to the references [46–52] (Table 2).

Specifically, the flexural resistances of samples 3, 4 and 7 were 60–70% lower than the references, while the compressive resistances were ~85% lower than the references (Figures 3 and 4). Replacement of 50% of the sand volume with TR grains (sample 6) led to an increase in the mechanical resistances with respect to the composites with 100% sand replacement, due to the presence of the more resistant sand aggregate. In fact, in this case, the flexural strength decrease was approximately 40–55% with respect to both references, while the compressive resistances were ~70% lower than the reference samples [51,53–57]. The specimen with fine tyre rubber aggregates (samples 3) showed higher mechanical resistances than the coarse tyre rubber type (samples 4), as was also observed in previous works [53–56], a result ascribed to the higher surface area of the fine type elastomeric materials, which, as observed in rheological measurements, improve the cohesiveness of the mixture. Mortars based on PG and PG/TR aggregates (samples 5 and 8) showed an increase in the flexural and compressive strengths with respect to tyre rubber composites, in particular the flexural resistance of sample 5 (PG specimen) was almost double the other tyre rubber samples (samples 3, 4 and 7) together with a three times higher increase of the compressive strength. Moreover, the PG composites showed a decrease in the flexural resistances in the range of 25–50% (sample 5) and 50–60% (sample 8) with respect to the references, and a decrease in the compressive resistances in the range of ~65% (sample 5) and ~80% (sample 8) with respect to the references [58–60]. The presence of tyre rubber was detrimental for the mechanical strengths, which conversely were interesting when bare PG was used because glass showed higher stiffness and better adhesion to the cement paste due to the high roughness of the beads

and to a chemical composition (silicates, aluminates) similar to the ligand matrix (Figure 5C) [11,61]. For this reason, the lowest specific weight of the glass samples was exclusively ascribed to the intrinsic porosity of the aggregate and not to the porosity of the composite at the interface. Table 3 shows the results obtained from the mechanical tests.

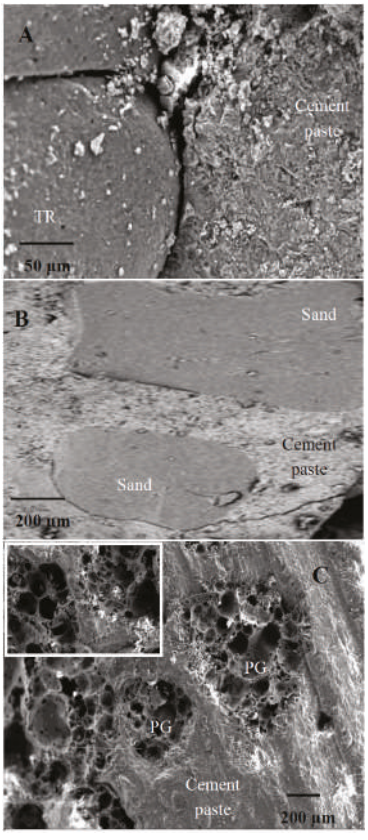

Figure 5. SEM images of: (**A**) cement/TR interface, (**B**) cement/sand interface, (**C**) cement/PG interface.

The flexural failure mode of the mortars containing bare TR aggregate did not exhibit the typical brittle behavior observed in the conventional sand-based samples (samples 1 and 2), indeed a separation of the two parts of the specimens was not observed but only discrete cracks, ascribed to the tyre tensile strength (Figure 3, on top) [53,62].

Similar to flexural strength observations, the compressive failure observed in the case of TR mortars was more gradual and the specimens showed a high-energy absorption capacity because of the load retention after failure without collapse. It was also observed that many aggregates of the TR specimens sheared off along the failure plane, and accordingly, the bond between the TR aggregate and the cement paste was stronger than the failure strength of the aggregate granules. Reference samples and sample 5 (based on bare PG) showed a typical brittle failure [60,63–65]. A semi-brittle failure was observed in the case of the Sand-TR and of the PG/TR samples (sample 6 and 8). The R_c values of the PG, TR_f/Sand and TR_f/PG samples were in the CS IV conformity range for plasters, while the R_c values of the TR_f, TR_c and TR_f/TR_c samples were in the CS III conformity range for plasters [66]. The R_c values of the PG and TR_f/Sand samples were in the M10 conformity range for masonries, while the R_c values of TR_f/PG, TR_f, TR_c and TR_f/TR_c were in the M5 conformity range for masonries [67].

Table 3. Main results from flexural (R_f), compressive (R_c), impact resistance (IR) and thermal tests (λ).

Sample	$R_{f\ (28d)}$ (MPa)	$R_{c\ (28d)}$ (MPa)	IR (J/cm^2)	λ (W/mK)
Norm	7.2	42.8	4.5	1.95
Sand	5.3	42.6	3.2	1.6
TR_f	2.5	6.4	51.6	0.3
TR_c	2.1	5.1	19.1	0.3
PG	3.6	13.8	1.3	0.2
TR_f/Sand	3.1	10.8	6.4	0.7
TR_f/TR_c	2.1	5.5	22.3	0.25
TR_f/PG	2.8	8.1	11	0.3

Figure 6 shows a picture of the sections of the specimens after the mechanical tests, where the nature of the aggregates can be observed together with a good distribution of the tyre rubber grains, porous glass beads and conventional sand. The samples, although characterized by different types of aggregates and with different grain size distribution, were extremely homogenous without any form of segregation.

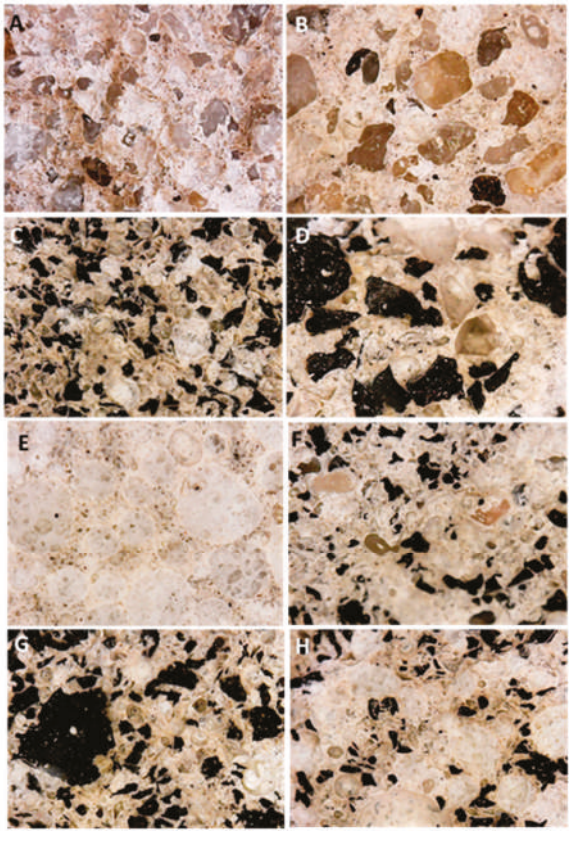

Figure 6. Sections of the specimens after the mechanical tests. (**A**) Norm (sample 1), (**B**) Sand (sample 2), (**C**) TR_f (sample 3), (**D**) TR_c (sample 4), (**E**) PG (sample 5), (**F**) TR_f/Sand (sample 6), (**G**) TR_f/TR_c (sample 7), (**H**) TR_f/PG (sample 8).

The temporal evolution of the flexural and compressive resistances of samples 3, 4, 5 and 8 is reported in Figure 7. An increase in the strengths can be observed for every composite with a final stabilization in the range of 60–90 days. This result may demonstrate a stability of the materials, in consideration of the adopted curing/conservation conditions of the conglomerates (in water).

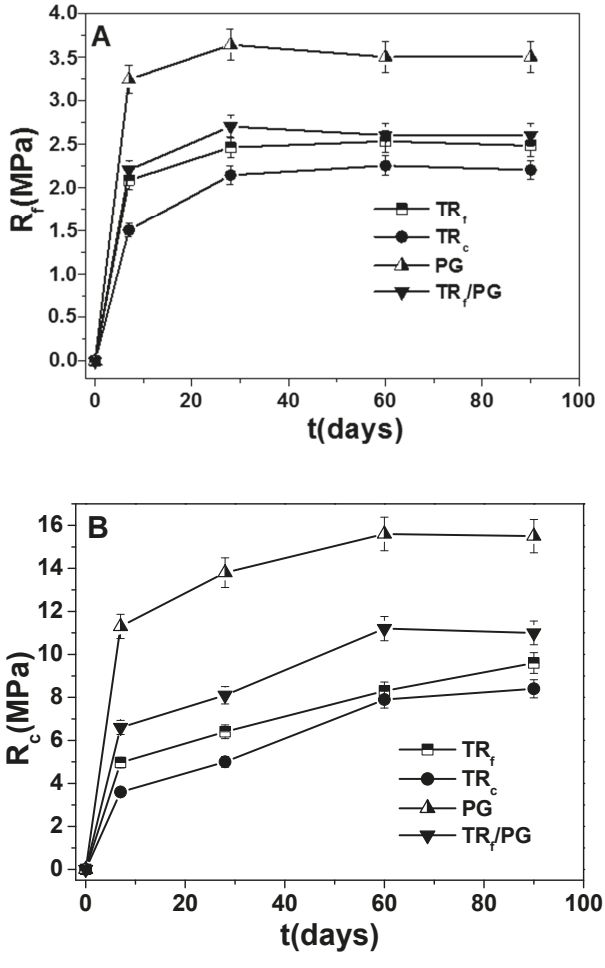

Figure 7. Temporal evolution of the (**A**) flexural and (**B**) compressive resistances of sample 3 (TR_f), sample 4 (TR_c), sample 5 (PG) and sample 8 (TR_f/PG).

From the impact compression tests (Figure 8A), it was observed that the references and the PG mortars (samples 1, 2 and 5) were extremely fragile, with a relatively low number of blows necessary for fracture formation (Figure 8D,E).

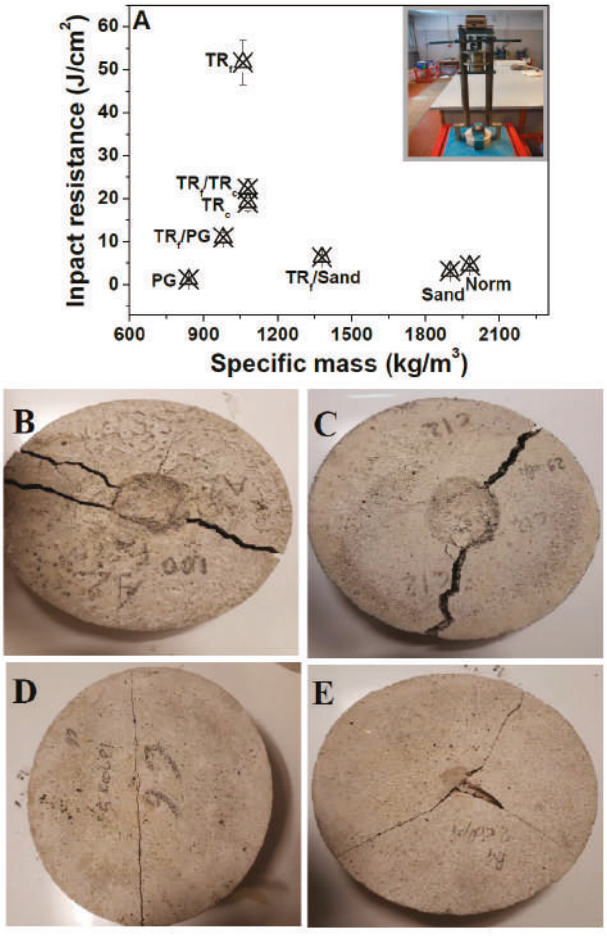

Figure 8. (**A**) Impact resistance of the cement mortars, (**B**) TR_f (sample 3), (**C**) TR_f/TR_c (sample 7), (**D**) Norm (sample 1), (**E**) PG (sample 5).

The best results were obtained with the TR specimens because of the load retention of these composites, ascribed to the super-elastic properties of the elastomeric material and evidenced by a deep groove before complete failure (Figure 8B,C) [46,68]. Specifically, sample 3 with finer grains showed the highest energy absorption capacity ascribed to a better compaction with respect to the other similar composites. As for the flexural and compressive tests, average values were observed in samples with 50% of TR (samples 6 and 8) because of the presence of brittle materials as sand and PG.

3.3. Thermal Tests

TR-based mortars (samples 3, 4 and 7) showed lower thermal conductivities and diffusivities (80–85%) as compared to the sand equivalent controls (Figure 9) because of the lower specific weight of the specimens due to the polymer characteristics (low specific weight of the aggregate) and also to the voids (entrapped air) at the TR/cement paste interface, which limit heat transport through the material (see Figure 5A) [50,68]. The best results were obtained in the case of the PG mortar (0.2 W/mK, sample 5). Specifically, a corresponding decrease (~90%) of the thermal conductivity with respect to the controls was observed, a result ascribed to the large porosity of the glass beads, which induces a

further increase in the thermal insulation (see Figure 1B). In addition, the TR/PG mixture affected the thermal insulation. Average values (60–65%) were obtained in samples with the presence of 50% of sand (sample 6). An exponential decrease in the conductivity and diffusivity data was observed with the decrease in the conglomerates specific weight. Table 3 also shows the results obtained from the thermal tests.

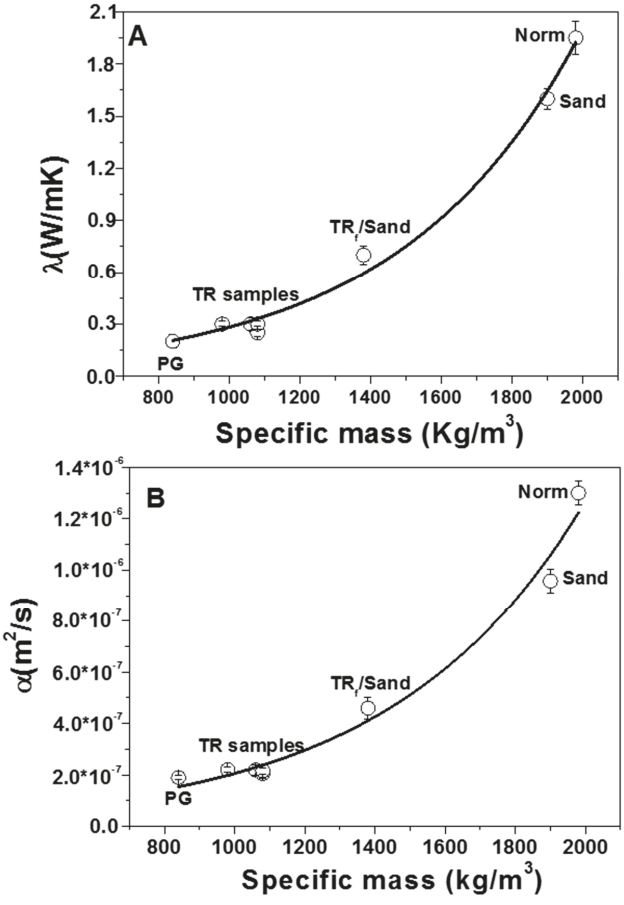

Figure 9. (**A**) Thermal conductivity and (**B**) thermal diffusivity of the cement mortar specimens.

3.4. Wettability Tests

An investigation on the wettability of the tyre rubber specimens was carried out in a previous work [52]. In the present paper, it was completed with the comparison of the properties of the porous glass mortars. As known, the wettability is the ability of a liquid to maintain contact with a solid surface, thus a hydrophobic behavior is associated with surfaces that repel water (poor wettability), while a hydrophilic behavior is associated with a favorable wettability of the surfaces [69]. A surface is considered hydrophobic if the water contact angle is higher than 90°, whereas a surface is considered hydrophilic if the water contact angle is lower than 90°. As has also been formerly observed [52], the surface and the bulk of the sand-based samples (norm and sand) showed an average fast water absorption and a hydrophilic behavior (water contact angle lower than 90°) due to the hydrophilic porous domains of the cement paste (Figure 10A). Similar results were obtained in the case of the

porous glass mortar (PG), a result ascribed to the hydrophilic nature and the high porosity of the soda-lime aggregate (Figure 5C), together with the presence of the hydrophilic porous domains of the cement paste, which determine a fast penetration of water (Figure 10B). Tyre-rubber specimens (TR_f, TR_c, TR_f/TR_c) showed a strong reduction in water penetration both on the surface and on the bulk and a hydrophobic behavior (water contact angle higher than 90° [52]), although these samples were more porous than the references (poor adhesion of the aggregate to the cement paste, see Figure 5A). These results were totally ascribed to the hydrophobic nature of the organic aggregate. Maximum hydrophobic performances were obtained in the presence of the finer tyre rubber grain size distribution (TR_f, Figure 10C). In addition, in the case of the rubber/sand sample (TR_f/Sand) the water absorption was significantly lower than the reference samples (~15% on the side surface, ~25% on the fracture surface), but higher than the TR-mortars due to the halved volume of rubber, which dramatically reduced the net force for water penetration and thus stabilized the deposited drops on the surface [52]. Interestingly, the rubber/glass sample (TR_f/PG) showed a low water absorption (~10% on the side surface, ~15% on the fracture surface) ascribed to the contribution of the organic hydrophobic aggregate in spite of the contribution of the hydrophilic and porous glass (Figure 10D). Therefore, in this case, the rubber contributed to the reduction of the net force for water penetration, thus stabilizing the deposited drops on the surface.

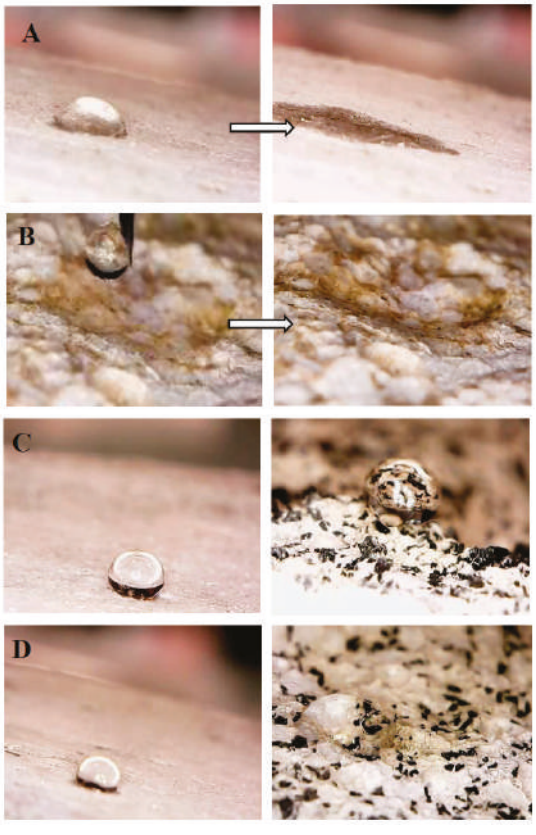

Figure 10. Wettability tests on the side surface of (**A**) Norm (sample 1) at t = 0 s (left) and at t = 60 s (right), on the fracture surface of (**B**) PG (sample 5) at t = 0 s (left) and at t = 2 s (right), on the side (left) and fracture (right) surface of (**C**) TR_f (sample 3) at t = 150 s, on the side (left) and fracture (right) surface of (**D**) TR_f/PG (sample 8) at t = 150 s.

It is worth saying that all materials showed a similar behavior because the surface and bulk of all the specimens were almost the same, which means that the mortar features cannot be modified by eventual wear or damage events of the surface.

4. Conclusions

End-of-life tyre rubber (TR) and recycled waste porous glass (PG) were employed for the production of lightweight eco-sustainable cement conglomerates specifically for indoor applications. A cheap and environmentally friendly process was used because the aggregates were not pre-treated. The secondary raw materials were added as partial and/or total replacement of the conventional sand aggregate, which was made on a volume basis rather than on a weight basis due to the low specific weight of both waste materials. The specimens were characterized by rheological, mechanical, thermal, microstructural and wettability tests.

TR and PG were added as partial and/or total replacement of the conventional aggregate, which was made on a volume basis rather than on a weight basis due to the low specific weight of both waste materials. In the present case, the total volume of aggregate was set at 500 cm^3 in order to preserve an acceptable workability of the mixture. The samples were prepared with a water/cement ratio equal to 0.5, a value that was chosen according to the standard protocol for the normalized mortar preparation, showing a plastic behavior.

The main results showed that:

(a) Fine TR aggregates affected the cohesiveness of the mixtures as opposite to coarse TR and PG types.

(b) The flexural and compressive strengths of the unconventional and lightweight mortars were lower than the references, based on the more resistant sand aggregate. Specifically, a decrease of ~60% and ~85% respectively of the flexural and compressive strengths was observed in the case of TR samples, whereas a lower decrease was observed in the case of the PG specimens (~25% and ~65% decrease respectively of the flexural and compressive strengths). The flexural and compressive strengths of the PG samples were higher than the TR samples because of the higher stiffness and good adhesion of the glass to the cement paste, ascribed to the roughness of the aggregate surface together with a chemical composition (silicates, aluminates) similar to the ligand matrix. On the contrary, an unfavorable adhesion of the rubber aggregate to the cement paste was observed and ascribed to the hydrophobic nature of the organic material and to the completely different chemical composition of the polymer and of the inorganic matrix.

(c) The specimen with fine tyre rubber aggregates showed higher mechanical resistances than the coarse tyre rubber type, a result ascribed to the higher surface area of the fine type elastomeric materials, which, as observed in rheological measurements, improves the cohesiveness of the mixture.

Replacement of 50% of the sand volume with TR grains led to an increase in the mechanical resistances with respect to the composites with 100% sand replacement, due to the presence of the more resistant sand aggregate.

(d) The flexural failure mode of the mortars containing bare TR aggregate did not exhibit the typical brittle behavior observed in the conventional sand-based samples and in the bare PG samples, indeed a separation of the two parts of the specimens was not observed but only discrete cracks were noticed and ascribed to the rubber tensile strength.

(e) From the impact compression tests it was observed that the references and the PG mortars were extremely fragile, and the best results were obtained with the TR specimens because of the load retention of these composites ascribed to the super-elastic properties of the elastomeric material and evidenced by a deep groove before complete failure.

(f) From thermal measurements it was observed that the thermal conductivity and diffusivity decrease of the lightweight materials (tyre rubber and porous glass specimens) was in the range of ~80–90% with respect to the sand-based samples. This was ascribed to the large porosity of the glass

beads and, in the case of the TR specimens, to the voids at the TR/cement paste interface, which limit heat transport through the material.

(g) Suitable applications in the construction industry as non-structural artifacts may be found for all the samples, as acceptable compressive data for plasters and masonries were obtained. Specifically, after wettability investigations, bare PG specimens may be suitable for indoor applications, while TR specimens may be also suitable for outside elements exposed for example to water flowing and capillary rise. The latter application may also be indicated for the glass/tyre rubber mortars characterized by hydrophobic behavior and low water absorption, ascribed to the presence of the organic aggregate, and by interesting mechanical resistances and high thermo-insulation, mainly ascribed to the inorganic aggregate.

Finally, it is worth considering that these waste/cement composites are cost-effective and environmentally sustainable construction materials because they are prepared through a cheap and eco-friendly process where the aggregates were not pre-treated and the mixture preparation did not require complex manufacturing processes or expensive procedures.

Author Contributions: Conceptualization, M.N.; methodology, R.D.M.; software, F.T.; validation, C.L.; formal analysis, A.P.; investigation, A.P.; data curation, S.D.G.; writing—original draft preparation, A.P.; writing—review and editing, A.P. and M.N.; supervision, M.N.

Funding: This research received no external funding

Acknowledgments: The authors wish to thank Pietro Stefanizzi and Stefania Liuzzi for thermal analysis. The authors also thank Adriano Boghetich for SEM-EDX analysis. Regione Puglia is gratefully acknowledged for financial support (Micro X-Ray Lab Project–Reti di Laboratori Pubblici di Ricerca, cod. n. 45 and 56). The Department of Civil, Environmental, Land, Construction and Chemistry (DICATECh) of the Polytechnic University of Bari is gratefully acknowledged for SEM analyses.

Conflicts of Interest: The authors declare no conflict of interest.

References

1. Geraldo, R.H.; Pinheiro, S.M.; Silva, J.S.; Andrade, H.M.; Dweck, J.; Gonçalves, J.P.; Camarini, G. Gypsum plaster waste recycling: A potential environmental and industrial solution. *J. Clean. Prod.* **2017**, *164*, 288–300. [CrossRef]
2. Gu, F.; Guo, J.; Zhang, W.; Summers, P.A.; Hall, P. From waste plastics to industrial raw materials: A life cycle assessment of mechanical plastic recycling practice based on a real-world case study. *Sci. Total Environ.* **2017**, *601*, 1192–1207. [CrossRef] [PubMed]
3. Singh, N.; Hui, D.; Singh, R.; Ahuja, I.P.S.; Feo, L.; Fraternali, F. Recycling of plastic solid waste: A state of art review and future applications. *Compos. Part B Eng.* **2017**, *115*, 409–422. [CrossRef]
4. Sienkiewicz, M.; Janik, H.; Borzędowska-Labuda, K.; Kucińska-Lipka, J. Environmentally friendly polymer-rubber composites obtained from waste tyres: A review. *J. Clean. Prod.* **2017**, *147*, 560–571. [CrossRef]
5. Liuzzi, S.; Rubino, C.; Stefanizzi, P.; Petrella, A.; Boghetich, A.; Casavola, C.; Pappalettera, G. Hygrothermal properties of clayey plasters with olive fibers. *Constr. Build. Mater.* **2018**, *158*, 24–32. [CrossRef]
6. Petrella, A.; Spasiano, D.; Acquafredda, P.; De Vietro, N.; Ranieri, E.; Cosma, P.; Rizzi, V.; Petruzzelli, V.; Petruzzelli, D. Heavy metals retention (Pb (II), Cd (II), Ni (II)) from single and multimetal solutions by natural biosorbents from the olive oil milling operations. *Process Saf. Environ.* **2018**, *114*, 79–90. [CrossRef]
7. Leng, Z.; Padhan, R.K.; Sreeram, A. Production of a sustainable paving material through chemical recycling of waste PET into crumb rubber modified asphalt. *J. Clean. Prod.* **2018**, *180*, 682–688. [CrossRef]
8. Yao, Z.; Ling, T.C.; Sarker, P.K.; Su, W.; Liu, J.; Wu, W.; Tang, J. Recycling difficult-to-treat e-waste cathode-ray-tube glass as construction and building materials: A critical review. *Renew. Sustain. Energy Rev.* **2018**, *81*, 595–604. [CrossRef]
9. Coppola, L.; Bellezze, T.; Belli, A.; Bignozzi, M.C.; Bolzoni, F.; Brenna, A.; Cabrini, M.; Candamano, S.; Cappai, M.; Caputo, D.; et al. Binders alternative to Portland cement and waste management for sustainable construction-part 1. *J. Appl. Biomater. Funct. Mater.* **2018**, *16*, 186–202.

10. Coppola, L.; Bellezze, T.; Belli, A.; Bignozzi, M.C.; Bolzoni, F.; Brenna, A.; Cabrini, M.; Candamano, S.; Cappai, M.; Caputo, D.; et al. Binders alternative to Portland cement and waste management for sustainable construction-part 2. *J. Appl. Biomater. Funct. Mater.* **2018**, *16*, 207–221.
11. Petrella, A.; Spasiano, D.; Race, M.; Rizzi, V.; Cosma, P.; Liuzzi, S.; De Vietro, N. Porous waste glass for lead removal in packed bed columns and reuse in cement conglomerates. *Materials* **2019**, *12*, 94. [CrossRef] [PubMed]
12. Kim, K.; Kim, K. Valuable Recycling of waste glass generated from the liquid crystal display panel industry. *J. Clean. Prod.* **2018**, *174*, 191–198. [CrossRef]
13. Paul, S.C.; Šavija, B.; Babafemi, A.J. A comprehensive review on mechanical and durability properties of cement-based materials containing waste recycled glass. *J. Clean. Prod.* **2018**, *198*, 891–906. [CrossRef]
14. Kroll, L.; Hoyer, S.; Klaerner, M. Production technology of cores for hybrid laminates containing rubber powder from scrap tyres. *Procedia Manuf.* **2018**, *21*, 591–598. [CrossRef]
15. Thomas, B.S.; Gupta, R.C. A comprehensive review on the applications of waste tire rubber in cement concrete. *Renew. Sustain. Energy Rev.* **2016**, *54*, 1323–1333. [CrossRef]
16. Presti, D.L.; Izquierdo, M.A.; del Barco Carrión, A.J. Towards storage-stable high-content recycled tyre rubber modified bitumen. *Environments* **2018**, *172*, 106–111. [CrossRef]
17. Ramirez-Canon, A.; Muñoz-Camelo, Y.; Singh, P. Decomposition of used tyre rubber by pyrolysis: Enhancement of the physical properties of the liquid fraction using a hydrogen stream. *Environments* **2018**, *5*, 72. [CrossRef]
18. Sobolev, K.; Turker, P.; Soboleva, S.; Iscioglu, G. Utilization of waste glass in ECO cement, strength properties and microstructural observations. *Waste Manag.* **2006**, *27*, 971–976. [CrossRef] [PubMed]
19. Silva, R.V.; De Brito, J.; Lye, C.Q.; Dhir, R.K. The role of glass waste in the production of ceramic-based products and other applications: A review. *J. Clean. Prod.* **2017**, *167*, 346–364. [CrossRef]
20. Chen, G.; Lee, H.; Young, K.L.; Yue, P.L.; Wong, A.; Tao, T.; Choi, K.K. Glass recycling in cement production—An innovative approach. *Waste Manag.* **2002**, *22*, 747–753. [CrossRef]
21. Sun, Z.; Shen, Z.; Ma, S.; Zhang, X. Sound absorption application of fiberglass recycled from waste printed circuit boards. *Mater. Struct.* **2015**, *48*, 387–392. [CrossRef]
22. Lu, J.X.; Duan, Z.H.; Poon, C.S. Combined use of waste glass powder and cullet in architectural mortar. *Cem. Concr. Comp.* **2017**, *82*, 34–44. [CrossRef]
23. Spasiano, D.; Luongo, V.; Petrella, A.; Alfè, M.; Pirozzi, F.; Fratino, U.; Piccinni, A.F. Preliminary study on the adoption of dark fermentation as pretreatment for a sustainable hydrothermal denaturation of cement-asbestos composites. *J. Clean. Prod.* **2017**, *166*, 172–180. [CrossRef]
24. Lachance-Tremblay, É.; Perraton, D.; Vaillancourt, M.; Di Benedetto, H. Effect of hydrated lime on linear viscoelastic properties of asphalt mixtures with glass aggregates subjected to freeze-thaw cycles. *Const. Build. Mater.* **2018**, *184*, 58–67. [CrossRef]
25. Amlashi, S.M.H.; Vaillancourt, M.; Carter, A.; Bilodeau, J.P. Resilient modulus of pavement unbound granular materials containing recycled glass aggregate. *Mater. Struct.* **2018**, *51*, 89. [CrossRef]
26. Petrella, A.; Petrella, M.; Boghetich, G.; Basile, T.; Petruzzelli, V.; Petruzzelli, D. Heavy metals retention on recycled waste glass from solid wastes sorting operations: A comparative study among different metal species. *Ind. Eng. Chem. Res.* **2012**, *51*, 119–125. [CrossRef]
27. Petrella, A.; Petruzzelli, V.; Ranieri, E.; Catalucci, V.; Petruzzelli, D. Sorption of Pb(II), Cd(II) and Ni(II) from single- and multimetal solutions by recycled waste porous glass. *Chem. Eng. Commun.* **2016**, *203*, 940–947. [CrossRef]
28. Petrella, A.; Petruzzelli, V.; Basile, T.; Petrella, M.; Boghetich, G.; Petruzzelli, D. Recycled porous glass from municipal/industrial solid wastes sorting operations as a lead ion sorbent from wastewaters. *React. Funct. Polym.* **2010**, *70*, 203–209. [CrossRef]
29. Rakshvir, M.; Barai, S.V. Studies on recycled aggregates-based concrete. *Waste Manag. Res.* **2006**, *24*, 225–233. [CrossRef]
30. Zhang, Y.; Hwang, J.Y.; Peng, Z.; Andriese, M.; Li, B.; Huang, X.; Wang, X. Microwave Absorption Characteristics of Tire. In *Characterization of Minerals, Metals, and Materials*; Carpenter, J.S., Bai, C., Pablo Escobedo-Diaz, J., Hwang, J.-Y., Ikhmayies, S., Li, B., Li, J., Neves, S., Peng, Z., Zhang, M., Eds.; Springer: Cham/Basel, Switzerland, 2015; pp. 235–243.

31. Escobar-Arnanz, J.; Mekni, S.; Blanco, G.; Eljarrat, E.; Barceló, D.; Ramos, L. Characterization of organic aromatic compounds in soils affected by an uncontrolled tire landfill fire through the use of comprehensive two-dimensional gas chromatography–time-of-flight mass spectrometry. *J. Chromatogr. A* **2018**, *1536*, 163–175. [CrossRef]
32. Artíñano, B.; Gómez-Moreno, F.J.; Díaz, E.; Amato, F.; Pandolfi, M.; Alonso-Blanco, E.; Coz, E.; Garcia-Alonso, S.; Becerril-Valle, M.; Querol, X.; et al. Outdoor and indoor particle characterization from a large and uncontrolled combustion of a tire landfill. *Sci. Total Environ.* **2017**, *593–594*, 543–551. [CrossRef] [PubMed]
33. Yang, F.; Feng, W.; Liu, F.; Jing, L.; Yuan, B.; Chen, D. Experimental and numerical study of rubber concrete slabs with steel reinforcement under close-in blast loading. *Constr. Build. Mater.* **2019**, *198*, 423–436. [CrossRef]
34. Diekmann, A.; Giese, U.; Schaumann, I. Polycyclic aromatic hydrocarbons in consumer goods made from recycled rubber material: A review. *Chemosphere* **2018**, *220*, 1163–1178. [CrossRef]
35. Czajczyńska, D.; Krzyżyńska, R.; Jouhara, H.; Spencer, N. Use of pyrolytic gas from waste tire as a fuel: A review. *Energy* **2017**, *134*, 1121–1131. [CrossRef]
36. Azevedo, F.; Pacheco-Torga, F.; Jesus, C.; de Aguiar, J.B.; Camões, A.F. Properties and durability of HPC with tyre rubber wastes. *Constr. Build. Mater.* **2012**, *34*, 186–191. [CrossRef]
37. Najim Khalid, B.; Hall Matthew, R. Mechanical and dynamic properties of self-compacting crumb rubber modified concrete. *Constr. Build. Mater.* **2012**, *27*, 521–530. [CrossRef]
38. Kovler, K.; Roussel, N. Properties of fresh and hardened concrete. *Cem. Concr. Res.* **2011**, *41*, 775–792. [CrossRef]
39. Bisht, K.; Ramana, P.V. Evaluation of mechanical and durability properties of crumb rubber concrete. *Constr. Build. Mater.* **2017**, *155*, 811–817. [CrossRef]
40. Italian Organization for Standardization (UNI). Cement Composition, Specifications and Conformity Criteria for Common Cements. EN 197-1. Available online: http://store.uni.com/magento-1.4.0.1/index.php/en-197-1-2011.html (accessed on 14 September 2011).
41. Italian Organization for Standardization (UNI). Methods of Testing Cement-Part 1: Determination of Strength. EN 196-1. Available online: http://store.uni.com/magento-1.4.0.1/index.php/en-196-1-2016.html (accessed on 27 April 2016).
42. International Organization for Standardization (ISO). Cement, Test Methods, Determination of Strength. ISO 679. Available online: http://store.uni.com/magento-1.4.0.1/index.php/iso-679-2009.html (accessed on 24 April 2009).
43. Italian Organization for Standardization (UNI). Determination of Consistency of Cement Mortars Using a Flow Table. UNI 7044:1972. Available online: http://store.uni.com/magento-1.4.0.1/index.php/uni-7044-1972.html (accessed on 20 April 1972).
44. ACI Committee 544. ACI 544.2R-89. Measurement of properties of fibre reinforced concrete. In *ACI Manual of Concrete Practice, Part 5: Masonry, Precast Concrete and Special Processes*; American Concrete Institute: Farmington Hills, MI, USA, 1996.
45. Gustafsson, S.E. Transient plane source techniques for thermal conductivity and thermal diffusivity measurements of solid materials. *Rev. Sci. Instrum.* **1991**, *62*, 797–804. [CrossRef]
46. Khalil, E.; Abd-Elmohsen, M.; Anwar, A.M. Impact resistance of rubberized self-compacting concrete. *Water Sci.* **2015**, *29*, 45–53. [CrossRef]
47. Li, G.; Wang, Z.; Leung, C.K.; Tang, S.; Pan, J.; Huang, W.; Chen, E. Properties of rubberized concrete modified by using silane coupling agent and carboxylated SBR. *J. Clean. Prod.* **2016**, *112*, 797–807. [CrossRef]
48. Huang, B.S.; Li, G.Q.; Pang, S.S.; Eggers, J. Investigation into waste tire rubberfilled concrete. *J. Mater. Civ. Eng.* **2004**, *16*, 187–194. [CrossRef]
49. Khaloo, A.R.; Dehestani, M.; Rahmatabadi, P. Mechanical properties of concrete containing a high level of tire-rubber particles. *Waste Manag.* **2008**, *28*, 2472–2482. [CrossRef] [PubMed]
50. Marie, I. Thermal conductivity of hybrid recycled aggregate–Rubberized concrete. *Constr. Build. Mater.* **2017**, *133*, 516–524. [CrossRef]
51. Karakurt, C. Microstructure properties of waste tire rubber composites: An overview. *J. Mater. Cycles Waste* **2015**, *17*, 422–433. [CrossRef]

52. Di Mundo, R.; Petrella, A.; Notarnicola, M. Surface and bulk hydrophobic cement composites by tyre rubber addition. *Constr. Build. Mater.* **2018**, *172*, 176–184. [CrossRef]
53. Aiello, M.A.; Leuzzi, F. Waste tyre rubberized concrete: Properties at fresh and hardened state. *Waste Manag.* **2010**, *30*, 1696–1704. [CrossRef]
54. Topcu, I.B. The properties of rubberized concretes. *Cem. Concr. Res.* **1995**, *25*, 304–310. [CrossRef]
55. Khatib, Z.K.; Bayomy, F.M. Rubberized Portland cement concrete. *J. Mater. Civ. Eng.* **1999**, *11*, 206–213. [CrossRef]
56. Eldin, N.N.; Senouci, A.B. Rubber-tire particles as concrete aggregate. *J. Mater. Civ. Eng.* **1993**, *5*, 478–496. [CrossRef]
57. Toutanji, H.A. The use of rubber tire particles in concrete to replace mineral aggregates. *Cem. Concr. Comp.* **1996**, *18*, 135–139. [CrossRef]
58. Kou, S.C.; Poon, C.S. Properties of self-compacting concrete prepared with recycled glass aggregate. *Cem. Concr. Comp.* **2009**, *31*, 107–113. [CrossRef]
59. Ali, E.E.; Al-Tersawy, S.H. Recycled glass as a partial replacement for fine aggregate in self compacting concrete. *Constr. Build. Mater.* **2012**, *35*, 785–791. [CrossRef]
60. Petrella, A.; Petrella, M.; Boghetich, G.; Petruzzelli, D.; Ayr, U.; Stefanizzi, P.; Calabrese, D.; Pace, L. Thermo-acoustic properties of cement-waste-glass mortars. *Proc. Inst. Civ. Eng. Constr. Mater.* **2009**, *162*, 67–72. [CrossRef]
61. Petrella, A.; Spasiano, D.; Rizzi, V.; Cosma, P.; Race, M.; De Vietro, N. Lead Ion Sorption by Perlite and Reuse of the Exhausted Material in the Construction Field. *Appl. Sci.* **2018**, *8*, 1882. [CrossRef]
62. Petrella, A.; Spasiano, D.; Liuzzi, S.; Ayr, U.; Cosma, P.; Rizzi, V.; Petrella, M.; Di Mundo, R. Use of cellulose fibers from wheat straw for sustainable cement mortars. *J. Sustain. Cem. Based Mater.* **2018**, *8*, 161–179. [CrossRef]
63. Petrella, A.; Spasiano, D.; Rizzi, V.; Cosma, P.; Race, M.; De Vietro, N. Thermodynamic and kinetic investigation of heavy metals sorption in packed bed columns by recycled lignocellulosic materials from olive oil production. *Chem. Eng. Commun.* **2019**, *206*, 1715–1730. [CrossRef]
64. Petrella, A.; Cosma, P.; Rizzi, V.; De Vietro, N. Porous alumosilicate aggregate as lead ion sorbent in wastewater treatments. *Separations* **2017**, *4*, 25. [CrossRef]
65. Petrella, A.; Petrella, M.; Boghetich, G.; Petruzzelli, D.; Calabrese, D.; Stefanizzi, P.; De Napoli, D.; Guastamacchia, M. Recycled waste glass as aggregate for lightweight concrete. *Proc. Inst. Civ. Eng. Constr. Mater.* **2007**, *160*, 165–170. [CrossRef]
66. Italian Organization for Standardization (UNI). Specification on Mortar for Masonry-Mortar for Interior and Exterior Plaster. EN 998-1. Available online: http://store.uni.com/catalogo/index.php/en-998-1-2016.html (accessed on 2 September 2019).
67. Italian Organization for Standardization (UNI). Specification on Mortar for Masonry-Masonry Mortars. EN 998-2. Available online: http://store.uni.com/catalogo/index.php/uni-en-998-2-2016.html (accessed on 2 September 2019).
68. Mastali, M.; Dalvand, A.; Sattarifard, A. The impact resistance and mechanical properties of the reinforced self-compacting concrete incorporating recycled CFRP fiber with different lengths and dosages. *Compos. Part B Eng.* **2017**, *112*, 74–92. [CrossRef]
69. Palumbo, F.; Di Mundo, R. Wettability: Significance and measurement. In *Polymer Surface Characterization*; Sabbatini, L., Ed.; De Gruyter: Berlin, Germany, 2014; pp. 207–241.

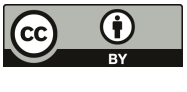

materials

MDPI

Article

Nanosilica Extracted from Hexafluorosilicic Acid of Waste Fertilizer as Reinforcement Material for Natural Rubber: Preparation and Mechanical Characteristics

Van-Huy Nguyen [1,2], Cuong Manh Vu [3,*], Hyoung Jin Choi [4,*] and Bui Xuan Kien [5]

1 Department for Management of Science and Technology Development, Ton Duc Thang University, Ho Chi Minh City 700000, Vietnam; nguyenvanhuy@tdtu.edu.vn
2 Faculty of Applied Sciences, Ton Duc Thang University, Ho Chi Minh City 700000, Vietnam
3 Center for Advanced Chemistry, Institute of Research and Development, Duy Tan University, Da Nang 550000, Vietnam
4 Department of Polymer Science and Engineering, Inha University, Incheon 22212, Korea
5 Faculty of Natural Sciences, Electric power University, 235 Hoang Quoc Viet St., Bac Tu Liem Dist, Hanoi 100000, Vietnam
* Correspondence: vumanhcuong@duytan.edu.vn or vumanhcuong309@gmail.com (C.M.V.); hjchoi@inha.ac.kr (H.J.C.)

Received: 30 July 2019; Accepted: 21 August 2019; Published: 23 August 2019

Abstract: Nanosilica particles are extracted from waste water containing a hexafluorosilicic acid discharged from Vietnamese fertilizer plants as an effective way not only to reduce waste water pollution but also to enhance the value of their waste water. Amorphous nanosilica particles are produced with diameters ranging from 40 to 60 nm and then adopted as a reinforcing additive for natural rubber (NR) composites. Morphological, mechanical, rheological, and thermal behaviors of the nanosilica-added NR composites are examined. Especially, mechanical behaviors of nanosilica-filled NR composites reach the optimum with 3 phr of nanosilica, at which its tensile strength, hardness, and decomposition temperature are improved by 20.6%, 7.1%, and 2.5%, respectively, compared with the pristine vulcanized NR. The improved mechanical properties can be explained by the tensile fractured surface morphology, which shows that the silica-filled NR is rougher than the pristine natural rubber sample.

Keywords: natural rubber; nanosilica; mechanical property; fertilizer plant; hexafluorosilicic acid; waste water

1. Introduction

While nanosilica is becoming one of the most widely used nanomaterials for many industries, with an annual growth of 5.6%, silica is used as an important filler for rubber in a range of products, such as tires and other industrial materials, because it increases its mechanical durability, heat resistance, shrinkage, thermal expansion, and stress [1–4]. In addition, it improves the wear resistance of rubber based composites by replacing a soft matrix with a hard inorganic filler. Therefore, silica-based polymer nanocomposites have many exciting features for their many applications in the automotive, electronics, marine, and other industries. Many researchers have used silica as a reinforcement material for rubber-based composites [5–9].

Mechanical characteristics of the rubber can be enhanced using nanosilica only or combined with other fillers [10,11]. In particular, high-quality silica also has an absolute advantage in the manufacture of household products (fashion footwear soles, rubber mattresses, and others) or medical rubber (gloves, boots). In the pharmaceutical industry, silica is used as a carrier for some proprietary medicines [12–14]. In the organic chemical industry, silica acts as a catalyst for some organic reactions,

helps acceleration rates, and improves reaction yields [15–18]. To meet the increasing demand for silica in industrial applications, many studies focused on the fabrication of silica from different sources [19–28]. In addition to the many common sources, such as silane compounds of Na_2SiO_3, hexafluorosilicic acid (H_2SiF_6) becomes a potential economical candidate for the production of silica. Hexafluorosilicic acid is a by-product from the fertilizer industry, produced in huge quantities annually [29]. On the other hand, it is toxic and harmful to the environment, requiring either chemical treatment or conversion to a highly economical product [30]. For example, in Vietnam, Lam Thao Fertilizers and Chemicals, the largest production company of fertilizers with an estimated capacity of approximately 850,000 tons/year, produces approximately 30,000 tons of hexafluorosilicic acid annually. The production of hexafluorosilicic acid in the fertilizer production line can be explained as follows: First, fluorapatite ($Ca_5(PO_4)_3F$ (calcium fluorophosphate)) is reacted with either H_2SO_4 or HNO_3 to generate HF according to the following reactions:

$$Ca_5(PO_4)_3F + 5H_2SO_4 + nH_2O \rightarrow 3H_3PO_4 + 5CaSO_4{\cdot}nH_2O + HF$$

Or

$$Ca_5(PO_4)_3F + 10HNO_3 \rightarrow 3H_3PO_4 + 5Ca(NO_3)_2 + HF$$

Obtained HF reacts with SiO_2, which exists in the composition of the raw materials, to form SiF_4 gas:

$$4HF + SiO_2 \rightarrow SiF_4 + 2H_2O$$

The collection of H_2SiF_6 is usually performed by an absorption method of gaseous SiF_4 in a water scrubber.

$$3SiF_4 + 2H_2O = 2H_2SiF_6 + SiO_2$$

Many groups have reported its utilization, such as in silica recovery [30–37]. Dragicevic and Hraste [38] prepared silica from the neutralization of fluosilicic acid with ammonia while Sarawade et al. [25] used Na_2CO_3 to recover mesoporous silica with a large surface area from waste H_2SiF_6 from the fertilizer company. Hexafluorosilicic acid was further adopted as a silica source to fabricate SZM-5 as a trans-alkylation catalyst [29]. Cicala et al. [39] synthesized amorphous silicon alloys from fluorinated gases by plasma deposition, while Guzeev et al. [40] produced zircon and zirconium tetrafluoride with silicon tetrafluoride and zirconium dioxide as a raw material. Liu et al. [41] also synthesized titanium containing Mobil Composition of Matter No. 41 (MCM-41) with the industrial H_2SiF_6 and applied for cyclohexene epoxidation reaction.

We report a simple method of recovering amorphous silica nanoparticles from hexafluorosilicic acid waste and their application as a reinforcing filler in natural rubber (NR) with enhanced mechanical and thermal characteristics in this study. Both fabricated nanosilica and nanosilica-added NR are characterized. These efforts could not only reduce the environmental pollution of hexafluorosilicic acid wastes, but also enhance the value of waste from a fertilizer plant as an inorganic filler of NR. Note that of the total cost for the final product in factory including the cost for raw material, equipment, energies, and waste water treatment etc., the cost for waste water treatment grows higher as a result of the government policy and type of the waste water. This results in the higher price of final products, reducing their competitiveness. In case of Vietnamese fertilizer plants, the by-product of H_2SiF_6 with its emission rate is about 35,000 tons per year. With its highly toxic and corrosive characteristics, the H_2SiF_6 solution could threaten the environment by contaminating rivers and oceans.

Therefore, we strongly believe that the production and utilization of nanosilica in this study could become a reliable and sustainable solution for dealing with waste water from fertilizer plants environmentally as well as economically.

2. Experimental Procedures

2.1. Materials

The hexafluorosilicic acid was collected from Lam Thao Fertilizers and Chemicals JSC (Phu Tho, Vietnam) and used as a raw resource for the production of nanosilica. The concentration of the hexafluorosilicic acid solution was 13 wt.% along with a very low concentration of Fe_2O_3 (0.01–0.02 wt.%) and P_2O_5 (0.001–0.01 wt.%). A 25 wt.% ammonia solution was purchased from Xilong Scientific Co. (Shantou, China). The NR (NR-Standard Vietnamese Rubber-3L) was purchased from Phuoc Hoa Rubber Co. (Binh Duong, Vietnam). We adopted 2, 2, 4-trimetyl-1, 2-dihydroquinolin (RD), N-cyclohexyl-2-benzothiazole sulfenamide (CBS), and 2, 2′-dibenzothizole disulfide (DM), (RongCheng K&S Chem., Rongcheng, China) as vulcanizing accelerators [42]. Stearic acid, zinc oxide, and sulfur were purchased from Sigma-Aldrich (St. Louis, MO, USA).

2.1.1. Recovery of Nanosilica

In the first step, pristine solutions of both hexafluorosilicic acid and ammonia were diluted with distilled water to 10 wt.% and 20 wt.%, respectively. In the second step, 200 g of 10 wt.% hexafluorosilicic acid and 110 g of 20 wt.% ammonia solution were mixed in a glass reactor vessel with a mechanical stirrer at 200 rpm for 12 h at 25 °C to obtain a slurry of nanosilica. Subsequently, the silica nanoparticles were collected with a vacuum filter under atmosphere 200 mg Hg and cleaned a couple of times with distilled water until they reached a neutral pH value. The resulting products were dried using a vacuum oven at 800 °C for 3 h and cooled to 25 °C before obtaining the final product. Figure 1 provides details of this processing.

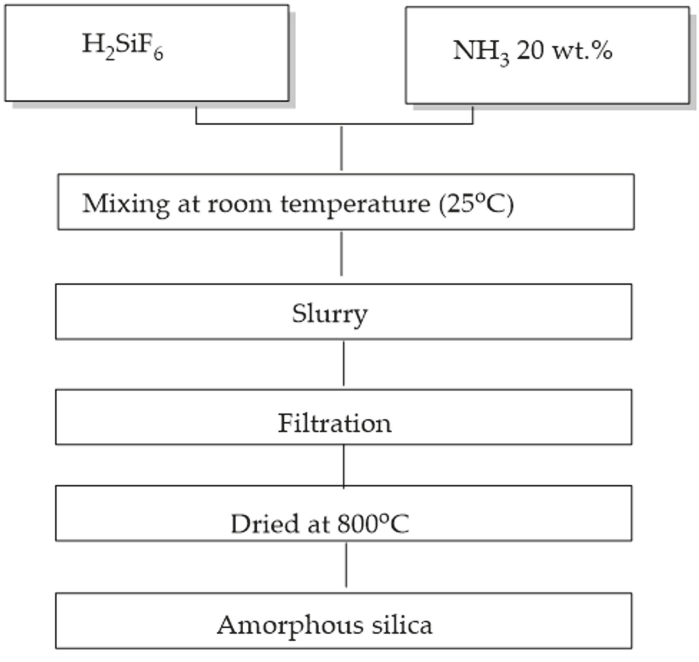

Figure 1. The processing of fabrication of nanosilica from hexafluorosilicic acid.

The material characteristics of the obtained nanosilica, such as chemical structure, crystallinity, and particle size were scrutinized by Fourier transform-infrared spectroscopy (FT-IR), X-ray diffraction (XRD), and transmission electron microscopy (TEM), respectively.

2.1.2. Rubber Compound Fabrication

The NR compounds both with and without nanosilica were fabricated following the formulations given in Table 1. Initially, the NR, ZnO, stearic acid, paraffin, and nanosilica were put into an internal mixer (Brabender Plasti-corder 350s, Brabender GmbH & Co. KG, Berlin, Germany) at different compositions depending on the sample number and mixed well at 50 °C with a rotor speed of 50 rpm for 1 h [42]. Further mixing was accomplished with a two-roll mill once three vulcanizing accelerator chemicals and sulfur were added. The rubber compounds were either used for examining curing characteristics or vulcanized to determine their mechanical properties.

Table 1. The composition of silica/natural rubber compounds.

Ingredients (phr)	M0	M1	M2	M3	M4	M5
Natural Rubber	100.0	100.0	100.0	100.0	100.0	100.0
Zinc Oxide	5.0	5.0	5.0	5.0	5.0	5.0
Stearic Acid	3.0	3.0	3.0	3.0	3.0	3.0
Parafin	1.0	1.0	1.0	1.0	1.0	1.0
RD	2.5	2.5	2.5	2.5	2.5	2.5
CBS	1.5	1.5	1.5	1.5	1.5	1.5
DM	0.5	0.5	0.5	0.5	0.5	0.5
Sulfur	2.0	2.0	2.0	2.0	2.0	2.0
Silica	0.0	1.0	3.0	5.0	7.0	10.0

2.2. Measurements

The moving die rheometer (Monsanto, MDR2000P, St. Louis, MO, USA) was used to determine the curing characteristics of NR compounds. About 5 g of rubber compound was inserted into the geometry of two parallel rotating disks at 150 °C at a frequency of 100 rpm. After processing was completed, the cure curve with many characteristics such as max. torque (M_H), min. torque (M_L), scorch time (t_2), and 90% cure time (t_{90}) were acquired.

In order to prepare the samples for tensile testing, a sheet of about 2 mm thickness was vulcanized in a molding test press (Gotech, GT7014H, Taichung, Taiwan) at 150 °C and a 40 kgf/cm^2 pressure for a respective cure time, t_{90}, which was estimated from the MDR 2000P measurement [42].

The tensile test was performed using an Instron universal testing machine according to ASTM D412-93 at room temperature (~25 °C). Tensile strengths and elongations at break were estimated from stress-strain curves and averaged values from five-time rerun measurements for each sample were obtained [34]. The Shore A hardness of the samples was evaluated following the ISO 7619-1:2010. Thermogravimetric analysis (TGA) was performed with a TGA Q50 (TA Instruments, New Castle, DE, USA) according to the ASTM D3850-94 method. Approximately 10–20 mg of vulcanized samples were loaded onto an open platinum pan, and then heated from 25 to 600 °C under a nitrogen environment at a fixed heating rate of 10 °C/min. The fracture surfaces of the fabricated nanocomposites were examined with a scanning electron microscope (SEM) (SEM JEOL 5510, JEOL, Tokyo, Japan) at 10 kV accelerating voltage.

The Mooney-Rilvin equation was used to determine the crosslinking density of the vulcanates based on the following stress-strain behavior [42]:

$$\sigma = 2(\lambda - \frac{1}{\lambda^2})(C_1 + \frac{C_2}{\lambda})$$

where σ, λ, C_1, and C_2 are the tensile stress, the strain, and constants, respectively. The C_1 and C_2 constants were determined from the slope and intercept of the curve of $\sigma/(\lambda - \lambda^{-2})$ versus 1/λ. Finally, the crosslinking density was obtained from the following equation:

$$2C_1 = \rho kT$$

where ρ is the cross-linking density, k is the Boltzmann constant, and T is the absolute temperature.

3. Results and Discussion

Initially, the chemical structure of fabricated silica nanoparticles was examined with the help of an FT-IR spectroscopy (Perkin Elmer, Waltham, MA, USA) as shown in Figure 2. The silica nanoparticles exhibited a distinctive absorption peak at 1000–1100 cm^{-1}, which was ascribed to a stretching vibration of Si–O–Si bonding. Another distinctive absorption peak also appeared at 1630 cm^{-1}, which was allocated to a bending vibration by way of H–O–H in the water molecules. An additional absorption peak was further detected at 3400 cm^{-1}, which was due to a stretching vibration of the hydroxyl group, confirming the existence of hydroxyl groups in the silica surface. Figure 2 also showed the FT-IR spectrum of vulcanized natural rubber filled with 3 phr silica composite. It is seen that the asymmetrical stretching vibration of Si–O–Si and the hydroxyl of silica in the NR/SiO_2 composite appeared at 1088 cm^{-1} and 3403 cm^{-1}, respectively.

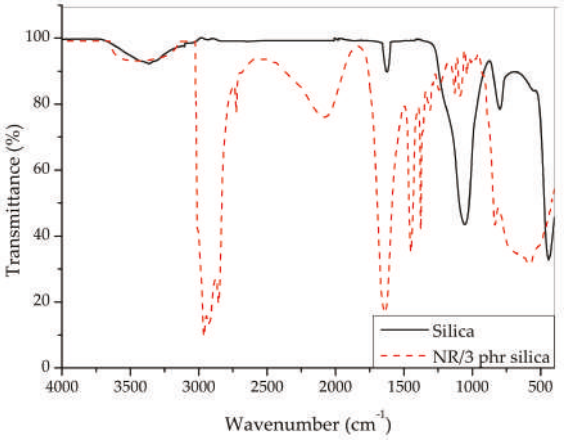

Figure 2. FT-IR spectra of fabricated nanosilica and natural rubber (NR)/3 phr silica composite.

Regarding the crystalline structure of the samples, the powder XRD pattern in Figure 3 indicated a broad peak at 22° of 2θ, revealing the amorphous nature of the nanosilica particles. Furthermore, the TEM image of nanosilica in Figure 4 showed its diameter of 40–60 nm.

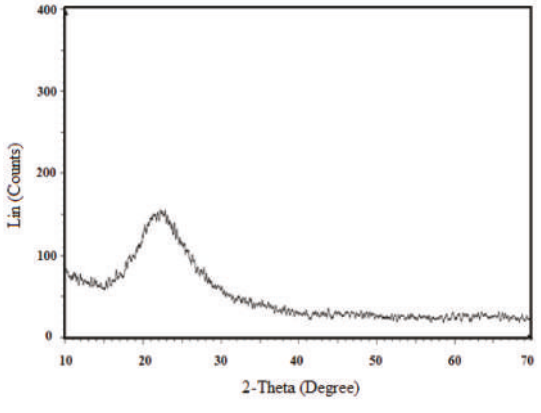

Figure 3. XRD pattern of nanosilica.

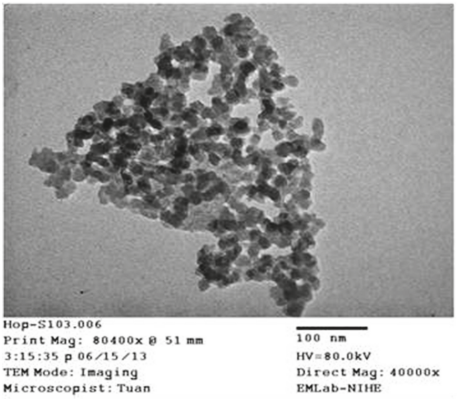

Figure 4. TEM of nanosilica.

Table 2 lists the main curing characteristics of the fabricated NR compounds that were obtained from the cure curves (Figure 5), in which both t_2 and t_{90} increased with increasing silica nanoparticle content in the NR. In general, the minimum torque (M_L) in Figure 5 is associated with a shear viscosity of the blend, while the maximum torque (M_H) has a relation to the elastic stiffness of vulcanized samples. The results implied that with addition of nanosilica, both M_L and M_H values increased, meaning that the viscosity or stiffness of vulcanized NR increased with the presence of nanosilica particles. The difference between maximum torque and minimum torque, (M_H-M_L), which was obtained from the dynamic shear modulus test, corresponds indirectly to the crosslinking density of the vulcanization. The results indicated that the (M_H-M_L) exhibited the same tendency to the maximum torque and increased with increasing nanosilica loading as a result of increased cross-linking of the NR with the presence of nanosilica particles.

Figure 6 presents typical stress-strain curves of the nanosilica-reinforced NR composite materials. All samples exhibited the deformation-forced crystallization characteristics with the rapidly raised sharp slopes when the strain reached more than 1500% [36,43,44]. Meanwhile, the tensile stress and slope curves increased with increased contents of silica and reached the optimal properties at 3 phr of silica filled NR. The details of the mechanical characteristics are provided in Table 3.

Table 2. Curing properties of the silica/rubber compounds.

Samples	Curing Properties				
	Minimum Torque, M_L (dN·m)	**Maximum Torque, M_H (dN·m)**	**$\triangle M = M_H - M_L$ (dN·m)**	**Scorch Time, t_{s2} (min:s)**	**Cure Time, t_{90} (min:s)**
M0	0.135	6.000	5.865	4:11	15:89
M1	0.144	6.400	6.256	4:25	16:15
M2	0.148	6.600	6.452	4:39	16:41
M3	0.154	6.850	6.696	4:41	16:83
M4	0.169	7.535	7.366	4:54	16:92
M5	0.185	8.220	8.035	4:60	17:01

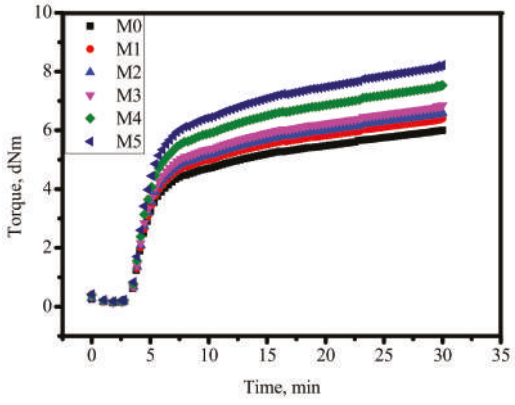

Figure 5. Cure curves of the investigated rubber compounds taken at 150 °C (black line—M0; red line—M1; blue line—M2; pink line—M3; olive line—M4; green line—M5).

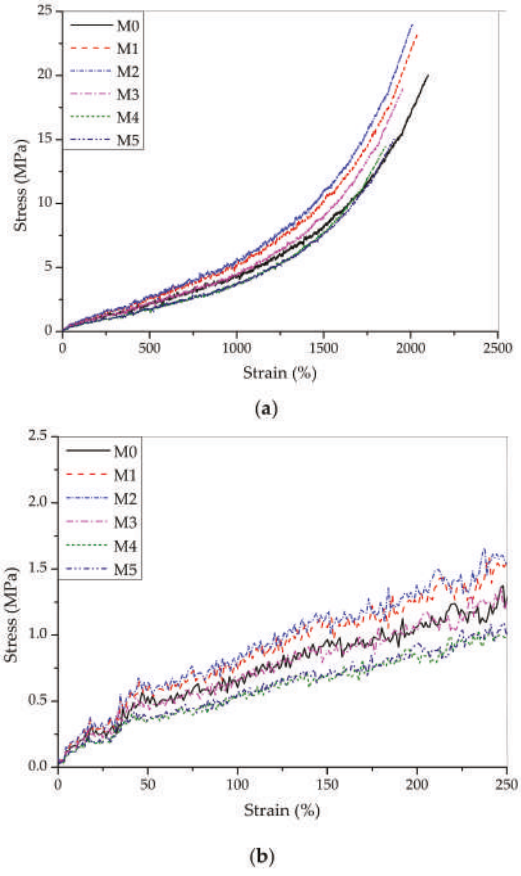

Figure 6. (**a**) Typical stress-strain of cured samples (Black line—M0; red line–M1; blue line—M2; pink line—M3; olive line—M4; orange line—M5). (**b**) The bottom figure is the one expanded in the initial stage;

Table 3. Mechanical properties of cured NR/silica compounds.

Samples	Mechanical Properties		
	Tensile Strength (MPa)	Elongation at Break (%)	Hardness (Shore A)
M0	20.02	2100.12	38.51
M1	23.18	2036.85	39.72
M2	24.15	2014.52	41.24
M3	18.93	1953.77	42.51
M4	15.13	1909.49	43.22
M5	14.45	1855.26	45.06

The tensile strength exhibited the decreasing trend when the silica content exceeded 3 phr. Although the elongation at break decreased with increased silica concentration, the hardness of the NR showed the same trend with the tensile strength. Both changes in the tensile strength and elongation at break for different nanosilica loadings have a relationship with a cross-linking density of the cured NR composites. That of the NR increased with silica concentration, resulting in an increase of the tensile strength and a decrease of the elongation at break due to the decreased slippage among the molecular chains. The H-bond between silica particles and rubber chain prevented the mobility and slippage of the rubber chain. On the other hand, the fact that tensile strength only increased with silica contents up to 3 phr may be due to the agglomeration of nanosilica at a higher content. The crosslinking densities of samples with name M0, M1, M2, M3, M4, M5 were 7.82×10^5, 8.06×10^5, 8.19×10^5, 8.22×10^5, 8.36×10^5 and 8.45×10^5 mol/cm^3, respectively. The trend of crosslinking density is the same as with the trend of M_H and hardness. The hardness also increased with increased silica content. The incremental increase of crosslinking density resulted in the decreasing of elongation at break because of the prevention of the slip between each NR molecule. In addition, more energy was needed to break the linkage between each rubber molecule as the result of increased tensile strength.

The SEM image results of the tensile fractured surface of the NR composites both in the absence and presence of 3 phr of nanosilica were presented in Figure 7. These results indicated that the fractured surface of the 3 phr silica-filled NR was observed to be rougher in comparison with the pristine sample. Therefore, extra energy was required compared to the case of the smooth fractured surface of the pristine NR. This result is in agreement with the tensile results shown in Figure 6.

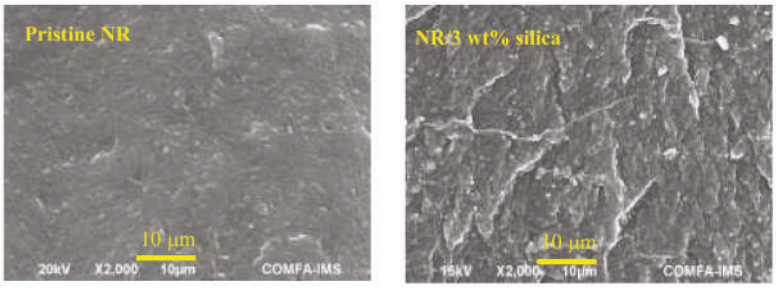

Figure 7. SEM images of the fracture surface of pristine natural rubber and 3 phr silica filled natural rubber.

The TEM images of both the natural rubber and 3 phr silica filled natural rubber are shown in Figure 8. The pristine NR sample had no silica particles, while the silica particles existed in the modified NR with nano scale from 20–60 nm.

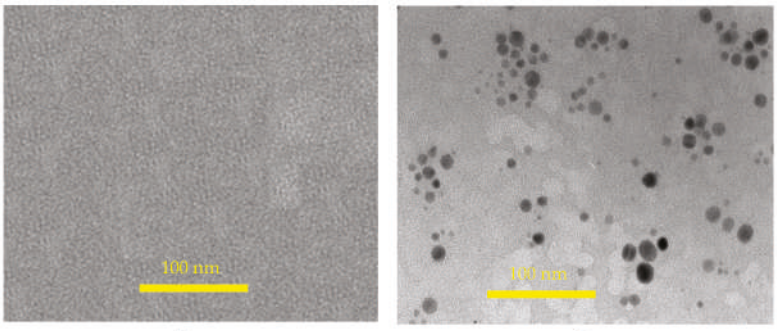

Figure 8. TEM images of pristine natural rubber (**a**) and 3 phr silica filled natural rubber (**b**).

The thermal degradation of both the pristine NR and the 3 phr nanosilica filled NR composites was examined in terms of the weight loss (%) as a function of temperature, as shown in Figure 9.

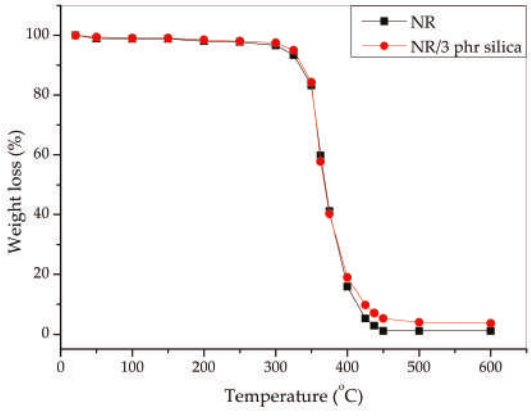

Figure 9. TGA of cured natural rubber (NR) (black dot line) and 3 phr of nanosilica filled natural rubber (red dot line).

Thermal degradation of the NR can be explained via various processes such as chain-scission of the polymers, and breakage of the cross-linked portion. The silica filled NR composite exhibited a 2.5% higher decomposition temperature in comparison with the pristine NR because of the existence of H-bonds between silica particles and rubber chains with higher thermal stability. The thermal degradation of both pristine and silica filled NR occurs through the degradation of isoprene units at around 368 °C. The presence of nanosilica induced the higher residues of nanocomposite when compared with pristine NR due to the presence of inorganic filler, which is more thermally stable than NR. The TGA results demonstrate that the nanosilica filled NR showed only a very slightly higher thermal stability than that for the NR. The initial temperature decomposition, the maximum decomposition temperature, and residue of silica modified NR and pure NR were 268.2 °C, 368.2 °C, 1.1% and 266.8 °C, 366.3 °C, 3.7%, respectively. The entire thermal degradation of the nanocomposite can be explained by the two-step process. First of all, the rubber chains and cross-linking were deteriorated into smaller parts. In the second step, the smaller parts in the first step continuously degraded into volatile products and disappeared. The residual char was higher for the nanosilica-filled sample.

Figure 10 shows the XRD patterns of vulcanized pure NR and NR/3 phr silica nanocomposite. The broad diffraction peak around 20° is the noncrystalline structure of NR, while the diffraction peaks

between 30°–50° are assigned to ZnO particles in the vulcanizates. None of the samples show obvious characteristic peaks of graphite or silica, indicating that silica particles are homogeneously dispersed in the rubber matrix. These results indicated that the silica did not keep the amorphous structure when embedded in natural rubber.

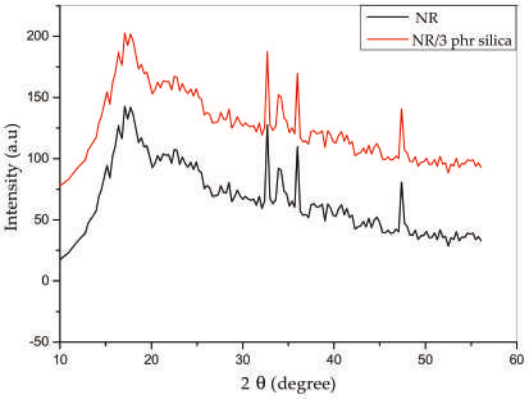

Figure 10. XRD spectra of vulcanized NR and NR/3 phr silica.

4. Conclusions

In this study, amorphous silica nanoparticles (between the sizes of 40–60 nm) were extracted from hexafluorosilicic acid waste produced by the Vietnamese fertilizer industry via a precipitation process. The production and utilization of the nanosilica by-product could become a reliable and sustainable solution for dealing with waste water from fertilizer plants environmentally as well as economically, regarding the waste water treatment. The resulting silica nanoparticles were then adopted as the filler for NR. The tensile strength of 3 phr silica-added NR nanocomposites increased by 20.6% compared to that of pristine NR. The elongation at break decreased with increased filler content and the hardness of the filled sample increased with increasing nanosilica content. The filled sample also exhibited better thermal resistance than the pristine sample due to the presence of nanosilica.

Author Contributions: Data curation, C.M.V., B.X.K.; formal analysis, C.M.V.; investigation, V.-H.N.; validation, H.J.C.; writing—original draft, C.M.V.; writing—review and editing, H.J.C.

Funding: This work was funded by Vietnam National Foundation for Science and Technology Development (grant number: 104.02-2017.15). One of the authors (H.J.C.) was partially supported by National Research Foundation of Korea (2018R1A4A1025169).

Conflicts of Interest: The authors declare no conflict of interest.

References

1. Chandra, C.S.J.; Bipinbal, P.K.; Sunil, K.N. Viscoelastic behaviour of silica filled natural rubber composites—Correlation of shear with elongational testing. *Polym. Test.* **2017**, *60*, 187–197. [CrossRef]
2. Tchalla, S.T.; Gac, P.Y.L.; Maurin, R.; Creachcade, R. Polychloroprene behaviour in a marine environment: Role of silica fillers. *Polym. Degrad. Stab.* **2017**, *139*, 28–37. [CrossRef]
3. Xu, T.; Jia, Z.; Wu, L.; Chen, Y.; Luo, Y.; Jia, D.; Peng, Z. Influence of acetone extract from natural rubber on the structure and interface interaction in NR/silica composites. *Appl. Surf. Sci.* **2017**, *423*, 43–52. [CrossRef]
4. Zhang, C.; Tang, Z.; Guo, B.; Zhang, L. Significantly improved rubber-silica interface via subtly controlling surface chemistry of silica. *Compos. Sci. Technol.* **2018**, *156*, 70–77. [CrossRef]
5. Jing, Y.; Niu, H.; Li, Y. Improved ethylene-propylene rubber/silica interface via in-situ polymerization. *Polymer* **2019**, *172*, 117–125. [CrossRef]
6. Jong, L. Improved mechanical properties of silica reinforced rubber with natural polymer. *Polym. Test.* **2019**, *79*, 106009. [CrossRef]

7. Tian, Q.; Tang, Y.; Ding, T.; Li, X.; Zhang, Z. Effect of nanosilica surface-capped by bis[3-(triethoxysilyl)propyl] tetrasulfide on the mechanical properties of styrene-butadiene rubber/butadiene rubber nanocomposites. *Compos. Commun.* **2018**, *10*, 190–193. [CrossRef]
8. Xu, H.; Xia, X.; Hussain, M.; Song, Y.; Zheng, Q. Linear and nonlinear rheological behaviors of silica filled nitrile butadiene rubber. *Polymer* **2018**, *156*, 222–227. [CrossRef]
9. Liu, D.; Song, L.; Song, H.; Chen, J.; Tian, Q.; Chen, L.; Sun, L.; Lu, A.; Huang, C.; Sun, G. Correlation between mechanical properties and microscopic structures of an optimized silica fraction in silicone rubber. *Compos. Sci. Technol.* **2018**, *165*, 373–379. [CrossRef]
10. Dong, B.; Liu, C.; Wu, Y.P. Fracture and fatigue of silica/carbon black/natural rubber composites. *Polym. Test.* **2014**, *38*, 40–45. [CrossRef]
11. Spratte, T.; Plagge, J.; Wunde, M.; Klüppel, M. Investigation of strain-induced crystallization of carbon black and silica filled natural rubber composites based on mechanical and temperature measurements. *Polymer* **2017**, *115*, 12–20. [CrossRef]
12. Cheng, Y.Z.; Zeng, X.; Cheng, D.B.; Xu, X.D.; Zhang, X.Z.; Zhuo, R.X.; He, F. Functional mesoporous silica nanoparticles (MSNs) for highly controllable drug release and synergistic therapy. *Colloids Surf. B Biointerfaces* **2016**, *145*, 217–225. [CrossRef]
13. Geng, H.; Zhao, Y.; Liu, J.; Cui, Y.; Wang, Y.; Zhao, Q.; Wang, S. Hollow mesoporous silica as a high drug loading carrier for regulation insoluble drug release. *Int. J. Pharm.* **2016**, *510*, 184–194. [CrossRef]
14. Jiao, J.; Li, X.; Zhang, S.; Liu, J.; Di, D.; Zhang, Y.; Zhao, Q.; Wang, S. Redox and pH dual-responsive PEG and chitosan-conjugated hollow mesoporous silica for controlled drug release. *Mater. Sci. Eng. C* **2016**, *67*, 26–33. [CrossRef]
15. Anbarasu, G.; Malathy, M.; Karthikeyan, P.; Rajavel, R. Silica functionalized Cu(II) acetylacetonate Schiff base complex: An efficient catalyst for the oxidative condensation reaction of benzyl alcohol with amines. *J. Solid State Chem.* **2017**, *253*, 305–312. [CrossRef]
16. Leckie, L.; Mapolie, S.F. Mesoporous silica as phase transfer agent in the biphasic oxidative cleavage of alkenes using triazole complexes of ruthenium as catalyst precursors. *Appl. Catal. A Gen.* **2018**, *565*, 76–86. [CrossRef]
17. Shabbir, S.; Lee, S.; Lim, M.; Lee, H.; Ko, H.; Lee, Y.; Rhee, H. Pd nanoparticles on reverse phase silica gel as recyclable catalyst for Suzuki-Miyaura cross coupling reaction and hydrogenation in water. *J. Organomet. Chem.* **2017**, *846*, 296–304. [CrossRef]
18. Zeng, K.; Huang, Z.; Yang, J.; Gu, Y. Silica-supported policresulen as a solid acid catalyst for organic reactions. *Chin. J. Catal.* **2015**, *36*, 1606–1613. [CrossRef]
19. Abou, R.M.; Faouzi, H. Synthesis and charaterization of amorphous silica nanoparticles from aqueous silicates using cationic Surfactants. *J. Met. Mater. Miner.* **2014**, *24*, 37–42.
20. Elineema, G.; Kim, J.K.; Hilonga, A.; Shao, G.N.; Kim, Y.N.; Quang, D.V.; Sarawade, P.B.; Kim, H.T. Quantitative recovery of high purity nanoporous silica from waste products of the phosphate fertilizer industry. *J. Ind. Eng. Chem.* **2013**, *19*, 63–67. [CrossRef]
21. Gustafsson, H.; Holmberg, K. Emulsion-based synthesis of porous silica. *Adv. Colloid Interface Sci.* **2017**, *247*, 426–434. [CrossRef]
22. Kang, K.K.; Oh, H.S.; Kim, D.Y.; Shim, G.; Lee, C.S. Synthesis of Silica Nanoparticles Using Biomimetic Mineralization with Polyallylamine Hydrochloride. *J. Colloid Interface Sci.* **2017**, *507*, 145–153. [CrossRef]
23. Kerdlap, W.; Thongpitak, C.; Keawmaungkom, S.; Warakulwit, C.; Klangprapan, S.; Choowongkomon, K.; Chisti, Y.; Hansupalak, N. Natural rubber as a template for making hollow silica spheres and their use as antibacterial agents. *Micropor. Mesopor. Mater.* **2019**, *273*, 10–18. [CrossRef]
24. Zulfiqar, U.; Subhani, T.; Husain, S.W. Synthesis and characterization of silica nanoparticles from clay. *J. Asian Ceramic Soc.* **2016**, *4*, 91–96. [CrossRef]
25. Sarawade, P.B.; Kim, J.K.; Hilonga, A.; Kim, H.T. Recovery of high surface area mesoporous silica from waste hexafluorosilicic acid (H_2SiF_6) of fertilizer industry. *J. Hazard. Mater.* **2010**, *173*, 576–580. [CrossRef]
26. Satisk, K.W. Amorphous Precipitated Siliceous Pigment for Cosmetic or Dentifrice Use and Method for Their Production. USA Patent 3,928,541, 23 December 1975.
27. Ui, S.W.; Lim, S.J.; Sang, H.L.; Choi, S.C. Control of size and morphology of nanosize silica particles using a sodium silicate solution. *J. Ceram. Process. Res.* **2009**, *10*, 553–558.

28. Patel, B.H.; Patel, P.N. Synthesis and charaterization of silica nano particles by acid leaching technique. *Res. J. Chem. Sci.* **2014**, *4*, 52–55.
29. Jin, F.; Wang, X.; Liu, T.; Wu, Y.; Xiao, L.; Yuan, M.; Fan, Y. Synthesis of ZSM-5 with the Silica Source from Industrial Hexafluorosilicic Acid as Transalkylation Catalyst. *Chin. J. Chem. Eng.* **2016**, *25*, 1303–1313. [CrossRef]
30. Krysztafkiewicz, A.; Rager, B.; Maik, M. Silica recovery from waste obtained in hydrofluoric acid and aluminum fluoride production from fluosilicic acid. *J. Hazard. Mater.* **1996**, *48*, 31–49. [CrossRef]
31. Jeong, S.Y.; Suh, J.K.; Lee, J.M.; Kwon, O.Y. Preparation of silica-based mesoporous materials from fluorosilicon compounds: Gelation of H2SiF6 in ammonia surfactant solution. *J. Colloid Interface Sci.* **1997**, *192*, 156–161. [CrossRef]
32. Panasyuk, G.P.; Azarova, L.A.; Privalov, V.L.; Belan, V.N.; Voroshilov, I.G.; Shpigun, L.K. Preparation of Silicon Dioxide with a Fixed Content of Fluorine from Fluorosilicic Acid. *Theor. Found. Chem. Eng.* **2018**, *52*, 607–611. [CrossRef]
33. Sikdar, S.K.; Moore, J.H. Recovery of Hydrofluoric Acid from Fluosilicic Acid with High pH Hydrolysis. USA Patent 4,213,951, 22 July 1980.
34. Sikdar, S.K.; Moore, J.H. Process for Producing Fluorine Compounds and Amorphous Silica. USA Patent 4,308,244, 29 December 1981.
35. Spijker, R. Process for the Preparation of Pure Silicon Dioxide. *Eur. Patent* **1983**, *94*, 139.
36. Toki, S.; Hsiao, B.S. Nature of Strain-Induced Structures in Natural and Synthetic Rubbers under Stretching. *Macromolecules* **2003**, *36*, 5915–5917. [CrossRef]
37. Zorya, L.; Krot, V. Method of high-purity silica production from hexafluorosilicic acid. *React. Kinet. Catal. Lett.* **1993**, *50*, 349–354. [CrossRef]
38. Dragicevic, T.; Hraste, M. Surface area of silica produced by neutralization of fluosilicic acid. *Chem. Biochem. Eng.* **1994**, *8*, 141–143.
39. Cicala, G.; Bruno, G.; Capezzuto, P. Plasma deposition of amorphous silicon alloys from fluorinated gases. *Pure Appl. Chem.* **1996**, *5*, 1143–1149. [CrossRef]
40. Guzeev, V.V.; D'yachenko, A.N.; Grishkov, V.N. Integrated utilization of silicon tetrafluoride and zirconium dioxide. *Russ. J. Appl. Chem.* **2003**, *76*, 1952–1955. [CrossRef]
41. Liu, T.; Jin, F.; Wang, X.; Fan, Y.; Yuan, M. Synthesis of titanium containing MCM-41 from industrial hexafluorosilicic acid as epoxidation catalyst. *Catal. Today* **2017**, *297*, 316–323. [CrossRef]
42. Vu, C.M.; Vu, H.T.; Choi, H.J. Fabrication of Natural Rubber/Epoxidized Natural Rubber/Nanosilica Nanocomposites and Their Physical Characteristics. *Macromol. Res.* **2015**, *23*, 284–290. [CrossRef]
43. Chen, L.; Guo, X.; Luo, Y.; Jia, Z.; Bai, J.; Chen, Y.; Jia, D. Effect of novel supported vulcanizing agent on the interfacial interaction and strain-induced crystallization properties of natural rubber nanocomposites. *Polymer* **2018**, *148*, 390–399. [CrossRef]
44. Chenal, J.M.; Chazeau, L.; Guy, L.; Bomal, Y.; Gauthier, C. Molecular weight between physical entanglements in natural rubber: A critical parameter during strain-induced crystallization. *Polymer* **2007**, *48*, 1042–1046. [CrossRef]

materials

MDPI

Article

Micron-Size White Bamboo Fibril-Based Silane Cellulose Aerogel: Fabrication and Oil Absorbent Characteristics

Dinh Duc Nguyen [1,2], Cuong Manh Vu [3,4,*], Huong Thi Vu [5] and Hyoung Jin Choi [6,*]

1 Department for Management of Science and Technology Development, Ton Duc Thang University, Ho Chi Minh City 700000, Vietnam; nguyendinhduc@tdtu.edu.vn
2 Faculty of Environment and Labour Safety, Ton Duc Thang University, Ho Chi Minh City 700000, Vietnam
3 Center for Advanced Chemistry, Institute of Research and Development, Duy Tan University, Da Nang 550000, Vietnam
4 Faculty of Chemical-Physical Engineering, Le Qui Don Technical University, 236 Hoang Quoc Viet, Ha Noi 100000, Vietnam
5 AQP research and control pharmaceuticals Joint Stock Company (AQP Pharma J.S.C) Dong Da, Ha Noi 100000, Vietnam; huongvtaqp@gmail.com
6 Department of Polymer Science and Engineering, Inha University, Incheon 22212, Korea
* Correspondence: vumanhcuong309@gmail.com (C.M.V.); hjchoi@inha.ac.kr (H.J.C.)

Received: 29 March 2019; Accepted: 25 April 2019; Published: 30 April 2019

Abstract: Micron-size white bamboo fibrils were fabricated from white bamboo and used as a source for the production of highly porous and very lightweight cellulose aerogels for use as a potential oil absorbent. The aerogels were fabricated through gelation from an aqueous alkali hydroxide/urea solution, followed by a conventional freeze-drying process. The morphology and physical properties of the aerogels were characterized by field emission scanning electron microscopy and Brunauer–Emmett–Teller surface area analysis, respectively. Successful silanization of the cellulose aerogel was confirmed by energy-dispersive X-ray spectroscopy, Fourier-transform infrared spectroscopy, and water contact angle measurements. The fabricated silane cellulose aerogel exhibited excellent absorption performance for various oil and organic solvents with typical weight gains ranging from 400% to 1200% of their own dry weight, making them promising versatile absorbents for a range of applications, including water purification.

Keywords: cellulose aerogel; oil absorbent; cellulose; white bamboo fibril; water pollution

1. Introduction

Water pollution caused by oil spillage related to the rapid development of the petroleum industries have serious effects on the environment and human life [1–3]. To resolve this problem, many methods have been proposed for water purification, such as water/oil separation [4–6], photocatalytic degradation [7,8], and adsorption [9–11]. Among these technologies, the use of porous absorbents with a hydrophobic surface is very promising for the rapid removal of oil from the surface of water. Various types of materials used as absorbents for cleaning oil spills have been fabricated. Oil absorbents can be sorted as inorganic minerals, synthetic organics, and natural organic materials [12]. Inorganic materials, such as fly ash and exfoliated graphite have low oil absorption capacity, whereas synthetic organic materials (i.e., polypropylene and polyurethane) possess high affinity to oil and organic solvents but cause a waste problem after their use due to their very slow degradation. Natural organic materials for oil absorption from plants (cellulose fibers) and animal residues (chitin and chitosan) have attracted increasing attention because of their renewability, low-cost, and biodegradability [13]. In addition, many kinds of natural materials, such as kapok fiber [14,15],

cotton fiber [16], wool fiber [17], milkweed [18], and sawdust [19], have been exploited for the simple, effective, and inexpensive treatments of oil spills. However, most of these are hydrophilic, resulting in low oil sorption capacity. Therefore, there is still a need to find new environmental friendly absorbents with high oil absorption capacity, good selectivity, and low-cost.

Aerogels are a highly porous solid that hold up to 99% by volume of air within their pores and are known as the lowest density solid material [20]. These materials have become the most promising absorbents owing to their lightness, high porosity, and large inner surface area. Aerogels can be obtained from both inorganic sources, such as silica [21–23] and metal oxides [24], and organic sources [25–27]. Generally, the mechanism of oil sorption by aerogels is considered to be governed mainly by aerogel surface adsorption, absorption, and diffusion through the voids via interfiber capillary action [28–30], and the amount adsorbed is known to be dependent on surface area and porosity of adsorbents [31].

Concurrently, as an abundant, sustainable, renewable, and biodegradable resource of biopolymer, various cellulose-based aerogels have been investigated [32–37]. However, because the untreated cellulose aerogels have high hydrophilicity, they can absorb both oil and water during the absorption processing [36]. Therefore, the surface modification is needed to improve the hydrophobicity and absorption efficiency. The silanization processing also became one of the best ways for this aim [35,36]. Cellulose can be obtained from plants, such as bamboo. In Vietnam, bamboo is distributed widely in the north and is mainly being used as a raw material for tradition products such as toothsticks, chopsticks, floors, and some furniture. To the best of the authors' knowledge, there are few reports of the fabrication of aerogels from white bamboo and their application as both an absorbent for oil and other toxic chemicals especially at the time when water pollution by oil and chemical spills is becoming a serious problem caused by the huge development of the petrochemical industry.

In this study, bamboo was used as a source of micron-size white bamboo fibrils prior to fabricating the aerogel. The aerogels were prepared in a simple way from the gels of micron-size white bamboo fibrils (MWBFs) in an aqueous alkali hydroxide/urea solution, followed by conventional freeze-drying. The resulting aerogel was rendered hydrophobic and oleophilic after being treated with a silane compound using a common chemical vapor deposition process.

2. Experiments

2.1. Materials and Chemicals

Dendrocalamus membranaceus Munro (white bamboo, ~3 years) from Hoa Binh Province, Vietnam was used as a micron-size fiber resource. Gama-methacryloxypropyltrimethoxysilane (MEMO silane) was purchased from Evonik Industries (Ho Chi Minh, Vietnam). All other chemicals, including alkali hydroxide, urea, and ethanol, were of reagent grade (Xilong Chemical Co. Ltd, Guangdong, China). All aqueous solutions were prepared using distilled water.

2.2. Preparation of Micron-Size White Bamboo Fibrils

The MWBF was fabricated from raw white bamboo using both a steam explosion following alkaline treatment technique and the mechanical extraction method (microgrinding). Raw white bamboo (~3 years old) was first cut into bamboo culms of 50–60 cm in length using a saw machine, and placed into an autoclave with over-heated steam at 175 °C and 0.7–0.8 MPa for 60 min. The steam was then released suddenly for 5 min and the cycles of sudden steam release were repeated 9 times. Subsequently, samples were immersed in a 2% NaOH solution at 70 °C for 5 h to ensure the complete removal of the cell walls. The roller looser was then used to extract the slabs into small fibers. Finally, they were washed with fresh water until they were neutralized, and dried in an oven for 24 h at 105 °C. The resulting fibers were dispersed in water with a fiber content of 10 wt.%. They were then cut into pulp fibers using a food mixer. The pulp fibers were passed 15 times between static grind and rotating grind stones revolving at 1500 rpm (MKCA6-3, Masuko Sangyo Co. Ltd., Saitama, Japan).

The obtained MWBF (water slurry with 90% water) was treated with ethanol to remove the water and filtered using a vacuum pump to obtain a sheet of MWBF. The filtered sheet of MWBF was stirred with an additional amount of ethanol using a stirrer at 5000 rpm for 15 min. The morphology of the MWBF was examined by scanning electron microscopy (SEM) (JEOL, Tokyo, Japan), as shown in Figure 1. The SEM in Figure 1 indicates that the diameter of cellulose fiber is in range from 90 nm to 0.2 μm, but its length is in the order of tens of micron.

(A) (B) (C)

Figure 1. Picture of white bamboo (**A**), micron-size white bamboo fibrils (MWBFs) (**B**), and SEM image of MWBFs (**C**).

2.3. Preparation of Cellulose Aerogel

The solvent mixture of NaOH/urea/H_2O (7:12:81 w/w) was precooled to approximately 5 °C. The desired amount of MWBF samples (1.5, 2, and 2.5 wt.%) was then dispersed immediately into the solvent system under vigorous stirring at this low temperature until a semitransparent or transparent gel was achieved, depending on the MWBF concentration. At the final stage, the gel was vacuumed to remove the air bubbles. The specimen thickness was controlled to approximately 2 cm using a beaker as a mold and then immersed into ethanol to obtain the 5 wt.% solution. A 100 mL of aqueous 10 wt.% H_2SO_4 solution was then added at ambient temperature for coagulation. The resulting cellulose hydrogels were washed with excess distilled water to remove the residual chemical reagents. The sample was then frozen in a freezer at −80 °C for 24 h and freeze-dried using a FTS Systems Dura-Stop Digital Control Stoppering Tray Dryer to obtain the desired cellulose aerogel (CA).

2.4. Fabrication of Silane Treated Cellulose Aerogel

A thermal chemical vapor deposition technique was used for surface modification of the cellulose aerogel. A Petri dish containing MEMO silane was placed in a vacuum desiccator together with the aerogel samples. The desiccator was sealed and vacuumed to 0.01 MPa, and then heated in an oven at 110 °C for various periods of time to determine the optimal conditions for the silanization reaction. Subsequently, the silane-coated cellulose aerogel (SCA) sample was kept in a vacuum oven for 30 min to remove the excess unreacted silane and by-products.

2.5. Characterization

All the tests were carried out in triplicate and the average results are reported. Initially, the densities of the cellulose aerogels were calculated by measuring the mass and volume of the aerogels. The mass was measured using an analytical balance, Fisher Scientific Accu-225D, with accuracy of 0.1 mg. The volume was determined by measuring the dimensions using a digital Vernier caliper. Average density was estimated after 5 measurements for 3 different aerogels [26]. The porosity was calculated using Equation (1):

$$\text{Porosity } (\%) = \left(1 - \frac{\rho_a}{\rho_c}\right) \times 100 \quad (1)$$

where ρ_a is the density of the aerogel and ρ_c is the density of MWBF (1.59 g/cm^3).

The BET specific surface area was determined by a N_2 physisorption method using Gemini VII 2390 equipment (Micromeritic Instrument Co., Norcross, GA, USA). The wettability of the SCA was evaluated by measuring the water contact angle. Images of distilled droplets on the SCA surface were taken with a digital camera (Cannon 20D and Nikkon 105 mm 1:2.5 lens, Bangkok, Thailand) and imported into the measurement software. The volume of the droplet was fixed using a 5-mL cylinder. The software is licensed image processing and analysis in Java (ImageJ) [38] and included low-bond axisymmetric drop shape analysis (LB-ADSA). The mean of the three measurements performed at different surface locations are reported as the water contact angle. The Fourier-transform infrared (FTIR) spectra of the cellulose aerogel (CA) sample before and after silanization were recorded on IRAFFINITY-1S equipment (Shimadzu, Kyoto, Japan) at room temperature. The microstructure and elemental analysis of the uncoated and coated CA were examined by field-emission scanning electron microscopy (FE-SEM) (JEOL JSM-7600F, Tokyo, Japan) equipped with an energy-dispersive X-ray spectroscope. The sample was coated with a thin layer of platinum by sputtering.

To investigate its compressive properties, a cylinder sample with a diameter of 20 mm and a height of 13 mm was compressed to 80% of its original height by using a universal testing machine (Instron, 100 kN, Norwood, MA, USA) with a compressing speed of 10 mm. min^{-1}. Five samples were tested to calculate the average value.

2.6. Oil/Solvent Absorption Capacity Measurements

The absorption capacity of SCA for various oils and organic solvents was determined by dipping a piece of SCA directly into the liquid (oil or solvent) for a certain time. The wet sample was then removed from the liquid and weighed after the aerogel surface has been blotted with filter paper to remove the excess surface oil/solvent. The test was repeated several times until the absorption process reached equilibrium. The absorption capacity (Q) was calculated from the mass gain using

$$Q\ (\%) = \frac{W - W_0}{W_0} \times 100 \tag{2}$$

where W_0 and W are the weights of the SCA before and after absorption, respectively.

The pseudo-first-order model (Equation (3)) and pseudo-second-order model (Equation (4)) were used to evaluate the absorption kinetics, where k_1 (h^{-1}) and k_2 (g·g^{-1}·%$^{-1}$·h^{-1}) are the adsorption rate constants of the pseudo-first-order equation and the pseudo-second-order equation, respectively. In addition, both Q_m and Q_t are absorption capacities at equilibrium conditions and at time t, respectively.

$$\ln \frac{Q_m}{Q_m - Q_t} = k_1 t \tag{3}$$

$$\frac{t}{Q_t} = \frac{1}{Q_m} t + \frac{1}{k_2 Q_m^2} \tag{4}$$

To examine their reusability, the oil/organic swollen samples were squeezed by hand to remove the absorbed solvent. The weights of the aerogels before organic adsorption, after adsorption, and after squeeze for removal of organic were measured during each cycle. Five samples were tested for each experiment.

3. Results and Discussion

3.1. Cellulose Aerogel Characteristics

By altering the concentration of the MWBF dispersion from 1.5 to 2.5 wt.%, aerogels with different porosities were prepared using a freeze-drying method. Under freeze-drying conditions, a slight shrinkage was observed in these aerogels compared to their initial hydrogel dimensions.

The experiments showed that the dispersion with 2.5 wt.% MWBF had very high viscosity, making it difficult to remove the air bubbles, resulting in a poor physical property. Table 1 lists the physical properties of the obtained cellulose aerogel.

Table 1. Physical properties of cellulose aerogels.

Sample	Cellulose Content (%)	Coagulation Solution	Density (g/cm^3)	Porosity (%)	Surface Area (m^2/g)
Cellulose aerogel	1.5	Ethanol	0.085	94.46	–
		Sulfuric acid	0.116	92.42	13.419
	2	Ethanol	0.131	91.41	–
		Sulfuric acid	0.135	91.19	9.046
	2.5	Ethanol	0.144	90.58	8.155

As shown in Table 1, the densities of the cellulose aerogels ranged from 0.085 to 0.144 g/cm^3, and all cellulose aerogels exhibited very high porosity (>90%). On the other hand, the specific surface area exhibited the low values from 8.155 to 13.419 m^2/g. Actually, this is quite common for aerogels obtained through a freeze-drying process. The main point here is that the typical porosity of such system is on the macron-scale, and hence the resulting specific surface area value is modest. The similar trend was also reported by Wang et al. [39]. Figure 2 shows the microstructure of a cross-section of the cellulose aerogel at different magnifications. The cellulose aerogels possessed a highly open porous honeycomb-like structure with a pore size distribution varying over a wide range from several to tens of micrometers. In addition, a network of interconnected uniform cellulose fibers appeared on the surface of the pore wall.

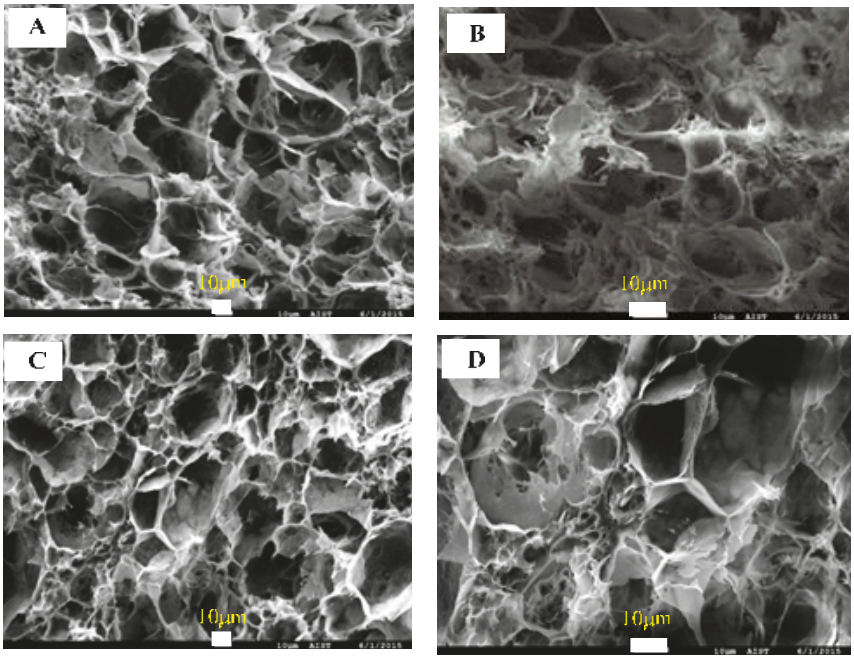

Figure 2. Field-emission scanning electron microscopy (FE-SEM) images of cellulose aerogel 2 wt.% (**a**,**b**) and cellulose aerogel 1.5 wt.% (**c**,**d**).

3.2. Mechanical Properties of Aerogel

The typical compression stress–strain curve of CA with different cellulose content is shown in Figure 3.

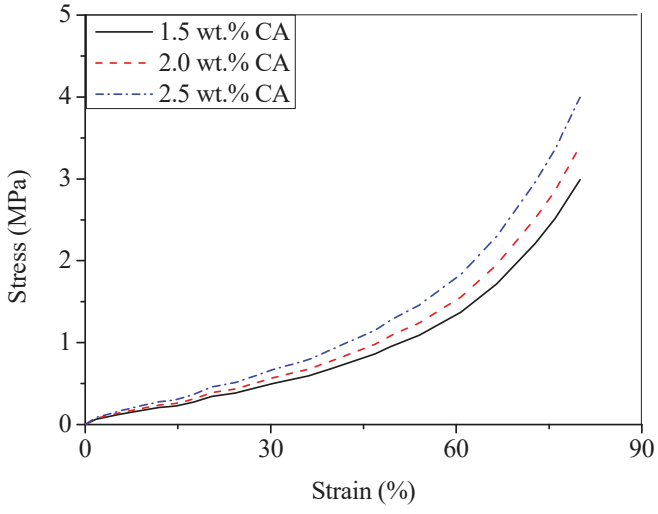

Figure 3. Typical compression stress–strain curves of cellulose aerogel (CA) with various cellulose concentration.

Figure 3 could be explained by two stress regions with increasing cellulose content. The first region appeared before 60% strain and can be characterized by slowly increasing stress, while the second region appeared at above 60% strain with rapidly increasing stress. The stress of CA obtained from 1.5, 2.0, and 2.5 wt.% of cellulose concentration at 60% strain was 1.37 ± 0.01; 1.55 ± 0.01, and 1.83 ± 0.02 MPa, respectively. At 80% strain, the stress of corresponding cellulose aerogels increased to 2.99 ± 0.02, 3.41 ± 0.01, and 4.01 ± 0.02 MPa, respectively. These results mean that the stress increased with increasing cellulose concentration as a result of higher crosslinking density. In addition, the slope of stress–strain curves was also increased with increasing cellulose content in the CA. The slope of stress–strain corresponded to the compressive modulus and the internal structure of aerogel. The high crosslinking density also was considered as a reason of increment of the compressive modulus above.

3.3. Silane Modification of Cellulose Aerogel

As hydrophilicity is the inherent nature of cellulose due to its hydroxyl groups, a silane coating was carried out for cellulose aerogels to make them both hydrophobic and oleophilic. To achieve this, a simple thermal chemical vapor deposition procedure was performed for the aerogel with MEMO silane at 110 °C in a vacuum desiccator, as described in the above. To become "active", the silane must first be hydrolyzed. The reaction of the silicon end of the molecule was initiated by the hydrolysis of the alkoxy group, usually after exposure to ambient moisture to form a silanol that releases alcohol as follows:

$$-\mathrm{Si(OCH_3)_3} + \mathrm{H_2O} \rightarrow -\mathrm{Si(OH)_3} + 3\,\mathrm{CH_3OH}$$

Once in the silanol state, the silane can be condensed on the aerogel surface, forming a direct covalent bond with the surface. The silanization process of the interior surface of as-prepared cellulose aerogel and silanized cellulose aerogel was shown in Figure 4.

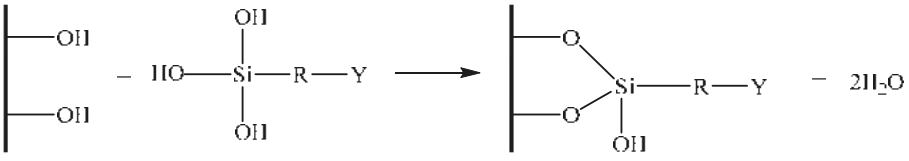

Figure 4. Silanization processing.

As shown in Figure 5, the open porous microstructure of the cellulose aerogel was preserved after coating. In addition, there was no change in the surface of the cellulose aerogel after coating, which might be due to the very thin silane coating layer.

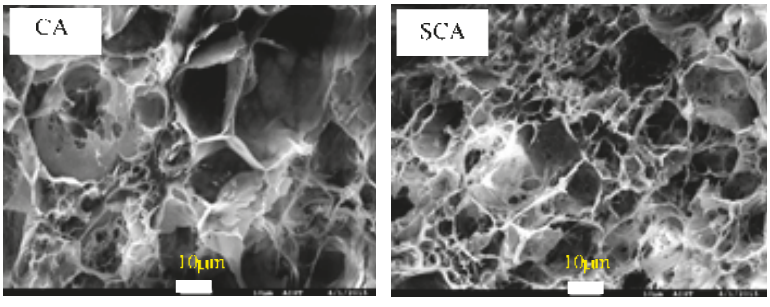

Figure 5. FE-SEM images of cross-section of CA and silane-coated cellulose aerogel (SCA).

Successful silanization on the surface of the cellulose aerogel was confirmed by FTIR spectroscopy, as shown in Figure 6. The FTIR spectrum of SCA showed four new peaks compared to the spectrum of the uncoated aerogel. The absorption bands at ~731 cm^{-1} and ~1269 cm^{-1} were attributed to the stretching and bending vibrations of the C–Si linkage, respectively. This confirmed the condensation of silane on the CA surface. In addition, the peak at 1720 cm^{-1} on the SCA spectrum was assigned to the characteristic vibrations of the carbonyl group of MEMO silane attached to the aerogel surface. The absorption band at ~815 cm^{-1} was attributed to the vibration of the Si-O-Si linkage, which might have formed due to the self-condensation of the silanols.

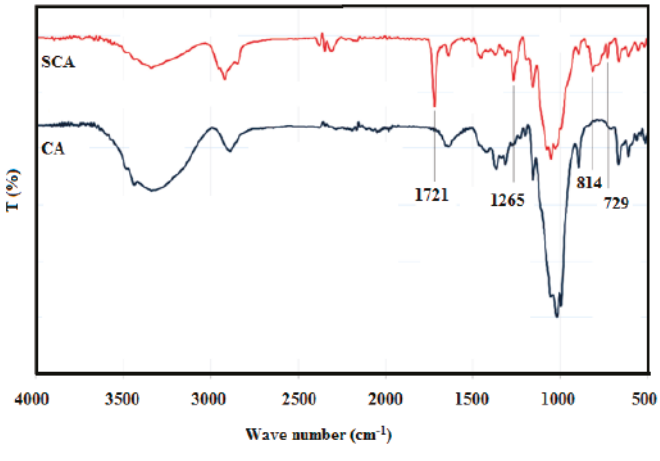

Figure 6. FTIR spectrums of cellulose aerogel and cellulose aerogel (CA) silanization with MEMO silane (SCA).

Silanization was confirmed by energy dispersive X-ray spectroscopy (EDX). The EDX spectrum of the uncoated CA revealed carbon and oxygen peaks but no silicon peak. After silanization, EDX showed peaks for carbon, oxygen, and silicon, as shown in Figure 7.

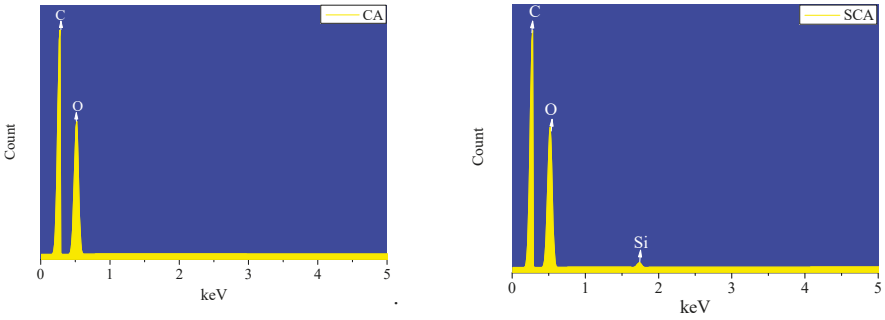

Figure 7. Energy dispersive X-ray spectroscopy (EDX) spectrum of (**a**) cellulose aerogel (CA) and (**b**) cellulose aerogel silanization with MEMO silane (SCA).

3.4. Surface Wettability of Silane-coated cellulose aerogel

Water contact angle measurements were also carried out on the uncoated and coated aerogel to study their surface wettability. The uncoated CA sample absorbed the distilled water droplet immediately in the test so no measurable contact angle was recorded. In contrast, high contact angles are observed for the MEMO silane-coated aerogel, as shown in Figure 8, proving the hydrophobicity of the material.

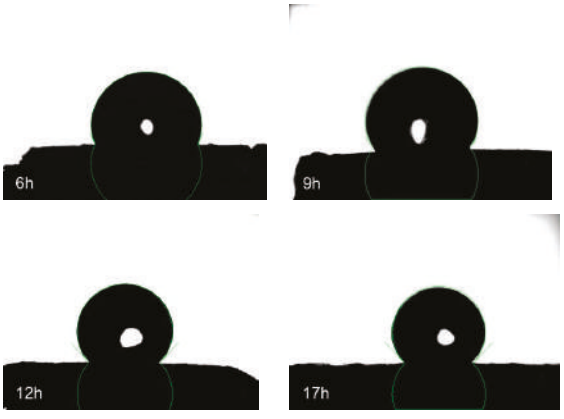

Figure 8. Measurements of water contact angle of cellulose aerogels after different coating processes.

Table 2 shows the improvement of the water contact angle of cellulose aerogels from 114.1 ± 5.26° to 132.3 ± 4.68° when the silanization time was increased from 6 to 12 h, indicating the high hydrophobicity of the obtained SCA. No increase in water contact angle was observed with further extended reaction times.

Table 2. Change of coated cellulose aerogel's water contact angle with silianation time.

Silanization Time (h)	Contact Angle (°)
6	114.1 ± 5.26
9	125.5 ± 4.68
12	132.3 ± 6.92
17	131.8 ± 5.18

3.5. Oil/Solvent Absorption Capacity of SCA and Its Recycleability

Owing to their low density, high porosity, and surface hydrophobicity, the silane-treated cellulose aerogels may be an ideal candidate for the selective absorption of oils and organic solvents from water. To examine the oil/solvent absorption behavior of MEMO silane-coated cellulose aerogel, several oils and organic solvents, such as toluene and gasoline were used.

Figure 9 shows the first minutes of the waste motor oil sorption process. The material absorbed the motor oil easily while floating in water, indicating high capacity absorption of the aerogel. After 5 min, there was no trace of waste motor oil on the water, showing that the sorption was completed successfully. Figure 10 shows the sorption kinetics of the oils and solvents on the silane-coated cellulose aerogel. The absorption rates were quite high at the very first stage and saturation was achieved after 75 h for all types of oils and solvents.

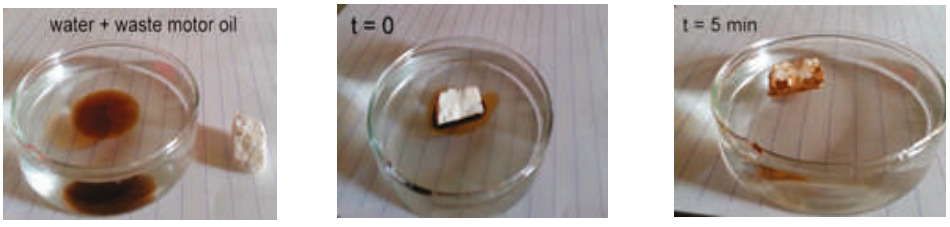

Figure 9. Waste motor oil absorption test of the silanized cellulose aerogel with MEMO silane.

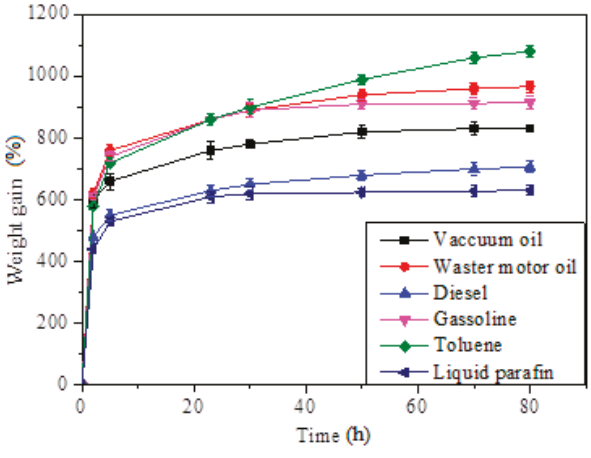

Figure 10. Absorption kinetics of oils and organic solvents on the silane-coated cellulose aerogel.

The experiment showed the linear relationship for both $\ln(Q_m/(Q_m - Q_t))$ and t/Q_t versus absorption time, t, for two representative adsorbates: vacuum oil and waste motor oil as shown in Figure 11. These results mean that the adsorption kinetics of the SCA followed the pseudo-first-order and pseudo-first-order equation quite similarly.

Equations (3) and (4) were used to calculate the absorption rate constants k_1, k_2, and correlation coefficient R^2 from Figure 11 as seen in Table 3.

The results in Table 3 indicated that the R^2 value of the pseudo second-order model of vacuum oil is higher than that of the pseudo first-order model. While the R^2 value of the pseudo second-order model of waste motor oil is lower than that of the pseudo first-order model. These results mean that the pseudo second order model can predict better the oil absorption behavior for vacuum oil and the pseudo first order model is better for waste motor oil in this work. The absorption processing of vacuum oil is faster than the absorption of waster motor oil because the k_1 and k_2 values of vacuum oil is higher than those of waste motor oil.

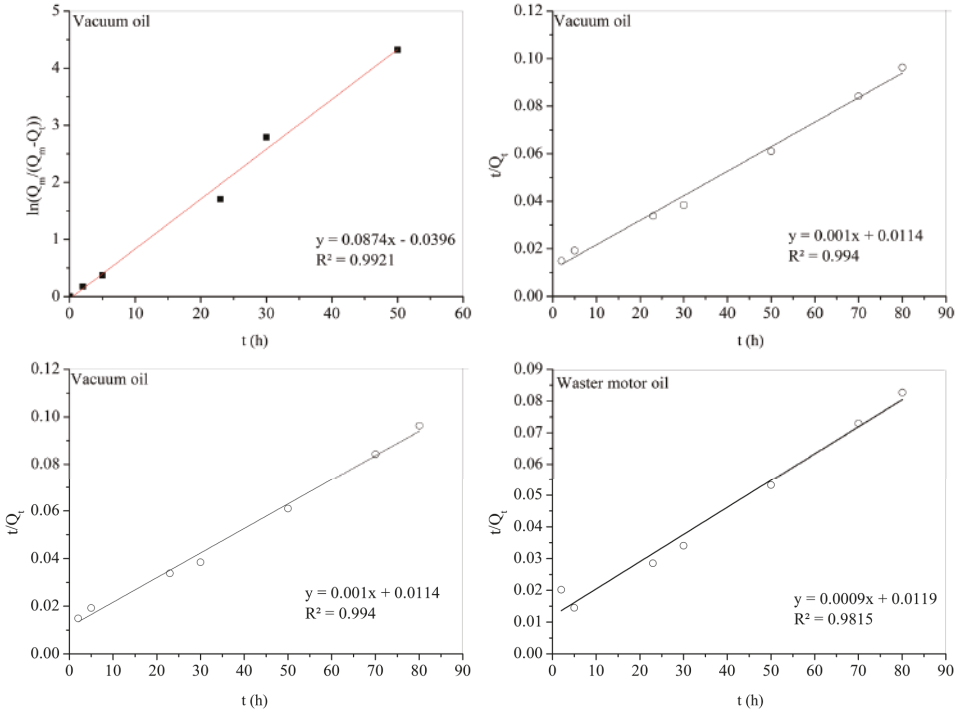

Figure 11. Pseudo-first-order and pseudo-second-order absorption linear fitting of the vacuum oil and waste motor oil onto SCA.

Table 3. Summary of the maximum oil absorption capacities and the absorption rate constants of the SCA using the pseudo-first-order and pseudo-second-order models.

Adsorbate	Maximum Absorption Capacity	Pseudo-First-Order		Pseudo-Second-Order	
	Q_m (%)	k_1	R^2	k_2	R^2
Vacuum oil	831 ± 12.2	0.0874	0.9921	1.27×10^{-5}	0.994
Waste motor oil	968 ± 18.6	0.0707	0.9956	8.99×10^{-5}	0.9815

Figure 12 shows the maximum absorption capacities of the oils and organic solvents on the silane-coated cellulose aerogel. The results showed that the absorbent had sorption capacity ranging from 631 ± 15.9% to 1081 ± 20.1% by weight gain. The high oil/solvent absorption capability of the silane-coated cellulose aerogel can be attributed to its highly porous structure and hydrophobic silane coating.

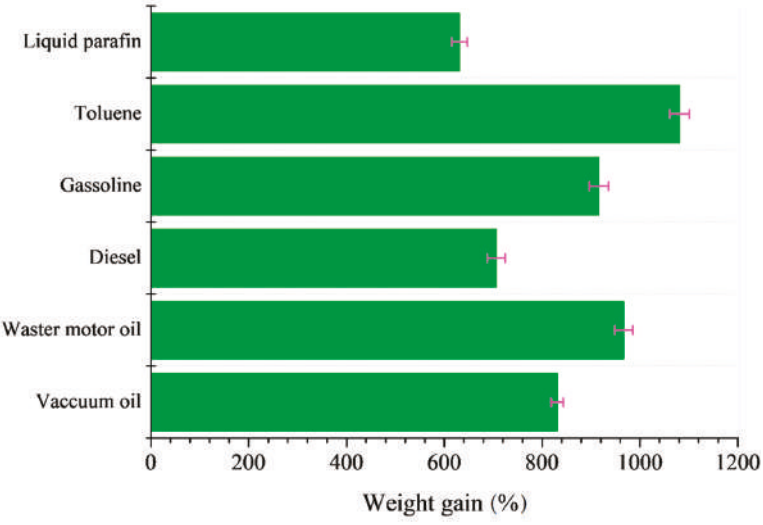

Figure 12. Absorption capacities of silane-coated cellulose aerogel for various oils and organic solvents as indicated by weight gain.

Because the weight gain of aerogel is related to the density of the respective oils and organic solvents, it can be normalized by dividing the oils and organic weight gain by the density of each respective oil and organic solvent. The results are reported in Figure 13. As shown in Figure 13, the highest absorption capacity was found for toluene and gasoline probably because these organic solvents possess the lowest viscosity. A lower viscosity would facilitate the penetration of solvent into the porous network of the aerogel more easily, leading to a higher oil/solvent absorption capacity.

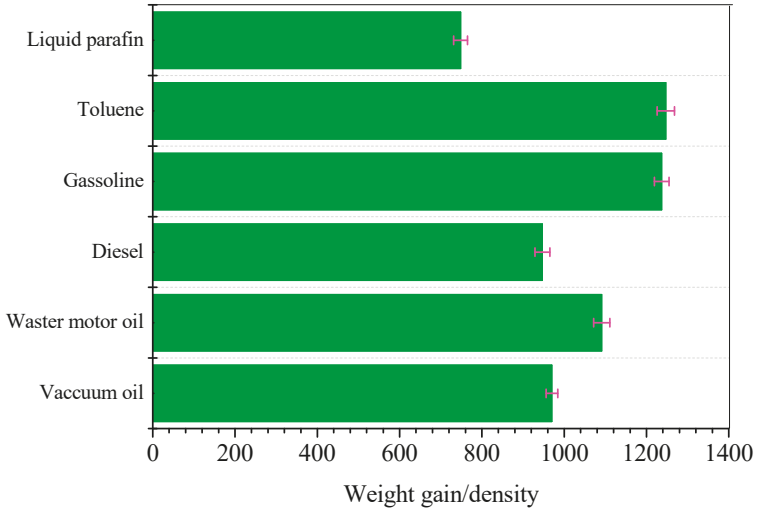

Figure 13. Absorption capacities normalized by the density of the respective oil or organic solvent.

Furthermore, for the recyclability test, the used absorbent was directly squeezed by hand and reused to absorb the oil and organic solvent. The absorption capacities of SCA for ten cycles are shown in Figure 14.

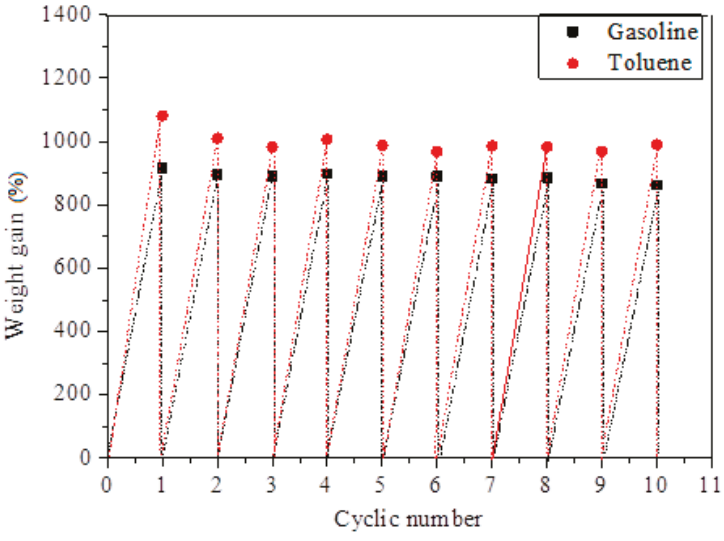

Figure 14. The cyclic adsorption capacity of sample SCA for gasoline and toluene.

After ten cycles, the adsorption capacity of the SCA for representative gasoline decreased from 916% to 862%. For toluene, the adsorption capacity decreased from 1081% to 989 % after ten cycles.

4. Conclusions

This paper reported the fabrication of a low density (0.084 g/cm^3) and highly porous (94.5%) green aerogel for the cleaning of oil and organic solvents from micron-size white bamboo fibrils (MWBF) with a very simple alkaline/ urea mixture solution method followed by a common freeze-drying process. FT-IR and EDX characterization were used to examine the surface morphology and chemical compositions of the silane-modified cellulose aerogel. The coating with MEMO silane for oil absorption purposes made the cellulose aerogel highly hydrophobic with water contact angles larger than 132.3 ± 6.92° and exhibited high absorption capacities of 1091 ± 19.6%, 1237 ± 17.6%, and 1247 ± 21.1% by weight gain for waste motor oil, diesel, and gasoline, respectively. Based on these results, the modified aerogels can be used to clean up oil spills and toxic chemicals in aquatic environments with the recyclability over 10 times.

Author Contributions: Conceptualization: D.D.N.; methodology: C.M.V.; validation: H.V.T.; formal analysis: C.M.V. and H.J.C.; investigation: C.M.V.; data curation: C.M.V. and D.D.N.; writing—original draft preparation: C.M.V. and H.J.C.; writing—review and editing: C.M.V. and H.J.C.

Funding: This research was funded by the Vietnam National Foundation for Science and Technology Development (NAFOSTED) under grant number 104.02-2017.15 (For Cuong Manh Vu) and HJC was partially supported by the National Research Foundation, Korea (2018R1A4A1025169).

Conflicts of Interest: The authors declare no conflict of interest.

References

1. Zhang, C.; Zhu, P.C.; Tan, L.; Liu, J.M.; Tan, B.; Yang, X.L.; Xu, H.B. Triptycene-Based Hyper-Cross-Linked Polymer Sponge for Gas Storage and Water Treatment. *Macromolecules* **2015**, *48*, 8509–8514. [CrossRef]
2. Howarth, A.J.; Liu, Y.; Hupp, J.T.; Farha, O.K. Metal-organic frameworks for applications in remediation of oxyanion/cation-contaminated water. *Cryst. Eng. Comm.* **2015**, *17*, 7245. [CrossRef]
3. Rey, A.; Mena, E.; Ch´avez, A.M.; Beltran, F.J.; Medina, F. Influence of structural properties on the activity of WO_3catalysts for visible light photocatalytic ozonation. *Chem. Eng. Sci.* **2015**, *126*, 80–90. [CrossRef]

4. Du, X.; You, S.; Wang, X.; Wang, Q.; Lu, J. Switchable and simultaneous oil/water separation induced by prewetting with a superamphiphilic self-cleaning mesh. *Chem. Eng. J.* **2017**, *313*, 398–403. [CrossRef]
5. Luo, Z.Y.; Lyu, S.S.; Fu, Y.X.; Heng, Y.; Mo, D.C. The Janus effect on superhydrophilic Cu mesh decorated with Ni-NiO/Ni(OH)$_2$ core-shell nanoparticles for oil/water separation. *Appl. Sur. Sci.* **2017**, *409*, 431–437. [CrossRef]
6. Liu, L.; Lei, J.; Li, L.; Zhang, R.; Mi, N.; Chen, H.; Huang, D.; Li, N. A facile method to fabricate the superhydrophobic magnetic sponge for oil-water separation. *Mater. Lett.* **2017**, *195*, 66–70. [CrossRef]
7. Ramezanalizadeh, H.; Manteghi, F. Design and development of a novel BiFeO$_3$/CuWO$_4$ heterojunction with enhanced photocatalytic performance for the degradation of organic dyes. *J. Photochem. Photobio A Chem.* **2017**, *338*, 60–71. [CrossRef]
8. Zhou, P.; Xie, Y.; Fang, J.; Ling, Y.; Yu, C.; Liu, X.; Dai, Y.; Qin, Y.; Zhou, D. CdS quantum dots confined in mesoporous TiO$_2$ with exceptional photocatalytic performance for degradation of organic pollutants. *Chemosphere* **2017**, *178*, 1–10. [CrossRef] [PubMed]
9. Kunaseth, M.; Poldorn, P.; Junkeaw, A.; Meeprasert, J.; Rungnim, C.; Namuangruk, S.; Kungwan, N.; Inntam, C. A DFT study of volatile organic compounds adsorption on transition metal deposited graphene. *Appl. Surf. Sci.* **2017**, *396*, 1712–1718. [CrossRef]
10. Yu, X.; Sun, W.; Ni, J. LSER model for organic compounds adsorption by single-walled carbon nanotubes: Comparison with multi-walled carbon nanotubes and activated carbon. *Environ. Pollul.* **2015**, *206*, 652–660. [CrossRef]
11. Doshi, B.; Repo, E.; Heiskanen, J.P.; Sirviö, J.A.; Sillanpää, M. Effectiveness of N,O-carboxymethyl chitosan on destabilization of Marine Diesel, Diesel and Marine-2T oil for oil spill treatment. *Carbohy. Polym.* **2017**, *167*, 326–336. [CrossRef] [PubMed]
12. Adebajo, M.O.; Frost, R.L.; Kloprogge, J.T.; Carmody, O.; Kokot, S. Porous Materials for Oil Spill Cleanup: A Review of Synthesis and Absorbing Properties. *J. Porous Mater.* **2003**, *10*, 159–170. [CrossRef]
13. Wahi, R.; Chuah, L.A.; Choong, T.S.; Ngaini, Z.; Nourouzi, M.M. Oil removal from aqueous state by natural fibrous sorbent: An overview. *Sep. Purif. Technol.* **2013**, *113*, 51–63. [CrossRef]
14. Huang, X.F.; Lim, T.T. Perfomance and mechanism of a hydrophobic-oleophilic kapok filter for oil/water separation. *Desalination* **2006**, *190*, 295–307. [CrossRef]
15. Wang, J.; Zheng, Y.; Wang, A. Investigation of acetylated kapok fibers on the sorption of oil in water. *J. Environ. Sci.* **2012**, *25*, 246–253. [CrossRef]
16. Deschamps, G.; Caruel, H.; Borredon, M.E.; Bonnin, C.; Vignoles, C. Oil Removal from water by selective sorption on hydrophobic cotton fibers. 1. Study of sorption properties and comparison with other cotton fiber-based sorbents. *Environ. Sci. Tech.* **2003**, *37*, 1013–1015. [CrossRef]
17. Rajakovic, V.; Aleksic, G.; Radetic, M.; Rajakovic, L. Efficiency of oil removal from real wastewater with different sorbent materials. *J. Hazar. Mater.* **2007**, *143*, 494–499. [CrossRef] [PubMed]
18. Choi, H.M.; Cloud, R.M. Natural sorbents in oil spill cleanup. *Environ. Sci. Tech.* **1992**, *26*, 772–776. [CrossRef]
19. Annunciado, T.R.; Sydenstricker, T.H.D.; Amico, S.C. Experimental investigation of various vegetable fibers as sorbent materials for oil spills. *Marin. Pollut. Bull.* **2005**, *50*, 1340–1346. [CrossRef]
20. Aegerter, M.A.; Leventis, N.; Koebel, M.M. *Aerogel Handbook*; Springer: New York, NY, USA, 2011; pp. 3–18.
21. Fang, W.Z.; Zhang, H.; Chen, L.; Tao, W.Q. Numerical predictions of thermal conductivities for the silica aerogel and its composites. *Appl. Therm. Eng.* **2017**, *115*, 1277–1286. [CrossRef]
22. Nazeran, N.; Moghaddas, J. Synthesis and characterization of silica aerogel reinforced rigid polyurethane foam for thermal insulation application. *J. Non-Crystall. Solid* **2017**, *461*, 1–11. [CrossRef]
23. Strobach, E.; Bhatia, B.; Yang, S.; Zhao, L.; Wang, E.N. High temperature annealing for structural optimization of silica aerogels in solar thermal applications. *J. Non-Crystall. Solid* **2017**, *462*, 72–77. [CrossRef]
24. Wu, X.; Li, W.; Shao, G.; Shen, X.; Cui, S.; Zhou, J.; Wei, Y.; Chen, X. Investigation on textural and structural evolution of the novel crack-free equimolar Al$_2$O$_3$-SiO$_2$-TiO$_2$ ternary aerogel during thermal treatment. *Ceramic. Inter.* **2017**, *43*, 4188–4196. [CrossRef]
25. Zheng, Q.; Cai, Z.; Gong, S. Green synthesis of polyvinyl alcohol (PVA)–cellulose nanofibril (CNF) hybrid aerogels and their use as superabsorbents. *J. Mater. Chem. A* **2014**, *2*, 3110–3118. [CrossRef]
26. Tripathi, A.; Parsons, G.N.; Khan, S.A.; Rojas, O.J. Synthesis of organic aerogels with tailorable morphology and strength by controlled solvent swelling following Hansen solubility. *Sci. Rep.* **2018**, *8*, 2106. [CrossRef]

27. Guo, H.; Meador, M.A.B.; McCorkle, L.; Quade, D.J.; Guo, J.; Hamilton, B.; Cakmak, M.; Sprowl, G. Polyimide Aerogels Cross-Linked through Amine Functionalized Polyoligomeric Silsesquioxane. *ACS Appl. Mater. Interfaces* **2011**, *3*, 546–552. [CrossRef]
28. Feng, J.; Wang, X.; Jiang, Y.; Du, D.; Feng, J. Study on Thermal Conductivities of Aromatic Polyimide Aerogels. *ACS Appl. Mater. Interfaces* **2016**, *8*, 12992–12996. [CrossRef]
29. Zhang, Y.; Yin, M.; Lin, X.; Ren, X.; Huang, T.S.; Kim, I.S. Functional Nanocomposite Aerogels Based on Nanocrystalline Cellulose for Selective Oil/Water Separation and Antibacterial Applications. *Chem. Eng. J.* **2019**, *371*, 306–313. [CrossRef]
30. Yue, X.; Zhang, T.; Yang, D.; Qiu, F.; Li, Z. Hybrid aerogels derived from banana peel and waste paper for efficient oil absorption and emulsion separation. *J. Clean. Prod.* **2018**, *199*, 411–419. [CrossRef]
31. Carmody, O.; Frost, R.; Xi, Y.; Kokot, S. Surface characterisation of selected sorbent materials for common hydrocarbon fuels. *Surf. Sci.* **2007**, *601*, 2066–2076. [CrossRef]
32. Silva, T.C.F.; Habibi, Y.; Colodette, J.L.; Elder, T.; Lucia, L.A. A fundamental investigation of the microarchitecture and mechanical properties of tempo-oxidized nanofibrillated cellulose (NFC)-based aerogels. *Cellulose* **2012**, *19*, 1945–1956. [CrossRef]
33. Sai, H.; Xing, L.; Xiang, J.; Cui, L.; Jiao, J.; Zhao, C.; Lia, Z.; Lia, F. Flexible aerogels based on an interpenetrating network of bacterial cellulose and silica by a non-supercritical drying process. *J. Mater. Chem. A* **2013**, *1*, 7963–7970. [CrossRef]
34. Cai, J.; Kimura, S.; Wada, M.; Kuga, S.; Zhang, L. Cellulose Aerogels from Aqueous Alkali Hydroxide–Urea Solution. *Chem. Sus. Chem.* **2008**, *1*, 149–154. [CrossRef]
35. Cervin, N.T.; Aulin, C.; Larsson, P.T.; Wagberg, L. Ultra porous nanocellulose aerogels as separation medium for mixtures of oil/water liquids. *Cellulose* **2012**, *19*, 401–410. [CrossRef]
36. Feng, J.; Nguyen, S.T.; Fan, Z.; Duong, H.M. Advanced fabrication and oil absorption properties of super-hydrophobic recycled cellulose aerogels. *Chem. Eng. J.* **2015**, *270*, 168–175. [CrossRef]
37. Jin, C.; Han, S.; Li, J.; Sun, Q. Fabrication of cellulose-based aerogels from waste newspaper without any pretreatment and their use for absorbents. *Carbohyd. Polym.* **2015**, *123*, 150–156. [CrossRef] [PubMed]
38. Stalder, A.F.; Melchior, T.; Müller, M.; Sage, D.; Blu, T.; Unser, M. Low-bond axisymmetric drop shape analysis for surface tension and contact angle measurements of sessile drops. *Colloid Surf. A Physicochem. Eng. Asp.* **2010**, *364*, 72–81. [CrossRef]
39. Wang, M.; Ma, Y.; Sun, Y.; Hong, S.Y.; Lee, S.K.; Yoon, B.; Chen, L.; Ci, L.; Nam, J.D.; Chen, X.; Suhr, J. Hierarchical porous chitosan sponges as robust and recyclable adsorbents for anionic dye adsorption. *Sci. Rep.* **2017**, *7*, 18054. [CrossRef] [PubMed]

materials

MDPI

Article

Study of the Suitability of Different Types of Slag and Its Influence on the Quality of Green Grouts Obtained by Partial Replacement of Cement

Francisca Perez-Garcia [1], Maria Eugenia Parron-Rubio [2,*], Jose Manuel Garcia-Manrique [1] and Maria Dolores Rubio-Cintas [2]

[1] Departamento de Ingeniería Civil, Materiales y Fabricación, Universidad de Málaga, 29071 Málaga, Spain; perez@uma.es (F.P.-G.); josegmo@uma.es (J.M.G.-M.)
[2] Departamento de Ingeniería Industrial y Civil, Universidad de Cádiz, 11202 Algeciras, Spain; mariadolores.rubio@uca.es
* Correspondence: mariaeugenia.parron@uca.es

Received: 18 March 2019; Accepted: 8 April 2019; Published: 10 April 2019

Abstract: This paper is part of a research line focused on the reduction of the use of cement in the industry. In this work, the study of work methodologies for the manufacture of green cementitious grout mixtures is studied. Grout is widely used in construction and it requires an important use of raw materials. On the other hand, the steel industry faces the problem of the growing generation of slag wastes due to the increase in steel manufacturing. The green grout aims to achieve the dual objective of reducing the demand for cement and improve the slag waste valorization. Slag is not introduced as an aggregate but through the direct replacement of cement and no additives. The research seeks a product where we can use steel slag intensively, guaranteeing minimum resistance and workability. Results with substitutions between a 25% to 50% and water/cement ratio of 1 are presented. In particular, the suitability of different slags (two Ladle Furnace Slag (LFS) and one Blast Furnace Slag (GGBS)) in the quality of the final product are analyzed. The feasibility of replacing cement with slag and the importance of the origin and pretreatment are highlighted.

Keywords: cementitious grout; green grout; cement; slag substitution; valorization; circular economy

1. Introduction

One of the most important challenges that society faces is to achieve a balance between the consumption of raw materials and our need for development. The future evolution of the industrial activity must include criteria of both efficiency and reuse of waste. The dimension of transformation must be limited to a sustainable environment where the global needs could be satisfied without severely compromising those of future generations (Brundlandt Report, 1987) [1]. To achieve this sustainable environment, actions must be taken in the reduction of harmful gas emissions (greenhouse effect) and the reduction of the use of natural raw materials.

One way to reduce the use of raw materials is to lead our efforts toward objectives such as those proposed in the circular economy theory, being aware that we inhabit a world with finite resources.

Therefore, the essence of the circular economy is to optimize the reuse of the generated resources and introduce them back into the production chain. This process, known as waste valorization [2], has become more and more important and today is a field of research with great potential.

Our efforts are focused on the construction industry, in particular, in the process of manufacturing cement-based materials. It is a fundamental element due to its role as a binding component in different mixtures. In order to reach a sustainable environment, the production of cement should be reduced.

One of the reasons is to minimize the extraction of limestone, but more significant is the reduction of energy consumption and on greenhouse gas emissions.

Throughout the entire process, the estimated CO_2 release during clinker manufacture is around 0.7 to 0.9 tons per Portland cement ton, which means that the cement industry generates between 7 and 9% of CO_2 worldwide. The decrease of these emissions is the trigger of the notable research interest in making progress toward reducing the industry's dependence on cement [3–6]. As an alternative to the use of cement, its partial replacement by other materials is proposed. At this point, the idea of valorization of existing waste in the industry itself becomes important.

Steel slag is a byproduct of steel manufacturing, which is obtained by the chemical reactions that take place in the processes of metal formation. It is a complex solution of silicates and oxides produced during the separation of the molten steel from impurities. The properties of the slag produced during steel making depends on many factors, mainly the manufacturing process. According to Setie et al. [2], four types of steel slag can be distinguished: electric arc furnace (EAF) slag, blast furnace slag (GGBS), basic oxygen furnace slag (BOFS), and ladle furnace slag (LFS) [7–9].

The EAF is a strong, dense, nonporous aggregate that is cubical in shape, has good resistance to polishing, and has an excellent affinity to bitumen. Therefore, EAF are more suitable for engineering purposes. The EAF slags can be also divided in two types: oxidizing or black (EAFS) and reducing or white (LFS). In a usual manufacturing process of steel, the EAFS produced is in the order of 110–130 kg per metric ton, and the LFS white one is about 20–30 kg per metric ton.

The increase in steel consumption supposes a proportional increase in the generation of this slag's waste. The strategies of waste valorization of the slags are diverse but not sufficient to achieve in practice a real reuse of these. Either by regulatory or economic problems. The steel slags are used in many areas, from fertilizers to civil industry. In the European Union, it has been used as an additive to make up the cements. The slag properties make them very appropriate for aggressive environments. Slags improve their resistance against salt water and sulphates (maritime facilities). In the last few decades, research efforts have been focused on its use as additives or as aggregate substitutes with arid, both fine and coarse, or as a substitute of arid as a bituminous binder in the pavement layer [10–20].

In the literature, we can find some recent and interesting works about cementitious grouts containing supplementary materials. In 2015, Celik et al. [21] investigate the mixture of rice husk ash in cement-based grout, the rheological properties of the mixture result in the increase in apparent viscosity. Amahjour et al. [22] (2002) or Pastor et al [23] (2016) add fly ash and silica fume to increase mechanical strength.

There are also studies where the substitutions of blast furnace slag are made in small percentages but always with chemical additives. Azadi et al. [24] (2013) worked with chemical additives to optimize the grout. They used sodium silicate (Na_2SiO_3) to increase resistance, sodium carbonate (Na_2CO_3) to reduce bleeding, or triethanolamine (TEA) to promote injection. In 2017, Zhang [25] introduced sodium silicate for quick adjustment.

An interesting research in this area is that done by Krishnamoorthy et al. [26]. In this study a cementitious grout containing supplementary cementitious materials (SCM) (fly ash, silica fume, GGBS) are presented. The results on flow characteristics, strength, and durability show that cementitious grouts containing SCM can be used successfully to repair concrete structures. They reach percentage substitution of 20 to 40% of GGBS slags with water/cement ratios of 0.25 to 0.40.

Huang [27] presented the study on cement ash slurries containing polypropylene (PP), fiber, and super plasticizer. With the addition of PP fiber, better resistance against cracking, sulphate attack, and volume changes was observed, but resulted in a higher viscosity and permeability. Bastien et al. [28] studied the properties of cement slurries with a low ratio of cement and water with superplasticizer and a low proportion of precipitated silica (3% by weight of cement). The rheological properties were also investigated. It is possible to obtain slurry mixtures with zero bleeding, good fluidity, and high compressive strength that meet the requirements for the use of post-tensioning.

Shannag [29] studied cementitious grouts, adding silica fume and natural pozzolan to achieve high performance. This incorporation results in a high fluidity, zero bleeding, high strength, and satisfactory shrinkage.

The literature indicates that the desirable properties for the grouts are that they must possess good fluidity, reduction of bleeding, initial setting time that is not too short, adequate strength, and durability.

Our line of research seeks to advance in the study of the technical feasibility of replacing cement with slag from the steel industry [30], both for the production of green concrete [7,31] and green cementitious grout.

However, there are many factors involved, as the properties of the resulting product related not only mechanical properties, but also durability, that are correlated with the characteristics of the slag used and its proportion.

This paper presents the results obtained in a set of tests for the manufacture of green grouts in a substitution dosage that varies between 0 and 50%. The substitutions have been made on cement Portland (CEM I). Unlike Portland CEM III and IV cements, which already have slag incorporations in their manufacture [32,33], our objective is to evaluate the possibility of working the cementitious grout with recycled material directly [34]. In particular, each mixture has been subjected to a test campaign of a slump test, compressive and bending tests, and exudation test. As mentioned, it is part of a wide "program intended to elaborate a standard to guide the use of steel slag as cement substitute" [7,31].

In the resulting discussion, the optimized simplification of the parameters of the model is considered when admitting that each phase of the material is subject to a similar tension that eliminates the influence of the form, the size, and the disposition of the phases. Therefore, the only factors that this approach considers are the concrete's resistance properties in relation to the replacement of some of its components by slag. The models are complicated, taking into account the case that the cement paste is the connection phase, where the inclusions form a disconnected phase [35].

A fundamental parameter to analyze will be the different behavior obtained (quality of the Green Grout) according to the characteristics of the slag. Two key aspects, the origin of the slag (dependent on the type of steel produced) and the treatments to which the slag have been subjected becomes determinant. In this research, slag from different origins within the country have been studied. The results obtained, such as those presented in a previous work for the case of concrete [7], are very positive and show the feasibility of the mixture.

On the following section, the materials analyzed are described. Then, a brief overview of the tests performed is made. In the next section, results are presented and discussed. Finally, the fundamental conclusion and lines of future research are summarized.

2. Materials

This article focuses on the progress made in replacing material in cementitious grout mixtures. This material has a wide presence in civil constructions. Two of the applications where this research presents potential applicability are the jet grouting, for the improvement of soil, and the execution of deep foundations such as micropiles. In the jet grouting process, the slurry is injected into the soil pores in order to fill and create cohesion, which increases the resistance characteristics or, equivalently, improves its mechanical properties [24,36]. Therefore, the rheological properties of grouts are directly related to the pumping capacity to penetrate holes and cracks [21].

One of the fundamental parameters in cement-based grout is the water/cement ratio by weight. Depending on the application, different relationships are recommended. In applications of foundation by injection, the cementitious grout needs to behave like a fluid able to penetrate the soil or rock so the ratio will vary between 0.6 and 2. In sealed works, it varies between 0.5 and 1. Figure 1 presents a schematic of these recommendations.

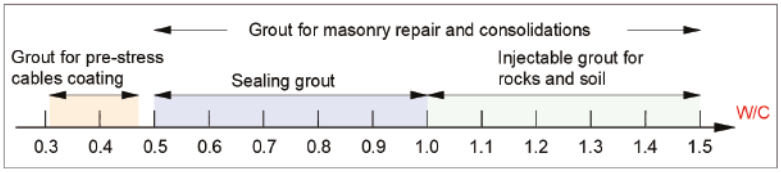

Figure 1. Schematic water–cement ratio (W/C) depending on the application.

Ten different mixes were designed by substituting a 30%, 40% and 50% of cement by slags (% in weight) obtained from three different blast furnaces in Spain, according to previous works with concrete [7,31]. Table 1 shows the cement and slag chemical composition (data provided by the supplying company). Table 2 presents the nomenclature used for the mixtures.

Table 1. Cement and slag chemical composition (data provided by the supplying company).

Slag Origin/Chemical Composition	SiO_2	Al_2O_3	CaO	Fe_2O_3	MgO	Na_2O	K_2O
	%	%	%	%	%	%	%
Cement	20–22	4–10	55.62	4	2	0.3	0.3
Slag GGBS (S1)	35.9	11.2	40	0.3	7.7	0.2	0.4
Slag LFS 1 (S2)	22.28	9.37	56.94	0.84	7.37	0	-
Slag LFS 2 (S3)	15.85	16.53	57.56	0.83	7.7	-	-

Table 2. Cementitious grout mixtures composition.

Mix Denomination	Slag	Substitution
S0	-	0%
S1_30	GGBS	30%
S1_40	GGBS	40%
S1_50	GGBS	50%
S2_30	LFS 1	30%
S2_40	LFS 1	40%
S2_50	LFS 1	50%
S3_30	LFS 2	30%
S3_40	LFS 2	40%
S3_50	LFS 2	50%

The used cement was Portland Cement CEM I 42.5 R (EN 197-1 [37], Holcim, Málaga, Spain). This cement was selected due to the absence of any kind of additive that could mask the results. It was used as reference pattern. Density: 3150 kg/m^3. Specific surface area: >280 m^2/kg. The water–cement ratio used was 1.

Three different slags are used (S1, S2 and S3). The first of them, S1, was a ground granulated blast furnace slag (GGBS) with mechanical processing. It presented a maximum grain size of 0.063 mm, density of 2910 kg/m^3, and specific surface area of 462 m^2/kg. On the other hand, S2 and S3 types were unprocessed ladle furnace slag (LFS) from two different steel mills. The only process they were subjected to was sieving in the lab with a 0.063 mm sieve. The fraction obtained through sieving was 23% and 15% by weight, respectively.

Chemical composition of the slags and cement used in the grouts mixtures is shown in Table 1. This chemical composition was proportionated by the slag supplier companies and it refers to the slags before the sieving process when needed in the laboratory.

As can be seen in Table 1, the chemical composition of the different slags varied for each of them, especially the percentage of SiO_2 and CaO.

The materials employed in this work did not include any type of additive because the objective of the research was to determine how the different slags behaved as substitutes of the binder without being affected by any additional parameter.

3. Tests Description

The mixes described in previous section were subject to different standard tests. The objective of these tests was to evaluate how cement-slag substitution may affect the main properties such as consistency, workability, and mechanical capabilities (compressive and flexural strength).

The batching was prepared according to the European standard used in the manufacture of cement grouts: EN 447 [38]. The laboratory conditions were 24 and 26 °C (temperature) and 40% relative humidity. An electric mixer of robust construction was used, with two speeds of rotation, with a mixing paddle with an anchoring system according to EN 196/1 [39].

Using the dispensing hopper, the Portland cement was incorporated into the mixing bowl with the slag where it was mixed for 90 s, then the water was added, again mixing for 180 s (Figure 2). For each of the mixtures, nine prismatic test specimens of $4 \times 4 \times 16$ cm^3 were prepared. Each one according to the EN 12390-2 standard [40] for hardened concrete where the methods for the manufacture and curing of specimens destined for the performance of resistance tests are described.

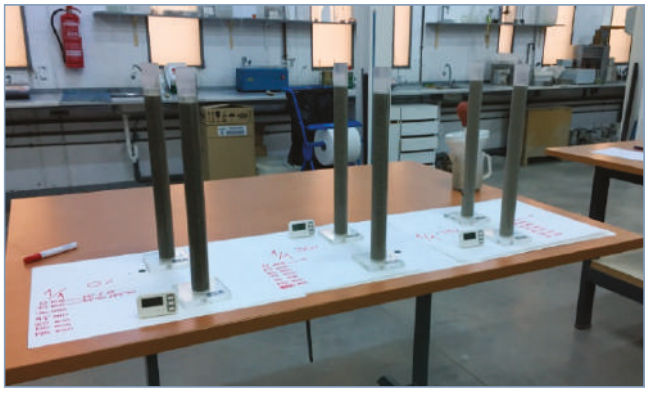

Figure 2. Exudation tests.

3.1. Flow Cone Test

The test for the flow of grout mixtures (flow cone method) was determined according to the norm EN 445 [41]. The test determines the time of efflux of a specified volume of fluid cement grout through a standardized flow cone.

Before beginning, the inside of the cone was moistened by filling the cone with water. The water was drained from the cone one minute before the test. The grout was poured slowly to prevent trapped air. The quantity tested was one liter of mix. Once full, the stopwatch was started, and simultaneously, the stopper was removed. The recorded result was be the time in which the entire grout passed through the cone.

3.2. Flexural Strength Test

The test was carried out at 7, 28 and 90 days for all the test pieces (nine prismatic test specimens for each mixture) according to EN 196-1 [39] and EN 196-7 [42] standards for cements. The test machine was equipped with a bending device incorporating two steel support rollers and a third steel loading roller of the same diameter and equidistant from the other two. The length of these rollers was between 45 and 50 mm. The load was applied continuously and without sudden shocks. The force did not

begin to be applied until the load roller and the support rollers rest firmly on the specimen. The rate increase R was 16 N/s, according to the expression:

$$R = \frac{2}{3} \times \frac{S \cdot d_1 \cdot d_2^2}{l} \times \frac{N}{s} \quad (1)$$

where d_1 and d_2 are the dimensions of the square section of the specimen and $l = 3 \times d$ is the distance between the rollers in millimeters.

The force signal was provided by an adjustable load cell to the upper, lower, or base bridge. It was formed by a strain gauge Wheatstone bridge, adhered to a structure. The force captured by the load cell was, due to its location, the same as that of the specimen under test; that is, there was a direct coupling between the test piece and the load cell. The machine was controlled by a computer through an ETIWIN control software, with ENAC (National Accreditation Entity in Spain) calibration certificate.

3.3. Compressive Strength Test

The test was performed at 7, 28, and 90 days as a bending test according to standards EN 196-1 [39] and EN 196-7 [42]. The number of specimens tested was 18 and an average value was calculated. According to Neville [43], the compressive strength of the modified cubic specimen would be 5% higher than the standard cubic specimen. An average value was obtained from this study because only two specimens per flexural strength test were performed.

The test was carried out with the same machine, model ETIMATIC-Proetisa H0224 (Production of Technical and Industrial Equipment, Madrid, Spain). The applied pressure was at an invariant rate of 0.5 MPa/s. The compressive strength is given by the expression:

$$f_c = \frac{F}{A_c} \quad (2)$$

where f_c is the compressive strength in MPa, F is the maximum breaking load expressed in N, and A_c is the cross-sectional area of the specimen given in mm^2.

3.4. Exudation Test

This test gives the exudation of the grout. It was carried out according to EN 445 [41] (Figure 2). Exudation was measured as the volume of water remaining on the surface of the mix that was kept protected from evaporation. The variation in volume was measured as a difference in percentage of the volume of the grout between the start and the end of the test. The test mainly measured the volume variation caused by sedimentation or expansion. A transparent tube, approximately 60 mm in internal diameter and around 1 m in length, was used. The tube was placed in a vertical position with the top end open. It ensured a rigid fixation that prevented any movement or vibration. The grout was poured into the tube with a constant flow to ensure that no trapped air remained. The tube was filled to a height, h_o. The ambient temperature of the laboratory was 18.1 °C and the grout acquired a temperature of 18.3 °C. The start time t_0 and the height h_0 were recorded. The height of the cement grout, h_g, was recorded at intervals of 15 min during the first hour, and then at 2 h, 3 h, and 4 h. The height of the exuded water, h_w, was recorded at the same time as the measurements of the grout were made. Possible heterogeneities that could be seen in its appearance through the transparent tube were recorded. The volume variation was:

$$h_w/h_o \times 100\% \quad (3)$$

4. Interfacial Transition Zone Review

Before presenting the data, the basic principles of mixing models based on the interfacial transition zone are reviewed (ITZ) [44]. This model usually applied to concrete assumes that the material is idealized as a composite of mortar and aggregate, where any arbitrarily small volume contains both

mortar and aggregate in fixed proportions [45]. The same hypothesis can be applied to the cementitious grout, which properties will be very influenced by the microstructure. This can be classified into three phases: aggregate, cement paste, and the interfacial transition zone (ITZ). ITZ has a critical role. This transition zone has a size comparable with the size of cement grains.

The effects of varying the percentage of slag substitution affects the state of the structure and causes an improvement in fluency. This leads us to expect an increase in the mechanical strength of the hardened grout. There are few studies on this phenomenon, due to it being difficult to find suitable definitions. It is a new diffuse distribution of the particles in the grout. The global grain size does not change, but the permeability evolves. If locally transported particles do not migrate further, an obstruction occurs that accompanies an overpressure. In short, the substitution of cement by slag results in a redistribution of the fine particles without modification of the total solid volume of the specimen.

Below, the formulation of these models are summarized. The partial densities for the three constituents are given by the following expressions:

$$\rho^s = \rho_s(1-\varphi) \tag{4}$$

$$\rho^w = \rho_w \varphi(1-c) \tag{5}$$

$$\rho^c = \rho_c \varphi\ c \tag{6}$$

Where ρ_s, ρ_w, and ρ_c are the real densities of the skeleton, water, and fluidized cement paste, respectively. The porosity, φ, defines the proportion of the holes in relation to the total volume. "c" is the concentration in the cement paste of the ITZ zone. It represents the total volume of the particles transported from the skeleton by the filtering forces in the void volume. The fraction of the mass of the fluidized solid is:

$$c_m = c\rho_w/(c\rho_w + (1-c)\rho_c) \tag{7}$$

Applying the mass conservation equations to each phase, Equation (8) presents the variation of mass for solid phase, Equation (9) for liquid phase, and Equation (10) for fluidized solid:

$$\frac{\partial \rho^s}{\partial t} + \nabla.(\rho^s v^s) = m^s \tag{8}$$

$$\frac{\partial \rho^w}{\partial t} + \nabla.(\rho^w v^w) = 0 \tag{9}$$

$$\frac{\partial \rho^c}{\partial t} + \nabla.(\rho^c v^c) = m^c \tag{10}$$

where "m" represents the typical variation of the mass of that constituent ($m^w = 0$), "t" is the time and ∂ is the gradient operator. Assuming that all the particles transferred from the skeleton re-enter the fluid, the following mass can be established:

$$m^c + m^s = 0 \tag{11}$$

It will be assumed, on the other hand, that the slag transported via filtration in the slurry moves with the same speed as the particles near the ITZ zone. This relationship translates the particular nature of the phenomenon that is considered in the framework of this study. There is, for example, no chemical reactions that cause a divergence between the mass transported from the solid skeleton per unit of time and that which is transformed into cement paste at the same time. The previous hypothesis also assumes that the ITZ does not significantly modify the proportions between the different phases that constitute the initial sample. Therefore, the initial variation and the temporal evolution of ρ_s (density of the solid skeleton) remain negligible. This means, in particular, that this phenomenon does

not develop considerably and causes little variation in the initial properties of the fluidized cement paste in, for example, its density.

5. Results and Discussion

In this section, the main results obtained are presented and discussed. The results obtained in each test are summarized for the proposed mixtures (Table 2). In general, the results between them were analyzed based on the reference mixture without any substitution (S0). The results were also compared with the works of Krishnamoorthy et al. [27]. The results presented in this paper had a higher percentage of substitution and a higher W/C ratio in addition to introducing the use of LFS slag. However, the similar evolution of the parameters studied for GGBS slag was checked.

5.1. Flow Cone Test Results

Flow cone test results are shown in Figure 3. It can be observed that there were no significant differences among the mixtures. The flow cone test results were always within an interval from 8.5 to 9 s. The main implication here is that the use of these types of slags as substitute of cement in cementitious grout had no significant effect in the fluidity of the resultant mix, at least in substitution percentages of up to 50%.

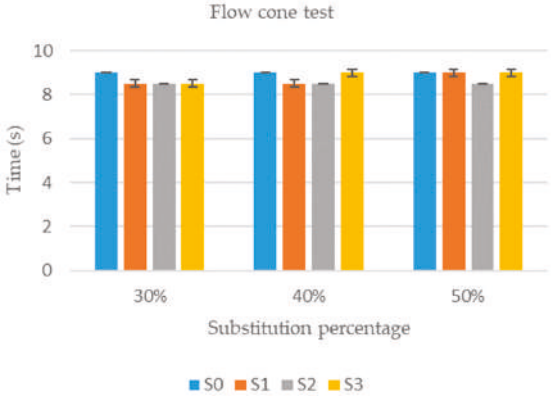

Figure 3. Flow cone test results.

This is an important conclusion because these new mixtures will not present disadvantages in their application with respect to the original ones while being able to take advantage of the same implementation technologies.

5.2. Flexural Strength Test Results

Flexural strength test results are shown in Table 3 for 10 mixtures at 7, 28, and 90 days. In Figure 4, the data are grouped according to time and percentage of substitution for each slag type. Figure 5 also allows for analyzing the behavior of each mixture with respect to the reference. Each result curve (MR) is non-dimensioned with respect to the corresponding value of S0 (MR_{S0}).

None of the mixes with slag substitution achieved the flexural strength reference (S0) at 7 days. However, at 28 days, the MR difference was reduced between S0 and two of the slag types (S1 and S2). One of the effects observed with slag was that the hardening process of the mixture was modified and delayed. As it has been observed in concrete mixtures incorporating GGBS slags as partial cement replacement, the strength at early stages was lower in comparison with traditional concrete. The results obtained in this work are in accordance with the results shown in previous works (Parron-Rubio et al. [7]).

No direct correlations were identified for each type of slag and its improvement with respect to MR.

Table 3. Flexural strength results.

Mixes	7	28	90	% Strength Gain at 90 Days
S0	2.45	3.36	3.92	-
S1_30	1.80	2.65	4.07	3.8%
S1_40	1.70	3.28	4.28	9.18%
S1_50	1.65	3.46	4.63	18.1%
S2_30	1.44	2.90	4.29	9.4%
S2_40	1.70	3.5	3.69	−5.9%
S2_50	1.35	2.61	3.60	−8.2%
S3_30	1.17	2.39	2.21	−43.6%
S3_40	0.88	1.83	1.46	−62.8%
S3_50	0.51	1.16	1.29	−67.1%

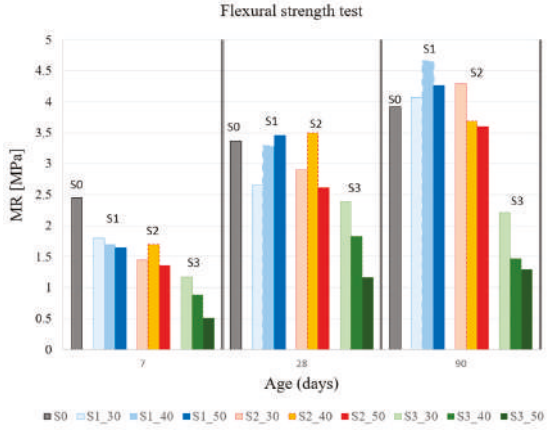

Figure 4. Results of flexural strength test (MR)(MPa).

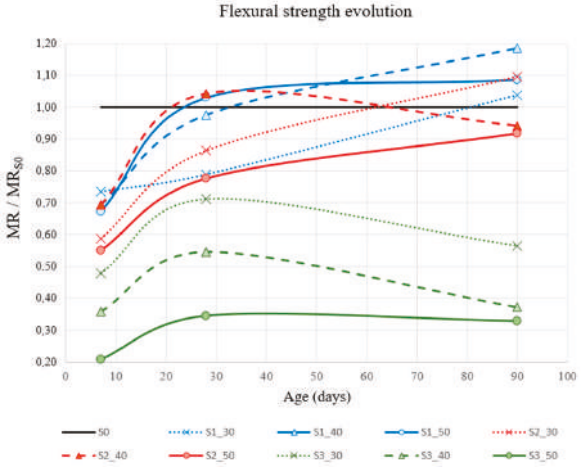

Figure 5. Flexural strength evolution (MR/MR$_{S0}$).

S1 mixtures showed a higher flexural strength than S2 and S3 mixtures. In the literature, there are some works that indicate that pozzolanic materials with a high SiO_2 content have better mechanical properties than pozzolanic materials with a low content of SiO_2 [7,46]. This can be the reason why S1 mixtures showed the highest flexural strength due to their highest SiO_2 content in comparison with S2 and S3 slags.

It seems that each slag had a particular dosage that optimized its behavior in the test. The S1_40 mix showed the best performance overall in this test, obtaining a flexural strength gain of up to 18.6% at 90 days with the 40% substitution.

S1 slags were unique in presenting an increase in flexural strength at 90 days for every substitution fraction (S1_30, S1_40, and S1_50). On the other hand, S3 slag showed poor results for this test. As it can be observed in Figure 4, flexural strength loss for this type of slag appeared at 7, 28, and 90 days. It seems that in this type of slag, the hardening stopped after 28 days. Actually, our conclusion is that from there it is maintained. We do not consider that the small decrease observed in Figure 4 is representative of any behavior, but is the consequence of some distortion of results.

5.3. Compressive Strength Test Results

Compressive strength test results are shown in Table 4 for 18 test specimens at 7, 28, and 90 days. In Figure 6, the data are grouped according to time and percentage of substitution for each slag type (S1, S2, and S3). Figure 7 also allows for analyzing the behavior of each mixture with respect to the reference. Each result curve (Rs) is non-dimensioned with respect to the corresponding value of S0 (Rss_0).

Table 4. Compressive strength results.

Mixes	7	28	90	% Strength Gain at 90 Days
S0	6.29	8.89	12.52	-
S1_30	4.40	6.98	13.25	5.8%
S1_40	4.38	8.66	14.97	19.6%
S1_50	4.50	11.41	16.90	35.0%
S2_30	3.20	6.41	9.27	−26.0%
S2_40	3.98	8.08	9.09	−27.4%
S2_50	3.15	6.27	7.34	−41.4%
S3_30	2.23	4.42	4.42	−64.7%
S3_40	1.65	3.33	3.17	−74.7%
S3_50	1.02	2.05	1.98	−84.2%

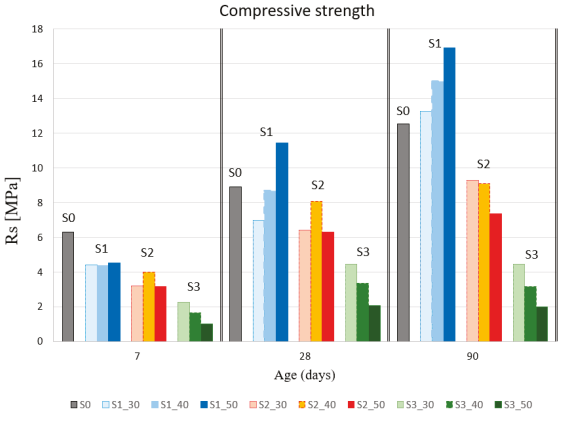

Figure 6. Results of compressive strength test (Rs)(MPa).

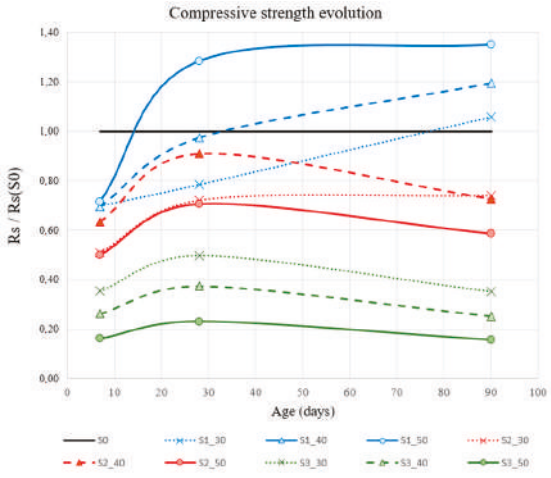

Figure 7. Compressive strength evolution ($Rs/Rs_{(S0)}$).

As for the flexural strength results, none of the mixes obtained a compressive strength gain at 7 days with respect to the reference grout mixture. The behavior at 28 and 90 days of the different mixes differed depending on the type of slag and the slag–cement substitution percentage.

The compressive strength of S1 slag grew as the substitution percentage increased. The behavior of the 40% mixture was similar to the 30%. The best compressive performance is attributed to the 50% mixture, which obtained a strength gain at 28 and 90 days of 28.35% and 35%, respectively.

The behavior of S2 slag at 7 days was similar for every substitution percentage and was about 30% less than the reference grout mixture at the same age. S2 mix obtained strength loss at 28 days for every substitution percentage, with the 40% mix (S2_40) the one performing the best, followed by the 30% mix and 50% mix. However, the results for 90 days show a relationship between substitution percentage and compressive strength, with the latter being greater as the substitution percentage decreased.

The compressive strength loss obtained using L3 mixes, at every stage and percentage substitution, was significant. Furthermore, the loss was greater as the substitution percentage increased. As in the case of the flexural strength, the mixtures with GGBS slags showed a higher compressive strength than LFS slags.

Krishnamoorthy et al. [27] presents results of variation of compressive strength with GGBS slags. They test them from porous concrete blocks containing a mixture of supplementary cementitious materials including fly ash, GGBS, and silica fume. One of them was prepared with a grouting mixture of ordinary Portland cement, 40% GGBS as aggregate, water–cement ratio of 0.35, and 1% superplasticizer. Although it is a different product, we can observe a similar slight improvement in the compressive strength.

5.4. Exudation Test Results

The results of the exudation test are shown on the Figure 8.

It can be distinguished in the figure that the mixture without substitution of cement by slag was the one that showed a higher percentage of water exudation at 240 min, obtaining a value of almost 30%.

GGBS (S1) mixtures had low values of exudation at early stages up to 120 min and obtained the lowest percentages at 240 min, except for the S2 mixture with 50% substitution.

LFS1 (S2) slag showed an exudation behavior similar to the reference mixture, although they obtained water exudation percentages superior to those of the rest of the slags.

Regarding the percentage substitution, the results clearly show that with higher substitution percentages, the exudation decreased.

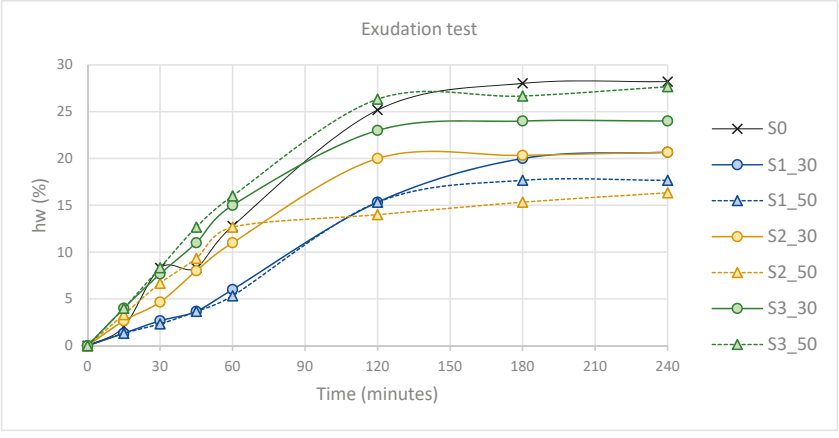

Figure 8. Exudation test.

6. Conclusions

In this paper, experimental results obtained from grouts with cement substitutions by slags in a dosage of up to 50%, W/C ratio of 1, and no additives are presented. The results for different white slags are studied (GGBS and LFS). All the specimens have been tested for exudation, compressive strength, and flexural strength to analyze the feasibility of the mixture for industrial applications. According to the results described in previous sections, the following conclusions can be highlighted:

In general, the mixtures obtained show an improvement in factors such as fluency and viscosity. The slags had a lower density than cement and cause a mixture more fluid. This was an improvement in application where this factor was important.

The mechanical response was less homogeneous and depended greatly on the origin of the slag, as expected. Improvements were observed in the results of compression and bending strength for mixtures with S1 slags (10% in bending and 35% in compression test). However, slag types S2 and S3 gave rise to mixtures with losses of resistance of 85% in compression with respect to the reference. This was due to the lower content of SiO_2 in slags S2 and S3 (LFS) in comparison with S1 slag (GGBS). It has been proven that there was a great difference between slags according to their origin, not only for its composition, but also for the treatment received prior to mixing. Therefore, each generator of slag waste required a study of the goodness of its product in terms of its use as a cementitious substitute. However, the tests seemed to indicate that an adequate treatment increased the potential valorizing of the waste in question.

In the conventional slurry, the aggregate was the least deformed; therefore, this was where the tensions were concentrated. They were then transferred to the ITZ. The green grouts (with cement substitution by slag) had a lower density rate. This increased the speed of the mechanism of the conservation equation of the mass. This filled the microstructural spaces, facilitating the adherence between the aggregate and the cement paste inside the transition.

In addition, the resultant cement grout was a sustainable material with a lower cost in comparison with traditional cement grouts.

The fundamental conclusion of this study was to verify the feasibility of obtaining mixtures with cement substitution by slag. A 50% reduction in the cement used in the mix was achieved, and at the same time, the viability of the grout was maintained. The fluidity obtained allows for use in

applications where there can be an intensive use of this grouts, such as jet-grouting for mixtures S1 and S2, or ground improvements for S3 mixtures

Higher cement substitution levels using slag waste may also be possible but this would require further investigation.

GGBS slags improved the mechanical and workability capabilities of the resulting mixture. The LFS slags studied in this work can be employed in other types of works where a high strength is not required. Therefore, this conclusion presents an opportunity to improve waste slag valorization if we progress in the high-level percentage of substitution with slags in ordinary products such as grouts or concrete.

Author Contributions: All the authors conceived and designed the experiments, and analyzed the results; F.P.-G. and M.E.P.-R. performed the experiments; M.D.R.-C. and J.G.-M. coordinated and wrote the paper.

Funding: The authors acknowledge the financial support provided to this work by the European Regional Development Fund (ERDF) as part of the Operational Programme Smart Growth 2014–2020. As well as the Center of Industrial Technological Development (CDTI) of the Ministry of Economy and Competitiveness as a part of the research project IDI-20160509 through the companies DRACE and GEOCISA.

Acknowledgments: The authors acknowledge to the technicians Manuel García Pareja and Maria José Rodríguez Aranda from the Polytechnic School of Algeciras for the preparation of tests and their technical support, and to the doctoral student Alberto Fraile Cava for his contribution to this research.

Conflicts of Interest: The authors declare no conflict of interest.

References

1. Brudtland, G.H. Report of the World Commision on Environement and Development: Our Common Future. Oxford University Press: Oxford, UK, 1987.
2. Setién, J.; Hernández, D.; González, J.J. Characterization of ladle furnace basic slag for use as a construction material. *Constr. Build. Mater.* **2009**, *23*, 1788–1794. [CrossRef]
3. Bilim, C.; Ati, C.D. Alkali activation of mortars containing different replacement levels of ground granulated blast furnace slag. *Constr. Build. Mater.* **2012**, *28*, 708–712. [CrossRef]
4. Hannesson, G.; Kuder, K.; Shogren, R.; Lehman, D. The influence of high volume of fly ash and slag on the compressive strength of self-consolidating concrete. *Constr. Build. Mater.* **2012**, *30*, 161–168. [CrossRef]
5. Özodabaş, A.; Yilmaz, K. Improvement of the performance of alkali activated blast furnace slag mortars with very finely ground pumice. *Constr. Build. Mater.* **2013**, *48*, 26–34. [CrossRef]
6. Rashad, A.M. A comprehensive overview about the influence of different additives on the properties of alkali-activated slag—A guide for Civil Engineer. *Constr. Build. Mater.* **2013**, *47*, 29–55. [CrossRef]
7. Parron-Rubio, M.; Perez-García, F.; Gonzalez-Herrera, A.; Rubio-Cintas, M. Concrete Properties Comparison When Substituting a 25% Cement with Slag from Different Provenances. *Materials* **2018**, *11*, 1029. [CrossRef] [PubMed]
8. Rubio-Cintas, M.D.; Barnett, S.J.; Perez-García, F.; Parron-Rubio, M.E. Mechanical-strength characteristics of concrete made with stainless steel industry wastes as binders. *Constr. Build. Mater.* **2019**, *204*, 675–683. [CrossRef]
9. Gökalp, İ.; Uz, V.E.; Saltan, M.; Tutumluer, E. Technical and environmental evaluation of metallurgical slags as aggregate for sustainable pavement layer applications. *Transp. Geotech.* **2018**, *14*, 61–69. [CrossRef]
10. Rubio Cintas, M.D.; Parrón Vera, M.A.; Contreras de Villa, F. Nuevos usos de las escorias y polvos de humo provocados por la siderurgia. *An. Ing. Mecánica* **2008**, *16*, 1233–1238.
11. Nishigaki, M. Producing permeable blocks and pavement bricks from molten slag. *Stud. Environ. Sci.* **1997**, *71*, 31–40. [CrossRef]
12. Rubio, M.D.; Parrón, M.A.; Contreras, F. Resistencia mecánica de hormigones con sustitución de un porcentaje de cemento por polvos de humo de sílice y escoria de horno de arco eléctrico. In *Comunicaciones V Congreso ACHE*; Asociación Científico-Técnica del Hormigón Estructural: Barcelona, Spain, 2011.
13. Hadjsadok, A.; Kenai, S.; Courard, L.; Michel, F.; Khatib, J. Durability of mortar and concretes containing slag with low hydraulic activity. *Cem. Concr. Compos.* **2012**, *34*, 671–677. [CrossRef]

14. Lam, M.N.T.; Jaritngam, S.; Le, D.H. Roller-compacted concrete pavement made of Electric Arc Furnace slag aggregate: Mix design and mechanical properties. *Constr. Build. Mater.* **2017**, *154*, 482–495. [CrossRef]
15. Xue, Y.; Wu, S.; Hou, H.; Zha, J. Experimental investigation of basic oxygen furnace slag used as aggregate in asphalt mixture. *J. Hazard. Mater.* **2006**, *138*, 261–268. [CrossRef] [PubMed]
16. Behiry, A.E.A.E.M. Evaluation of steel slag and crushed limestone mixtures as subbase material in flexible pavement. *Ain Shams Eng. J.* **2013**, *4*, 43–53. [CrossRef]
17. Sas, W.; Głuchowski, A.; Radziemska, M.; Dziecioł, J.; Szymański, A. Environmental and geotechnical assessment of the steel slags as a material for road structure. *Materials* **2015**, *8*, 4857–4875. [CrossRef]
18. Mahmoud, E.; Ibrahim, A.; El-Chabib, H.; Patibandla, V.C. Self-Consolidating Concrete Incorporating High Volume of Fly Ash, Slag, and Recycled Asphalt Pavement. *Int. J. Concr. Struct. Mater.* **2013**, *7*, 155–163. [CrossRef]
19. Hybská, H.; Hroncová, E.; Ladomerský, J.; Balco, K.; Mitterpach, J. Ecotoxicity of concretes with granulated slag from gray iron pilot production as filler. *Materials* **2017**, *10*, 505. [CrossRef]
20. Boza, M. Universidad de Holguín Utilización de las escorias de acería como material de construcción. *Ciencia Futuro* **2011**, *1*, 31–40.
21. Celik, F.; Canakci, H. An investigation of rheological properties of cement-based grout mixed with rice husk ash (RHA). *Constr. Build. Mater.* **2015**, *91*, 187–194. [CrossRef]
22. Amahjour, F.; Pardo, P.; Borrachero, M.V. Propiedades De Lechadas De Cemento Fabricadas Con Cementos De Tipo I Y Mezclas Con Cenizas Volantes (Cv)Y Humo De Sílice (Hs). In Proceedings of the VIII Congreso Nacional de Propiedades Mecánicas de Sólidos, Gandia, Spain, 25–28 June 2002; pp. 729–737.
23. Pastor, J.L.; Ortega, J.M.; Flor, M.; López, M.P.; Sánchez, I.; Climent, M.A. Microstructure and durability of fly ash cement grouts for micropiles. *Constr. Build. Mater.* **2016**, *117*, 47–57. [CrossRef]
24. Azadi, M.R.; Taghichian, A.; Taheri, A. Optimization of cement-based grouts using chemical additives. *J. Rock Mech. Geotech. Eng.* **2017**, *9*, 623–637. [CrossRef]
25. Zhang, W.; Li, S.; Wei, J.; Zhang, Q.; Liu, R.; Zhang, X.; Yin, H. Grouting rock fractures with cement and sodium silicate grout. *Carbonates Evaporites* **2018**, *33*, 211–222. [CrossRef]
26. Krishnamoorthy, T.S.; Gopalakrishnan, S.; Balasubramanian, K.; Bharatkumar, B.H.; Rama Mohan Rao, P. Investigations on the cementitious grouts containing supplementary cementitious materials. *Cem. Concr. Res.* **2002**, *32*, 1395–1405. [CrossRef]
27. Huang, W.-H. Improving the properties of cement–fly ash grout using fiber and superplasticizer. *Cem. Concr. Res.* **2001**, *31*, 1033–1041. [CrossRef]
28. Bastien, J.; Dugat, J.; Prat, E. Cement Grout Containing Precipitated Silica and Superplasticizers for Post-Tensioning. *ACI Mater. J.* **1997**, *94*, 291–295. [CrossRef]
29. Shannag, M.J. High-performance cementitious grouts for structural repair. *Cem. Concr. Res.* **2002**, *32*, 803–808. [CrossRef]
30. Kim, J.-H.; Lee, H.-S. Improvement of Early Strength of Cement Mortar Containing Granulated Blast Furnace Slag Using Industrial Byproducts. *Materials* **2017**, *10*, 1050. [CrossRef]
31. Rubio Cintas, M.D.; Parrón Vera, M.A.; Contreras, F.; Rubio, M.D.; Parrón, M.A.; Contreras, F. Method for Producing Cinder Concrete. Patent ES20130000758 20130803, 3 June 2015.
32. Ortega, J.M.; Albaladejo, A.; Pastor, J.L.; Sánchez, I.; Climent, M.A. Influence of using slag cement on the microstructure and durability related properties of cement grouts for micropiles. *Constr. Build. Mater.* **2013**, *38*, 84–93. [CrossRef]
33. Manso, J.M.; Polanco, J.A.; Losañez, M.; González, J.J. Durability of concrete made with EAF slag as aggregate. *Cem. Concr. Compos.* **2006**, *28*, 528–534. [CrossRef]
34. Manso, J.M.; Ortega-López, V.; Polanco, J.A.; Setién, J. The use of ladle furnace slag in soil stabilization. *Constr. Build. Mater.* **2013**, *40*, 126–134. [CrossRef]
35. Mavko, G. Effective Medium Theories. Ph.D. Thesis, Stanford University, Stanford, CA, USA, 2010.
36. Li, S.; Sha, F.; Liu, R.; Zhang, Q.; Li, Z. Investigation on fundamental properties of microfine cement and cement-slag grouts. *Constr. Build. Mater.* **2017**, *153*, 965–974. [CrossRef]
37. *EN 197-1:2011 Cement-Part1: Composition, Specifications and Conformity Criteria for Commons Cements*; European Committee for Standardization: Brussels, Belgium, 14 September 2011.
38. *EN 447: 2009 Grout for Prestressing Tendons. Basic Requirements*; European Committee for Standardization: Brussels, Belgium, 2 September 2009.

39. *EN 196-1:2005 Methods of Testing Cement. Determination of Strength*; European Committee for Standardization: Brussels, Belgium, 22 March 2005.
40. *EN 12390-2:2009 Testing Hardened Concrete Part 2: Making and Curing Specimens for Strength Tests*; European Committee for Standardization: Brussels, Belgium, 30 September 2009.
41. *EN 445: 2011 Grout for Prestressing Tendons*; Test methods; European Committee for Standardization: Brussels, Belgium, 10 May 2011.
42. *EN 196-7:2008 Methods of Testing Cement Part 7: Methods of Taking and Preparing Samples of Cement*; European Committee for Standardization: Brussels, Belgium, 31 January 2018.
43. Neville, A.M. *Properties of Concrete/A.M.Neville*, 4th ed.; Longman: Harlow, UK, 1995.
44. Scrivener, K.L.; Crumbie, A.K.; Laugesen, P. The interfacial transition zone (ITZ) between cement paste and aggregate in concrete. *Interface Sci.* **2004**, *12*, 411–421. [CrossRef]
45. Ortiz, M.; Popov, E.P. Plain concrete as a composite material. *Mech. Mater.* **1982**, *1*, 139–150. [CrossRef]
46. Cánovas, M.F.; Gaitan, V.H. Behavior of steel fibe high strength concrete under impact of projectiles. *Mater. Constr.* **2012**, *62*, 381–396. [CrossRef]

materials

MDPI

Article

Rapid Immobilization of Simulated Radioactive Soil Waste Using Self-Propagating Synthesized $Gd_2Ti_2O_7$ Pyrochlore Matrix

Jiali Xue [1], Kuibao Zhang [1,2,*], Zongsheng He [1], Wenwen Zhao [1], Weiwei Li [1], Dayan Xie [1], Baozhu Luo [1], Kai Xu [3] and Haibin Zhang [4,*]

1 State Key Laboratory of Environment-friendly Energy Materials, Southwest University of Science and Technology, Mianyang 621010, China; xuejiali0304@163.com (J.X.); hezongsheng@swust.edu.cn (Z.H.); zhaowenwen@swust.du.cn (W.Z.); liweiwei@swust.du.cn (W.L.); xiedayan@swust.edu.cn (D.X.); luobaozhu@swust.edu.cn (B.L.)

2 Sichuan Civil-Military Integration Institute, Mianyang 621010, China

3 State Key Laboratory of Silicate Materials for Architectures, Wuhan University of Technology, Wuhan 430070, China; kaixu@whut.edu.cn

4 Institute of Nuclear Physics and Chemistry, China Academy of Engineering Physics, Mianyang 621900, China

* Correspondence: zhangkuibao@swust.edu.cn (K.Z.); hbzhang@caep.cn (H.Z.); Tel.: +86-816-241-9492 (K.Z.)

Received: 22 February 2019; Accepted: 8 April 2019; Published: 10 April 2019

Abstract: A rapid and effective method is necessary in the disposal of severely radioactive contaminated soil waste. Simulated Ce-bearing radioactive soil waste was immobilized by self-propagating high-temperature synthesis (SHS) within 5 min in this study. The main work includes the rapid synthesis of soil waste forms, the analysis of phase composition, microstructure and chemical durability. These results show that the simulated nuclide Ce was successfully immobilized into the pyrochlore-rich waste matrice, whose main phases are SiO_2, pyrochlore ($Gd_2Ti_2O_7$) and Cu. The normalized leaching rates of Si and Na on the 42nd day are 1.86×10^{-3} and 1.63×10^{-2} $g \cdot m^{-2} \cdot d^{-1}$, respectively. And the normalized leaching rate of Ce also remains at low level (10^{-5}–10^{-6} $g \cdot m^{-2} \cdot d^{-1}$) within 42 days.

Keywords: Radioactive soil waste; $Gd_2Ti_2O_7$ pyrochlore; SHS; CeO_2; Immobilization

1. Introduction

In recent years, nuclear power has been developed rapidly in the world due to its advantages of high efficiency, economy and low carbon emissions. However, the harm caused by the byproduction of nuclear energy, mainly nuclear wastes, can hardly be ignored, especially high-level radioactive waste (HLW) [1]. The radioactive nuclides in HLW, such as ^{137}Cs, ^{90}Sr, ^{239}Pu, ^{235}U, etc., possess the characteristics of long half-life, high toxicity, and high heat generation [2,3]. When these radionuclides enter the soil, the situation becomes more complicated because the presence of soil will increase the cost of disposal [4,5]. Furthermore, soil contaminated by highly radioactive nuclides may pose a long-term threat to organisms due to ecological cycling [6,7].

For radioactive contaminated soil, sand is an inseparable main substance and must be cured together with radionuclides. At present, there are mainly physical landfill and bioremediation methods for the treatment of radioactive contaminated soil. The physical landfill is a time-consuming project, which will destroy the ecosystem of disposal area. At the same time, it may cause further pollution due to leakage during transportation [8]. The bioremediation method requires a long period of restoration, and the growth of plants is limited by climate and geology [9]. In addition to the above methods, vitrification is an effective technology for the immobilization of long half-life wastes, especially for soil wastes contaminated by high radioactive nuclides [10,11]. Particularly, borosilicate glass is the most

widely studied and utilized vitrified waste form in the world because of its good radiation resistance, corrosion resistance, and chemical stability [12]. Regrettably, the glass matrice may decompose in geological repositories due to high temperature and high pressure [13,14]. Furthermore, the relatively low thermal stability of vitrified waste forms is also a potential limitation [15]. Compared with glass matrice, ceramic solidified bodies have the advantages of low expansion rate, excellent mechanical properties, and good chemical stability. Subsequently, Synroc has been proposed as a potential alternative host matrix for HLW immobilization based on the isomorphism substitution theory [16–20].

Self-propagating high-temperature synthesis (SHS) is a technology that uses the energy released by exothermic redox reactions to synthesize the final products [21–23]. SHS technology possesses certain technical and cost advantages in the treatment of contaminated soil. According to the characteristics of radionuclides, the composition and proportion of a SHS reaction system can be well designed. In addition, quick pressing (QP) is also introduced to obtain compact samples [24]. Zirconolite-rich matrice and titanate-pyrochlore with excellent chemical durability can also be prepared by SHS/QP [25–30]. SHS/QP technology can synthesize high density ceramic matrix in several minutes, which was considered as a potential method to deal with environmental issues. In this study, $Gd_2Ti_2O_7$ pyrochlore waste matrix was synthesized by SHS for the disposal of simulated radioactive soil waste. Ten wt.% CeO_2 was regarded as a simulate of tetravalent actinide [31]. Silica sand was utilized as the heat insulation material and pressure transfer medium during the SHS/QP process. A series of characterizations were carried out to understand the solidifying mechanism of obtained waste forms. In addition, the aqueous durability was evaluated using the standard Product Consistency Test (PCT) method [32].

2. Materials and Methods

The composition of original soil is listed in Table 1. The soil (200 meshes) and simulated radionuclide Ce^{4+} (CeO_2, Aladdin Industrial Inc., purity $\geq$ 99.99%)) were mixed with the weight ratio of 9:1. The SHS reaction was prepared according to the following chemical equation [28]:

$$4CuO + Gd_2O_3 + 2Ti = Gd_2Ti_2O_7 + 4Cu \quad (1)$$

The raw materials of CuO, Gd_2O_3, and Ti (purity $\geq$ 99.9 wt.%) were purchased from Aladdin Industrial Inc. (Shanghai, China). Different contents of simulated radioactive soil wastes (0 wt.%, 5 wt.%, 10 wt.%, 15 wt.%, 20 wt.%, 25 wt.%) were mixed with the raw materials of SHS reaction (labelled as Cu-0, Cu-5, Cu-10, Cu-15, Cu-20, and Cu-25, respectively). Pretreatment of powder samples is similar as the previous study [28].

Table 1. Soil composition in this study.

Composition	SiO_2	Al_2O_3	Fe_2O_3	CaO	K_2O	MgO	Na_2O	TiO_2
Content (wt.%)	66.32	16.57	5.87	4.67	2.86	1.66	0.81	0.74

The SHS/QP process is shown in Figure 1. The self-propagating combustion reactions were ignited by tungsten wire, which was located at one side with tight contact of the green body and heated by a direct current of about 50 A. The SHS reactants were ignited at high temperature, and the combustion wave automatically propagated to the unreacted region until the reaction's completion. Before densification, the W/Re 5/26 thermocouple was placed in the center of the samples to measure the reaction temperature of Cu-0 to Cu-25 specimens. The unpressurized samples were crushed into fine powders for X-ray diffraction analysis (XRD; X'Pert PRO, PANalytical B.V., Almelo, The Netherlands).

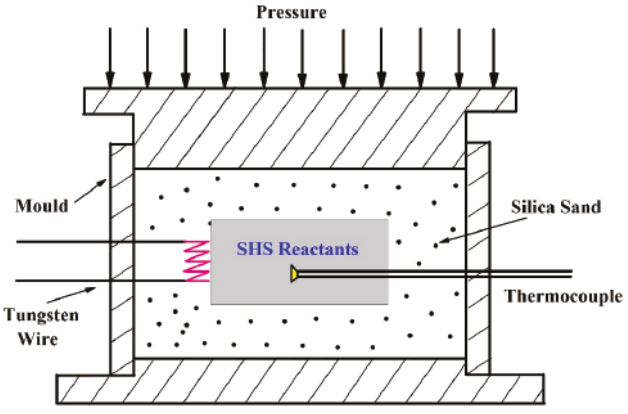

Figure 1. Diagrammatic sketch of the self-propagating high-temperature synthesis/quick pressing (SHS/QP) process.

For densification, the ignited sample was compressed by 50 MPa with 60 s dwelling time after proper combustion delay time. The SHS-ed compact sample was cut and polished to characterize the microstructure and elemental distribution using field-emission scanning electron microscopy (FESEM; Zeiss Ultra-55, Oberkochen, Germany) and energy-dispersive X-ray spectroscopy (EDX, ULTRA 55, ZEISS, Oberkochen, Germany). The chemical durability of waste form was tested by the Product Consistency Test (PCT) standard. The concentrations of Na and Si in leachate were determined by inductively coupled plasma (ICP) analysis (iCPA 6500, ThermoFisher, Waltham, MA, USA), while that of Ce was obtained by inductively coupled plasma-mass spectrometry (ICP-MS) analysis using an Agilent 7700× spectrometer (Agilent, Santa Clara, CA, USA). The normalized release rates were calculated as the following formula:

$$NR_i = \frac{C_i \cdot V}{f_i \cdot S_A \cdot t} \quad (2)$$

where C_i is the concentration of element i in the solution, V is the volume of the leachate (m^3), S_A is the surface area of powder specimen (m^2), f_i is the mass fraction of element i in the sample (wt.%) and t is the leaching duration (d). The S_A/V ratio is about 2000 m^{-1}, which is derived from the standard test method for The Product Consistency Test (ASTM c 1285-02) [32]. In this standard, the waste particles are assumed to be spherical and the average particle diameter is 1.12×10^{-4} m for −100 (0.149 mm) to +200 (0.074 mm) meshes particles. Therefore, the average particle area and volume are calculated as 3.90×10^{-8} m^2 and 7.25×10^{-13} m^3, respectively. The average particle mass is calculated to be 1.96×10^{-6} g. Thus, there are 1 g/1.96×10^{-6} g = 5.11×10^5 particles in 1 g powder waste form with −100 to +200 meshes particles. Thus, the total surface area of 1 g powder with −100 to +200 meshes particles is calculated to be 1.99×10^{-2} m^2. As long as the density and particle size of waste form remain comparable during the leaching tests, this parameter will remain at a constant value and doesn't need to be calculated every time.

3. Results and Discussion

3.1. Temperature and Powder XRD Analysis

The combustion process of the designed SHS reaction takes about 10 s after tungsten wire ignition. The center temperature of all samples in SHS reactions are measured and depicted in Figure 2. With the increment of soil wastes, the center temperatures of Cu-0, Cu-5, Cu-10, Cu-15, Cu-20, and Cu-25 samples decrease from 1679 to 1052 °C in Figure 2. The center temperature of the Cu-0 sample is the highest at 1679 °C, while the Cu-25 sample with the maximum soil content exhibits

the lowest temperature at 1052 °C. Apparently, the increase of soil wastes led to the decrease of SHS reaction temperature.

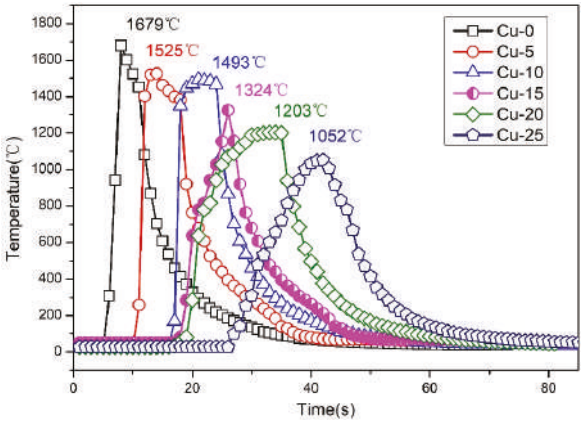

Figure 2. Real temperature curves of all samples during SHS reaction.

The XRD patterns in Figure 3 show that the specimens with soil waste (Cu-5 to Cu-25 samples) are composed of Cu, SiO_2, and $Gd_2Ti_2O_7$ (PDF No. 23-0259), while the sample without soil waste only contains $Gd_2Ti_2O_7$ pyrochlore. From Cu-5 to Cu-25 specimens, the main phase of all samples is $Gd_2Ti_2O_7$ pyrochlore, demonstrating that the increase of soil wastes does not change the phase composition. In Figure 3, the content of Cu in these SHS-ed samples increases with the increment of soil content, but Cu is hardly found in the Cu-0 sample. Because the temperature of Cu-0 reaction is the highest, the Cu melts and condenses into bulky grains during the high temperature reaction. With the decrease of reaction temperature, the size of copper particles decreases. Meanwhile, all SHS-ed samples were ground into powder for XRD testing, where the granulated Cu was sifted out directly. By contrast, the content change of SiO_2 has no regular pattern, which may be affected by the heat insulator silica sand. However, unknown phases appear in the Cu-25 sample, which may be related with the large amount of simulated radioactive soil. Therefore, the Cu-20 specimen was selected for further analysis.

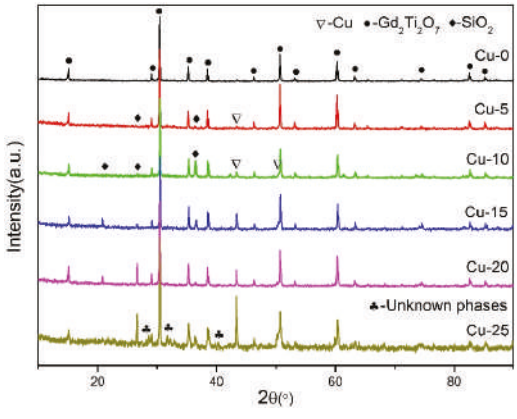

Figure 3. X-ray diffraction (XRD) patterns of all SHS-ed samples.

3.2. Raman Analysis and Microstructure Characterization

Raman spectroscopy was carried out to further analyze the crystal structure and internal bonds of pyrochlore. Raman spectroscopy is an important technique, especially in systems where oxygen displacement induces structure transformation, such as distinguishing fluorite from pyrochlore in pyrochlore ceramics [33]. Different from the $A_2B_2O_7$ fluorite structure with only one F_{2g} vibration mode, the pyrochlore structure contains six Raman modes (A_{1g}, E_g, and $4F_{2g}$). Typical wavenumbers of pyrochlore phase at room temperature are 520 cm^{-1} (A_{1g}), 330 cm^{-1} (E_g), and 200, 310, 450, 580 cm^{-1} ($4F_{2g}$) [33,34]. For Ti-pyrochlore, the most prominent characteristic of Raman spectra are the intensive band at 320 cm^{-1} and the A_{1g} band at 520 cm^{-1}. The band around 320 cm^{-1} includes E_g + F_{2g} modes with very close frequency, which is mostly attributed to O–A–O bond vibration. The A_{1g} band at 520 cm^{-1} is believed to be related to A–O stretching [35,36].

The Raman spectra of Cu-0, Cu-10, and Cu-20 samples are shown in Figure 4. The six Raman active vibration modes (A_{1g}, E_g and $4F_{2g}$) are explicitly assigned. In addition, the Si–O stretching vibration at 1100 cm^{-1} and the Si–O–Si symmetric bending vibration near 700 cm^{-1} are also included. The Raman spectra peaks of three specimens are similar except for some changes in strength, which means the pyrochlore structure of $Gd_2Ti_2O_7$ remains unchanged. In particular, the characteristic F_{2g} (200 cm^{-1} and 455 cm^{-1}) bands are well defined in the Cu-0 specimen. On the contrary, the vibration intensity of E_g + F_{2g} modes (320 cm^{-1}) and A_{1g} mode (520 cm^{-1}) increase significantly in the Cu-10 and Cu-20 samples. It is evident that this drastic change is due to the addition of simulated radioactive soil. On the basis of previous literatures [33–36], we preliminarily speculate that some ions in the simulated radioactive soil (possibly containing Ce) occupy the A and B sites of pyrochlore structure, resulting in steep changes of oxygen ions' environment and peak intensity of Raman spectra.

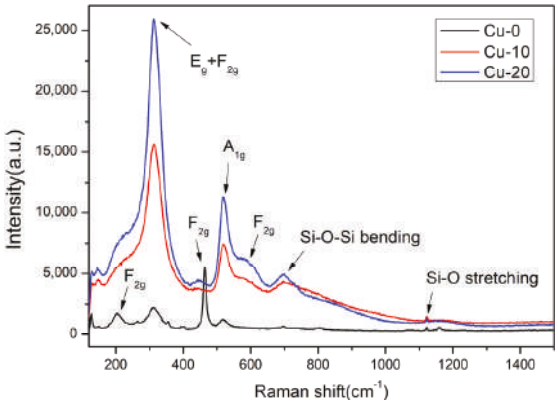

Figure 4. Raman spectra of the Cu-0, Cu-10, and Cu-20 samples.

As shown in Figure 5, the microstructure and elemental distribution of the compact Cu-20 specimen are exhibited in the SEM and elemental mapping images. It can be found that the pores mainly exist in the ceramic matrix rather than the copper phase. It may be argued that the melting point of copper (1083.4 °C) is lower than the combustion temperature of the Cu-20 sample. Therefore, gas can easily be discharged from the copper into the ceramic matrix. The Cu-20 sample consists of four phases, labeled as A, B, C, D in Figure 5a. According to Figure 5b–f and XRD analysis, we speculate that the A region is copper, the B region should be $Gd_2Ti_2O_7$, the C region is SiO_2, and the D region represents TiO_2. The impurity TiO_2 phase is produced from the raw materials of the reaction system and the original soil. However, no TiO_2 exists in the previous XRD result of Cu-20. It is possible that the diffraction peaks of TiO_2 are not obvious because of its low content.

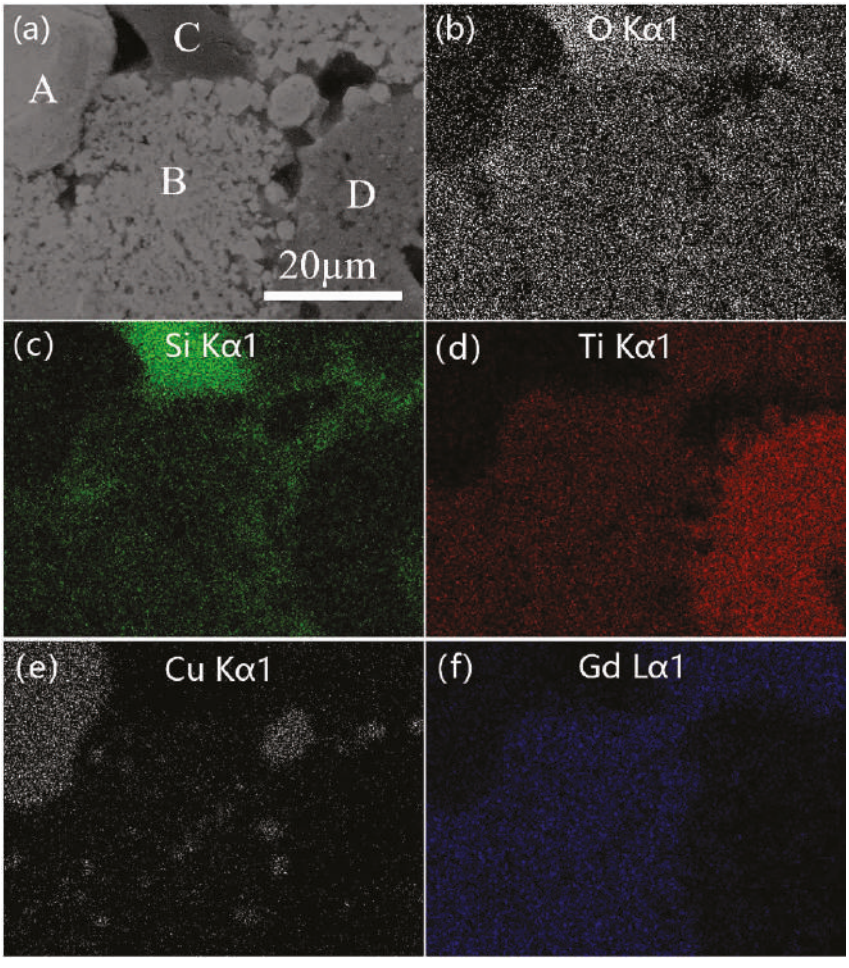

Figure 5. (**a**) SEM image of Cu-20 specimen, and element mapping images of (**b**) O, (**c**) Si, (**d**) Ti, (**e**) Cu, (**f**) Gd.

The EDX elemental spotting analysis of the Cu-20 sample is presented in Figure 6. The EDX spotting image of "B" phase in Figure 6a is presented in Figure 6b. Combined with the XRD and EDX mapping results, the existence of Gd, Ti, Ce, and O in the EDX spotting spectra indicates that the "B" phase is Ce doped $Gd_2Ti_2O_7$ pyrochlore phase. The average elemental quantities are acquired by taking at least five points of "A" area as listed in the inserted table of Figure 6b, which results in the chemical formulation of $Gd_{1.96}Ti_{1.94}Ce_{0.09}O_7$. Meanwhile, a small amount of Ce is also found in the soil phase according to Figure 6c, indicating that the simulated nuclide Ce of radioactive soil waste can exist in both the pyrochlore phase and soil phase. At the same time, most of the elements in original soil are retained in the soil phase. Figure 6d shows that only Ti and O are present in the D region, which confirms that the D phase is TiO_2.

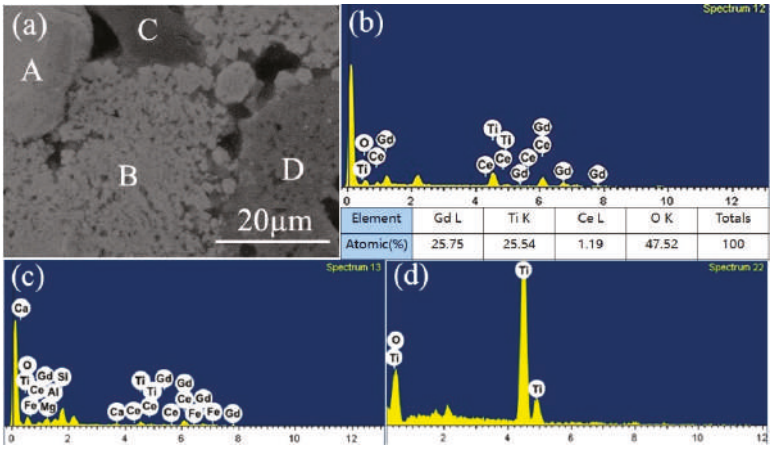

Figure 6. Energy dispersive X-ray spectroscopy (EDX) elemental spotting analysis: (**a**) Representative SEM image of the Cu-20 sample, (**b**) EDX spectrum and elemental composition of the labeled "B" area in (**a**), (**c**) EDX spectrum of region C in (**a**), (**d**) EDX spectrum of region D in (**a**).

3.3. Chemical Durability Measurement by PCT Leaching Test

The leaching performance of nuclear waste forms is a significant indicator for estimating the chemical stability [37]. The 1–42 days normalized elemental leaching rates of Si, Na, and Ce of the Cu-20 sample are depicted in Figure 7. With the extension of soaking time, the normalized leaching rates of Na and Si show a downward trend from 1 to 14 days. Then, NR_{Na} and NR_{Si} exhibit slight ascension within 14–28 days, and finally both of them reach the lowest values in 42 days. The day 1 and day 42 NR_{Si} values are 2.04×10^{-2} and 1.86×10^{-3} g·m^{-2}·d^{-1}, which represent excellent stability. The lowest value of NR_{Na} is 1.63×10^{-2} g·m^{-2}·d^{-1} after 42 days of leaching. This rule is not applicable for Ce, whose leaching rate has no definite regulation. The NR_{Ce} varies from 7.20×10^{-5} g·m^{-2}·d^{-1} of 42 days to 2.20×10^{-6} g·m^{-2}·d^{-1} of 7 days, which is about five orders of magnitude lower than the NR_{Na} values. The NR_{ce} values vary irregularly but remain at a low level (10^{-5}–10^{-6} g·m^{-2}·d^{-1}). Compared with our previous research results [38], the leaching rate of Si is slightly lower in this study. The NR_{Na} of the Cu-20 sample is similar to that of borosilicate glass-ceramics [39]. Nevertheless, the leaching performance of simulated nuclide in Cu-20 sample is significantly lower than that of typical vitreous products [40].

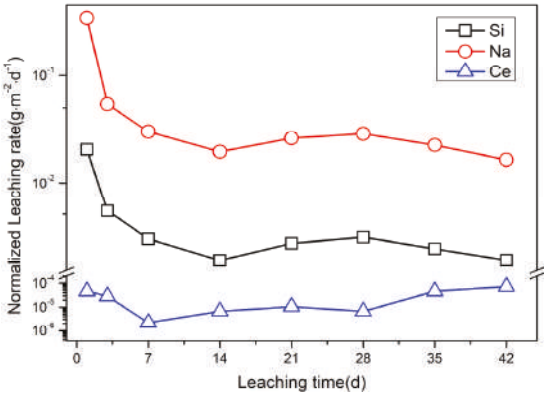

Figure 7. Normalized leaching rates of Si, Na, and Ce from day 1–42.

4. Conclusions

In summary, a series of $Gd_2Ti_2O_7$-based waste forms containing 5–25 wt.% simulated radioactive contaminated soil have been successfully synthesized by SHS in 5 min. The obtained products are multiphase composite materials composed of SiO_2, $Gd_2Ti_2O_7$, and Cu. Furthermore, the simulated nuclide Ce exists in pyrochlore and soil phases simultaneously, which indicates that Ce migrates partly from soil to pyrochlore phase during the SHS reaction. The solidified body of Cu-20 sample exhibits high stability. The 42 days NR_{Si} and NR_{Na} are as low as 1.86×10^{-3} and 1.63×10^{-2} $g \cdot m^{-2} \cdot d^{-1}$, respectively. And the 1–42 days NR_{Ce} values also remain at a low level (10^{-5}–10^{-6} $g \cdot m^{-2} \cdot d^{-1}$). Based on the analysis of phase composition, microstructure, and chemical durability, the application potential of SHS technology in the rapid disposal of radioactive soil wastes is revealed.

Author Contributions: Conceptualization, K.Z., B.L. and H.Z.; Methodology, K.Z. and J.X.; Formal Analysis, J.X., K.X., Z.H. and W.Z.; Investigation, J.X., W.L., D.X. and Z.H.; Writing—Original Draft Preparation, J.X.; Writing—Review & Editing, K.Z. and B.L.

Funding: This research was funded by the National Natural Science Foundation of China (No. 51672228), the Project of State Key Laboratory of Environment-friendly Energy Materials (Southwest University of Science and Technology, No. 16kffk05 and 17FKSY0104) and Science Development Foundation of China Academy of Engineering Physics.

Conflicts of Interest: The authors declare no conflict of interest.

References

1. International Atomic Energy Agency. *Design and Operation of High Level Waste, Vitrification and Storage Facility (Technical Report Series No. 176)*; IAEA: Vienna, Austria, 1977.
2. Ojovan, M.I.; Lee, W.E. *An Introduction to Nuclear Waste Immobilization*; Elsevier Ltd.: Oxford, UK, 2005; pp. 213–267.
3. Caurant, D.; Loiseau, P.; Majérus, O.; Aubin-Chevaldonnet, V.; Bardez, I.; Quintas, A. *Glasses, Glass-Ceramics and Ceramics for Immobilization of Highly Radioactive Nuclear Wastes*; Nova Science Publishers: New York, NY, USA, 2009.
4. Zhu, Y.G.; Shaw, G. Soil contamination with radionuclides and potential remediation. *Chemosphere* **2000**, *41*, 121–128. [PubMed]
5. Mao, X.H.; Qin, Z.G.; Yuan, X.N.; Wang, C.M.; Cai, X.N.; Zhao, W.X.; Zhao, K.; Yang, P.; Fan, X.L. Immobilization of simulated radioactive soil waste containing cerium by self-propagating high-temperature synthesis. *J. Nucl. Mater.* **2013**, *443*, 428–431. [CrossRef]
6. Gavrilescu, M.; Pavel, L.V.; Cretescu, I. Characterization and remediation of soils contaminated with uranium. *J. Hazard. Mater.* **2009**, *163*, 475–510. [CrossRef] [PubMed]
7. Yasunari, T.J.; Stohl, A.; Hayano, R.S.; Burkhart, J.F.; Eckhardt, S.; Yasunari, T. Cesium-137 deposition and contamination of Japanese soils due to the Fukushima nuclear accident. *Proc. Natl. Acad. Sci. USA* **2011**, *108*, 19530–19534. [CrossRef] [PubMed]
8. Xie, Y.; Wu, T.; Shi, Z.K.; Zhang, D. A very low level radioactive waste landfill soil characteristics and properties of strontium block. *Chem. Res. Appl.* **2013**, *25*, 558–562.
9. Lloyd, J.R.; Renshaw, J.C. Bioremediation of radioactive waste: Radionuclide-microbe interactions in laboratory and field-scale studies. *Curr. Opin. Biotech.* **2005**, *16*, 254–260. [CrossRef]
10. Zhang, S.; Ding, Y.; Lu, X.R.; Mao, X.L.; Song, M.X. Rapid and efficient disposal of radioactive contaminated soil using microwave sintering method. *Mater. Lett.* **2016**, *175*, 165–168.
11. Zhang, S.; Shu, X.Y.; Chen, S.Z.; Yang, H.M.; Hou, C.X.; Mao, X.L.; Chi, F.T.; Song, M.X.; Lu, X.R. Rapid immobilization of simulated radioactive soil waste by microwave sintering. *J. Hazard. Mater.* **2017**, *337*, 20–26. [PubMed]
12. Gin, S.; Abdelouas, A.; Criscenti, L.J.; Ebert, W.L. An international initiative on long-term behavior of high-level nuclear waste glass. *Mater. Today* **2013**, *16*, 243–248. [CrossRef]
13. Mccarthy, G.J.; Ebert, W.L.; Roy, R.; Scheetz, B.E. Interactions between nuclear waste and surrounding rock. *Nature* **1978**, *273*, 216–217. [CrossRef]

14. Loiseau, P.; Caurant, D.; Majerus, O.; Baffier, N.; Fillet, C. Crystallization study of (TiO_2, ZrO_2)-rich SiO_2-Al_2O_3-CaO glasses. Part II. Surface and internal crystallization processes investigated by differential thermal analysis (DTA). *J. Mater. Sci.* **2003**, *38*, 843–852.
15. Caurant, D.; Majérus, O.; Loiseau, P.; Bardez, I.; Baffier, N.; Dussossoy, J.L. Crystallization of neodymium-rich phases in silicate glasses developed for nuclear waste immobilization. *J. Nucl. Mater.* **2006**, *354*, 143–162.
16. Ringwood, A.E.; Kesson, S.E.; Ware, N.G.; Hibberson, W.; Major, A. Immobilization of high level nuclear reactor wastes in SYNROC. *Nature* **1979**, *278*, 219–223. [CrossRef]
17. Franck, P.; John, M.H.; Urs, S. The current state and future of accessory mineral research. *Chem. Geol.* **2002**, *191*, 3–24.
18. Vance, E.R. Development of ceramic waste forms for high-level nuclear waste over the last 30 years. *Mater. Res. Soc. Symp. Proc.* **2006**, *985*, 135–140. [CrossRef]
19. Weber, W.J.; Navrotsky, A.; Stefanovsky, S.; Vance, E.R.; Vernaz, E. Materials science of high-level nuclear waste immobilization. *MRS Bull.* **2009**, *34*, 46–53. [CrossRef]
20. Zhang, K.B.; Yin, D.; Han, P.W.; Zhang, H.B. Two-step synthesis of zirconolite-rich ceramic waste matrice and its physicochemical properties. *Int. J. Appl. Ceram. Technol.* **2018**, *15*, 171–178. [CrossRef]
21. Muthuraman, M.; Dhas, N.A.; Patil, K.C. Combustion synthesis of oxide materials for nuclear waste immobilization. *Bull. Mater. Sci.* **1994**, *17*, 977–987. [CrossRef]
22. Muthuraman, M.; Patil, K.C.; Senbagaraman, S.; Umarji, A.M. Sintering, microstructure and dilatometric studies of combustion synthesized Synroc phases. *Mater. Res. Bull.* **1996**, *31*, 1375–1381. [CrossRef]
23. He, Z.S.; Zhang, K.B.; Xue, J.L.; Zhao, W.W.; Zhang, H.B. Self-propagating chemical furnace synthesis of nanograin $Gd_2Zr_2O_7$ ceramic and its aqueous durability. *J. Nucl. Mater.* **2018**, *512*, 385–390. [CrossRef]
24. Zhang, K.B.; Wen, G.J.; Zhang, H.B.; Teng, Y.C. Self-propagating high-temperature synthesis of $Y_2Ti_2O_7$ pyrochlore and its aqueous durability. *J. Nucl. Mater.* **2015**, *465*, 1–5.
25. Zhang, K.B.; He, Z.S.; Peng, L.; Zhang, H.B.; Lu, X.R. Self-propagating synthesis of $Y_{2-x}Nd_xTi_2O_7$ pyrochlore and its aqueous durability as nuclear waste form. *Scripta. Mater.* **2018**, *146*, 300–303.
26. Zhang, K.B.; He, Z.S.; Xue, J.L.; Zhao, W.W.; Zhang, H.B. Self-propagating synthesis of $Y_{2-x}Nd_xTi_2O_7$ pyrochlores using CuO as the oxidant and its characterizations as waste form. *J. Nucl. Mater.* **2018**, *507*, 93–100. [CrossRef]
27. Zhang, K.B.; Yin, D.; Peng, L.; Wu, J.J. Self-propagating synthesis and CeO_2 immobilization of zirconolite-rich composites using CuO as the oxidant. *Ceram. Int.* **2017**, *43*, 1415–1423. [CrossRef]
28. Peng, L.; Zhang, K.B.; Yin, D.; Wu, J.J.; He, S.H.; He, H.M. Self-propagating synthesis, mechanical property and aqueous durability of $Gd_2Ti_2O_7$ pyrochlore. *Ceram. Int.* **2016**, *42*, 18907–18913. [CrossRef]
29. Peng, L.; Zhang, K.B.; He, Z.S.; Yin, D.; Xue, J.L.; Xu, C.; Zhang, H.B. Self-propagating high-temperature synthesis of ZrO_2 incorporated $Gd_2Ti_2O_7$ pyrochlore. *J. Adv. Ceram.* **2018**, *7*, 41–49. [CrossRef]
30. He, Z.S.; Zhang, K.B.; Peng, L.; Zhao, W.W.; Xue, J.L.; Zhang, H.B. Self-propagating plus quick pressing synthesis and characterizations of $Gd_{2-x}Nd_xTi_{1.3}Zr_{0.7}O_7$ ($0 \leq x \leq 1.4$) pyrochlores. *J. Nucl. Mater.* **2018**, *504*, 61–67. [CrossRef]
31. Kim, H.S.; Joung, C.Y.; Lee, B.H.; Oh, J.Y.; Koo, Y.H.; Heimgartner, P. Applicability of CeO_2 as a surrogate for PuO_2 in a MOX fuel development. *J. Nucl. Mater.* **2008**, *378*, 98–104. [CrossRef]
32. ASTM Committee. *Standard Test Methods for Determining Chemical Durability of Nuclear, Hazardous, and Mixed Waste Glasses and Multiphase Glass Ceramics: The Product Consistency Test (PCT)*; ASTM International: West Conshohocken, PA, USA, 2002.
33. Mączka, M.; Hanuza, J.; Hermanowicz, K.; Fuentes, A.F.; Matsuhira, K.; Hiroi, Z. Temperature-dependent Raman scattering studies of the geometrically frustrated pyrochlores $Dy_2Ti_2O_7$, $Gd_2Ti_2O_7$ and $Er_2Ti_2O_7$. *J. Raman Spectrosc.* **2008**, *39*, 537–544. [CrossRef]
34. Mączka, M.; Sanjuán, M.L.; Fuentes, A.F.; Macalik, L.; Hanuza, J.; Matsuhira, K.; Hiroi, Z. Temperature-dependent studies of the geometrically frustrated pyrochlores $Ho_2Ti_2O_7$ and $Dy_2Ti_2O_7$. *Phys. Rev. B* **2009**, *79*, 214437. [CrossRef]
35. Zhang, F.X.; Manoun, B.; Saxena, S.K. Pressure-induced order-disorder transitions in pyrochlore $RE_2Ti_2O_7$ (RE = Y, Gd). *Mater. Lett.* **2006**, *60*, 2773–2776. [CrossRef]
36. Sanjuán, M.L.; Guglieri, C.; DíazMoreno, S.; Aquilanti, G.; Fuentes, A.F.; Olivi, L.; Chaboy, J. Raman and X-ray absorption spectroscopy study of the phase evolution induced by mechanical milling and thermal treatments in $R_2Ti_2O_7$ pyrochlores. *Phys. Rev. B* **2011**, *84*, 104207. [CrossRef]

37. Zhang, Y.; Stewart, M.W.A.; Li, H.; Carter, M.L.; Vance, E.R.; Moricca, S. Zirconolit-rich titanate ceramics for immobilisation of actinides-Waste form/HIP can interactions and chemical durability. *J. Nucl. Mater.* **2009**, *395*, 69–74. [CrossRef]
38. Xue, J.L.; Zhang, K.B.; He, Z.H.; Zhao, W.W.; Li, W.W.; Xie, D.Y.; Zhang, H.B. Rapid disposal of simulated Ce-bearing radioactive soil waste using self-propagating synthesized zirconolite-rich waste matrice. *Ceram. Int.* **2018**, *44*, 14534–14540.
39. Wu, L.; Li, Y.X.; Teng, Y.C.; Meng, G.L. Preparation and characterization of borosilicate glass-ceramics containing zirconolite and titanite crystalline phases. *J. Non-Cryst. Solids* **2013**, *380*, 123–127. [CrossRef]
40. Ojovan, M.I.; Lee, W.E. Glassy Wasteforms for Nuclear Waste Immobilization. *Metall. Mater. Trans. A* **2011**, *42*, 837–851. [CrossRef]

MDPI
St. Alban-Anlage 66
4052 Basel
Switzerland
Tel. +41 61 683 77 34
Fax +41 61 302 89 18
www.mdpi.com

Materials Editorial Office
E-mail: materials@mdpi.com
www.mdpi.com/journal/materials

MDPI
St. Alban-Anlage 66
4052 Basel
Switzerland

Tel: +41 61 683 77 34
Fax: +41 61 302 89 18

www.mdpi.com

ISBN 978-3-03943-111-3